

GROWTH, FABRICATION, AND CHARACTERIZATION OF CARBON NANOTUBES,  
NANOTUBE FILMS, AND NANOWIRES

By

YONGHO CHOI

A DISSERTATION PRESENTED TO THE GRADUATE SCHOOL  
OF THE UNIVERSITY OF FLORIDA IN PARTIAL FULFILLMENT  
OF THE REQUIREMENTS FOR THE DEGREE OF  
DOCTOR OF PHILOSOPHY

UNIVERSITY OF FLORIDA

2008

© 2008 Yongho Choi

To my parents, Heeyual Park and Hyungjin Choi; my wife, Sungeun Kim; my son, Andrew Minjun Choi, with love.

## ACKNOWLEDGMENTS

First and foremost, I express my sincere gratitude to my advisor, Professor Ant Ural. It was one of the great fortunes in my life to work for him and to start my research career under his guidance. His greatest guidance helped me to learn knowledge and also helped me to improve skills of my logical thinking and handling of research projects. With his patience, encouragement, and invaluable advice, I improved my research abilities and accomplish this work.

I would like to express my sincere appreciation to my committee members, Professor Gijs Bosman, Professor Jing Guo, and Professor Kirk Ziegler, for their invaluable discussions, suggestions and kind supports.

My appreciation also goes to Ashkan Behnam, Jason Johnson, Leila Noriega, Joe Portillo, and all other former and current nanotech group members. We discussed a lot of issues together and made a lot of good times as a friend.

I give sincere appreciation and love to my family. Their support with belief is the strongest energy for me to stand up and to walk ahead.

## TABLE OF CONTENTS

	<u>page</u>
ACKNOWLEDGMENTS .....	4
LIST OF TABLES .....	8
LIST OF FIGURES .....	9
ABSTRACT.....	11
CHAPTER	
1 INTRODUCTION .....	13
Single-Walled Carbon Nanotubes .....	15
Single-Walled Carbon Nanotube Geometrical and Electronic Structure .....	15
Single-Walled Carbon Nanotube Growth Methods .....	17
GaN Nanowires .....	18
2 SINGLE-WALLED CARBON NANOTUBE GROWTH FROM ION IMPLANTED IRON CATALYST.....	27
Introduction.....	27
Ion Implantation.....	28
Liquid-Based Catalyst .....	28
Experimental Procedure.....	29
Results and Discussion .....	29
AFM Characterization .....	29
TEM Characterization .....	32
Raman Spectroscopy Characterization and Discussion .....	33
Electrical Characterization .....	36
Conclusions.....	37
3 MICROMACHINED SILICON TRANSMISSION ELECTRON MICROSCOPY GRIDS FOR DIRECT CHARACTERIZATION OF AS-GROWN NANOTUBES AND NANOWIRES .....	47
Introduction.....	47
Design of the TEM Grids .....	48
Microfabrication of the TEM Grids.....	49
Nanotube Growth on the TEM Grids .....	50
Characterization of Nanotubes Grown on the TEM Grids .....	50
Conclusions.....	52

4	SILICON OXIDE NANOWIRE GROWTH FROM IRON ION IMPLANTED SiO <sub>2</sub> SUBSTRATES .....	58
	Introduction.....	58
	Experimental Method .....	59
	Results and Discussion .....	60
	Conclusions.....	63
5	GaN NANOWIRE GROWTH FROM ION IMPLANTED IRON CATALYST .....	71
	Introduction.....	71
	Experimental Method .....	72
	Results and Discussion .....	73
	Conclusions.....	75
6	NANOLITHOGRAPHIC PATTERNING OF TRANSPARENT, CONDUCTIVE SINGLE-WALLED CARBON NANOTUBE FILMS BY INDUCTIVELY COUPLED PLASMA REACTIVE ION ETCHING.....	82
	Introduction.....	82
	SWNT Film Deposition.....	83
	Lithography.....	83
	O <sub>2</sub> Plasma Etching .....	84
	Results and Discussion .....	85
	Effect of Substrate Bias Power.....	88
	Effect of Chamber Pressure.....	89
	Effect of Substrate Cooling .....	89
	Comparison to Parallel-Plate RIE System.....	90
	Conclusions.....	90
7	FABRICATION AND DARK CURRENT CHARACTERIZATION OF METAL-SEMICONDUCTOR-METAL (MSM) PHOTODETECTORS WITH TRANSPARENT AND CONDUCTIVE CARBON NANOTUBE FILM SCHOTTKY ELECTRODES.....	98
	Introduction.....	98
	Experimental Method .....	99
	Result and Discussion.....	100
	Conclusions.....	102
8	CONCLUSIONS AND FUTURE WORK.....	108
	Conclusions.....	108
	Suggestions for Future Work.....	109
APPENDIX		
A	MASK LAYOUT .....	111

LIST OF REFERENCES .....113  
BIOGRAPHICAL SKETCH .....122

## LIST OF TABLES

<u>Table</u>		<u>page</u>
2-1	Average height and density of catalyst nanoparticles formed after annealing and the average diameter and density of nanotubes grown for each Fe ion implantation condition..	46
2-2	Density of catalyst nanoparticles formed after growth for each Fe ion implantation condition ..	46
6-1	Etch rates of the SWNT film and three different resists ..	97

## LIST OF FIGURES

<u>Figure</u>	<u>page</u>
1-1 Unrolled graphene sheet making up SWNT and its honeycomb lattice. ....	23
1-2 Reciprocal lattice of graphene (unrolled carbon nanotube).....	23
1-3 Energy dispersion relations for graphene shown throughout whole region of Brillouin zone.....	24
1-4 Schematic of CVD system used to grow SWNTs .....	25
1-5 Lattice constant of III-V nitride semiconductor materials as a function of bandgap energy.....	26
2-1 Distribution profiles of various ions in crystalline silicon after implantation at energy of 200 keV.....	38
2-2 AFM images of liquid catalyst and SWNTs grown from the catalyst.....	38
2-3 AFM images of Fe catalyst nanoparticles formed after annealing and Carbon nanotubes grown by CVD.....	39
2-4 AFM images of Fe catalyst nanoparticles formed after annealing and Carbon nanotubes grown by CVD.....	40
2-5 Optical microscope image of micromachined Si TEM grids and HRTEM images of SWNTs.....	41
2-6 Micro Raman spectra of grown nanotubes .....	42
2-7 Kataura plot showing the electronic transition energies for all possible SWNTs as a function of diameter.....	43
2-8 Cross-sectional schematic of process flow for SWNT transistor .....	44
2-9 Optical microscope image of fabricated nanotube device sample.....	45
2-10 Cross-sectional schematic view of SWNT transistor device and $I_{DS}-V_{GS}$ curve .....	45
3-1 Images of micromachined Si TEM grid.....	53
3-2 Process flow for micromachined Si TEM grids.....	54
3-3 HRTEM images of SWNTs taken using micromachined Si TEM grids.....	55
3-4 SEM images of nanotubes and AFM images of ion implanted catalyst and solution-based catalyst .....	56

3-5	Micro-Raman spectra of SWNTs grown from ion implanted catalyst .....	57
4-1	Schematic of Fe ion implantation condition and depth profile of Fe atoms .....	65
4-2	SEM images of silicon oxide nanowires.....	66
4-3	TEM images of silicon oxide nanowires.....	67
4-4	EDS spectrum of individual silicon oxide nanowire. ....	68
4-5	AFM images of SiO <sub>2</sub> sample surface.....	69
4-6	Solid-liquid-solid (SLS) growth model of silicon oxide nanowires .....	70
5-1	Depth profile of Fe atoms in SiO <sub>2</sub> . and schematic of CVD setup.....	77
5-2	AFM images of Fe catalyst nanoparticles formed after annealing .....	78
5-3	SEM image and XRD pattern of as-grown GaN nanowires .....	79
5-4	HRTEM image, SAED pattern, and EDS spectrum of individual GaN nanowire .....	80
5-5	Vapor-liquid-solid (VLS) growth mechanism for GaN nanowires. ....	81
6-1	AFM image and transmittance spectra of SWNT films.....	92
6-2	Schematic of ICP-RIE system .....	93
6-3	AFM image of etched SWNT film .....	94
6-4	Text characters printed in SWNT film.....	95
6-5	AFM image of a series of nanotube film lines.....	96
7-1	MSM photodetector .....	103
7-2	Process flow for MSM photodetectors with SWNT film electrodes.....	104
7-3	Dark current of SWNT film-GaAs MSM device.....	105
7-4	Dark current of SWNT film-GaAs MSM device.....	106
A-1	Mask layout for nanotube device fabrication.....	111
A-2	Mask layout for single nanotube device .....	112

Abstract of Dissertation Presented to the Graduate School  
of the University of Florida in Partial Fulfillment of the  
Requirements for the Degree of Doctor of Philosophy

GROWTH, FABRICATION, AND CHARACTERIZATION OF CARBON NANOTUBES,  
NANOTUBE FILMS, AND NANOWIRES

By

Yongho Choi

December 2008

Chair: Ant Ural

Major: Electrical and Computer Engineering

We explored nucleating the growth of nanomaterials by the ion implantation technique. We present experimental evidence that single-walled carbon nanotubes (SWNT) and  $\text{SiO}_x$  and GaN nanowires can be grown by Fe ion implantation into  $\text{SiO}_2/\text{Si}$  substrates, subsequent annealing, and chemical vapor deposition (CVD) growth. Moreover, we show that there is a dose and energy window of ion implantation in which SWNT and nanowire growth are observed for a given growth condition. For nanomaterials growth, catalyst is usually spun on or drop-dried from a liquid solution containing iron nanoparticles or deposited as solid thin film layers by evaporation or sputtering. However, it is not possible to pattern the liquid solution-based catalyst into very small dimensions or the thin film catalyst into nonplanar three-dimensional (3D) device structures, such as the sidewalls of high aspect ratio trenches. By adopting the ion implantation technique for nucleating nanomaterials growth, this thesis opens up the possibility of controlling the origin of nanomaterials at the nanometer scale and of integrating nanomaterials into nonplanar 3D device structures with precise dose control. We also fabricate micromachined Si Transmission Electron Microscopy (TEM) grids for direct TEM, as well as Atomic Force Microscopy (AFM), Scanning Electron Microscopy (SEM), and Raman characterization of as-grown nanomaterials. As a result, these micromachined TEM grids offer

fast, easy, and reliable structural characterization. Furthermore these grids provide a low cost, mass producible, efficient, reliable, and versatile platform for direct TEM, AFM, SEM, and Raman analysis of as-grown nanomaterials, eliminating the need for any post-processing growth.

We also explored fabrication and characterization of single-walled carbon nanotube films which are three-dimensional films of tens of nanometers thickness, consisting of an interwoven mesh of single-walled carbon nanotubes. We demonstrate, for the first time, patterning of SWNT films down to submicron lateral dimensions as small as 50 nm using e-beam lithography and inductively coupled plasma (ICP) etching. This simple and efficient “top-down” patterning capability developed could open up tremendous opportunities for integrating single-walled nanotube films into a wide range of electronic and optoelectronic devices. Furthermore, we fabricate and characterize the effect of device geometry on the dark current of metal-semiconductor-metal (MSM) photodetectors based on SWNT film-GaAs Schottky contacts. We observed that dark currents of the MSM devices scale rationally with device geometry, such as the device active area, finger width, and finger spacing. These results open up the possibility of integrating SWNT films as transparent and conductive Schottky electrodes in conventional semiconductor electronic and optoelectronic devices.

## CHAPTER 1 INTRODUCTION

The continuous drive toward increasingly smaller length scales has led to many advances in science and technology over the past century. One of the most remarkable examples of this drive towards miniaturization is the microelectronics industry, which has constantly relied on scaling to create denser, faster, and cheaper devices since the invention of the first transistor. However, the scaling of silicon integrated circuit technology is predicted to slow down and reach the end of the “roadmap” in the next few decades [1-4]. Instead of trying to push this “top-down” scaling paradigm further, an alternative is to use a “bottom-up” fabrication approach to achieve even smaller length scales. This “bottom-up” approach involves using nanomaterials, which naturally have very small size, as the building blocks of new electrical, mechanical, chemical, and biological devices. Single-walled carbon nanotubes (SWNTs) and semiconductor nanowires, which have attracted a significant amount of research attention in recent years, are promising nanoscale materials as building blocks for “bottom-up” assembly of nanoelectronics [5-27]. SWNTs have also remarkable physical and electronic properties, such as high mobility and current density. Based on these characteristics, device applications such as sensors and transistors have been demonstrated experimentally [28-30].

There are several growth methods developed to synthesize SWNTs, namely arc-discharge, laser ablation and chemical vapor deposition (CVD). However, controlled growth has remained a big challenge for manufacturing SWNTs for device applications. An essential component of the CVD growth process is the catalyst material placed on the substrate for nucleating the growth of carbon nanotubes. In this dissertation, we demonstrate that ion implantation, a well-established technique in silicon microfabrication, and subsequent annealing can be used as an alternative method to create catalyst nanoparticles for single-walled carbon nanotube growth, as

presented in Chapter 2. To characterize the structure of the as-grown SWNTs *directly* after CVD growth, a silicon based micromachined transmission electron microscopy (TEM) grid is designed and fabricated, as described in Chapter 3. In Chapters 4 and 5, we further extend the use of ion implanted catalyst to nanowire growth. In Chapter 4, we show that SiO<sub>x</sub> nanowires can be grown from ion implanted catalyst by the solid-liquid-solid (SLS) growth mechanism. In Chapter 5, we show the vapor-liquid-solid (VLS) growth of GaN nanowires from the ion implanted catalyst.

An alternative way to overcome the manufacturability problems of individual SWNTs is using single-walled carbon nanotube films, which are three-dimensional networks of interwoven SWNTs. In the nanotube film, individual variations in diameter and chirality of nanotubes are averaged, and this results in uniform physical and electronic properties. Furthermore, what makes SWNT films even more attractive for device applications is that they are flexible, transparent, and conductive. Any potential device application utilizing SWNT films [31-43] requires the capability to efficiently pattern them. In Chapter 6, we present an efficient technique that we have developed to pattern SWNT films by photolithography or e-beam lithography, and subsequent O<sub>2</sub> plasma etching using an inductively coupled plasma (ICP).

Using the patterning technique developed and shown in Chapter 6, we fabricate Metal-Semiconductor-Metal (MSM) photodetectors with SWNT film electrodes on GaAs substrates. In Chapter 7, we present the fabrication process of SWNT film-GaAs MSM photodetectors and the characterization of their dark current. The conclusions of this dissertation and suggested future works are given in Chapter 8.

## Single-Walled Carbon Nanotubes

### Single-Walled Carbon Nanotube Geometrical and Electronic Structure

A single walled carbon nanotube is a graphene sheet rolled into a cylindrical shape of diameter ranging from 0.7 nm to 10 nm. Three types of SWNT structures namely, armchair, zigzag, and chiral, are possible depending on the chiral vector,  $C_h$ , which is defined below.

Figure 1-1 shows the unrolled graphene sheet and its honeycomb lattice. The vector  $\overline{OB}$  is in the direction of the longitudinal nanotube axis, and the vector  $\overline{OA}$  corresponds to a cross-section of the nanotube perpendicular to the nanotube axis. The chiral vector  $C_h$  and the translation vector  $T$  can be defined by those two vectors,  $\overline{OA}$  and  $\overline{OB}$ , respectively, and the nanotube can be formed when the point O is connected to A and the point B is connected to B'.

The chiral vector  $C_h$  is defined as

$$C_h = na_1 + ma_2 = (n, m), \quad (1)$$

where  $a_1$  and  $a_2$  are the real space unit vectors of graphene, as shown in Figure 1-1, and any point on the hexagonal graphene lattice can be expressed by them. Three types of nanotubes can be classified by the chiral vector  $C_h$ . The zigzag nanotube is the case when  $C_h = (n, 0)$ , the armchair nanotube is the case when  $n=m$ , that is  $C_h = (n, n)$ , and all other combinations of  $n$  and  $m$  are chiral nanotubes. The diameter of the nanotube,  $d_t$ , can be calculated by

$$d_t = L / \pi = |C_h| / \pi = \sqrt{C_h \cdot C_h} / \pi = a \sqrt{n^2 + m^2 + nm} / \pi, \quad (2)$$

where  $L$  is the circumference of the nanotube and  $a = 2.49 \text{ \AA}$  is the lattice constant of the honeycomb graphene lattice. Furthermore, the chiral angle  $\theta$  represents the angle between the chiral vector  $C_h$  and the vector  $a_1$ , and it is in the range from  $0$  to  $30^\circ$ . The chiral angle  $\theta = 0^\circ$  corresponds to zigzag nanotubes,  $30^\circ$  corresponds to armchair nanotubes, and all other angles

between  $0$  and  $30^\circ$  correspond to chiral nanotubes. The translational vector,  $\mathbf{T}$ , is defined as the vector which is parallel to the nanotube axis and is normal to the chiral vector,  $\mathbf{C}_h$ , as shown in Figure 1-1. Similar to the vector  $\mathbf{C}_h$ , the vector  $\mathbf{T}$  can be expressed in terms of the two basis vectors  $\mathbf{a}_1$  and  $\mathbf{a}_2$ , as

$$\mathbf{T} = t_1 \mathbf{a}_1 + t_2 \mathbf{a}_2 = (t_1, t_2) \quad (3)$$

By using the relationship  $\mathbf{C}_h \cdot \mathbf{T} = 0$ ,  $t_1$  and  $t_2$  can be written in terms of  $n$  and  $m$  as

$$t_1 = \frac{2m+n}{d_R} \quad \text{and} \quad t_2 = -\frac{2n+m}{d_R}, \quad (4)$$

where  $d_R$  is the greatest common divisor of  $(2m+n)$  and  $(2n+m)$ .

Introducing  $d$  as the greatest common divisor of  $n$  and  $m$ , then we can get  $d_R$  as

$$\begin{aligned} d_R &= d \text{ if } n-m \text{ is not a multiple of } 3d \\ &= 3d \text{ if } n-m \text{ is a multiple of } 3d \end{aligned} \quad (5)$$

The electrical properties of the nanotube is determined by its geometrical structure. Figure 1-2 shows the reciprocal lattice of graphene. The SWNT reciprocal lattice vectors are  $\mathbf{K}_1$  and  $\mathbf{K}_2$ . The reciprocal lattice vector  $\mathbf{K}_1$  corresponds to the circumferential direction and  $\mathbf{K}_2$  corresponds to the longitudinal direction. As a result, the following relations between  $\mathbf{C}_h$ ,  $\mathbf{T}$ ,  $\mathbf{K}_1$ , and  $\mathbf{K}_2$  exist:

$$\begin{aligned} \mathbf{C}_h \cdot \mathbf{K}_1 &= 2\pi, & \mathbf{T} \cdot \mathbf{K}_1 &= 0 \\ \mathbf{C}_h \cdot \mathbf{K}_2 &= 0, & \mathbf{T} \cdot \mathbf{K}_2 &= 2\pi \end{aligned} \quad (6)$$

From these relations, we can get the expressions for  $\mathbf{K}_1$  and  $\mathbf{K}_2$  as

$$\mathbf{K}_1 = \frac{1}{N}(-t_2 \mathbf{b}_1 + t_1 \mathbf{b}_2), \quad \mathbf{K}_2 = \frac{1}{N}(m \mathbf{b}_1 - n \mathbf{b}_2), \quad (7)$$

where  $\mathbf{b}_1$  and  $\mathbf{b}_2$  are the reciprocal lattice vectors of graphene given by

$$\mathbf{b}_1 = \left( \frac{2\pi}{\sqrt{3}a}, \frac{2\pi}{a} \right), \quad \mathbf{b}_2 = \left( \frac{2\pi}{\sqrt{3}a}, -\frac{2\pi}{a} \right), \quad (8)$$

and  $N$  is the number of hexagons in a unit cell of the nanotube given by

$$N = \frac{|\mathbf{C}_h \times \mathbf{T}|}{|\mathbf{a}_1 \times \mathbf{a}_2|} = \frac{2(m^2 + n^2 + nm)}{d_R} = \frac{2L^2}{a^2 d_R} \quad (9)$$

Figure 1-3A shows the Brillouin zone of graphene and  $\Gamma$ ,  $K$  and  $M$  are high symmetry points which correspond to the center, the corner, and the center of the edge, respectively. The energy dispersion relations for graphene throughout the whole region of the Brillouin zone are shown in Figure 1-3B. The allowed wavevectors in the direction of  $\mathbf{K}_2$  in Figure 1-2 are continuous for an infinitely long nanotube. In the circumferential direction, however, there are  $N$  discrete allowed wavevectors. When the allowed wavevectors in the circumferential direction include the  $K$  point which is shown in Figure 1-3, the nanotube is metallic. In other words, the valence band and conduction bands meet each other. This corresponds to the condition,

$$(n - m) \text{ is a multiple of } 3 \quad (10)$$

For all other cases, the nanotube is semiconducting. Furthermore, the bandgap of semiconducting nanotubes is inversely proportional to their diameter [7, 44].

### Single-Walled Carbon Nanotube Growth Methods

Several growth methods have been developed to synthesize carbon nanotubes, namely arc discharge, laser ablation, and chemical vapor deposition (CVD). In the arc discharge method, a voltage around 25 V is applied to two carbon rod electrodes with a separation  $\sim 1$  mm. A high current flows between the two electrodes in a helium atmosphere. The carbon at the anode evaporates and condenses at the cathode and forms nanotubes. To synthesize SWNTs, transition metals such as Co, Ni, and Fe are used as catalyst material on the electrode. The as-grown SWNTs have few defects because of the high temperature during growth ( $\sim 3,000^\circ \text{C}$ ) and their

diameters are usually small and their diameter distribution is narrow. However, this method produces many by-products such as fullerenes and amorphous carbon, so a purification process is required after growth [6, 9].

The laser ablation method uses a laser to synthesize nanotubes. A pulsed laser vaporizes the graphite target inside a tube furnace ( $\sim 1,200^\circ\text{C}$ ). To obtain SWNTs, transition metals are added to the graphite target. Argon or other inert gases flow to the tube to carry the grown nanotubes to the water-cooled copper collector. This growth method produces many by-products similar to the arc discharge method. Nanotubes grown by both arc-discharge and laser ablation methods are usually bundled due to van der Waals forces. To get individual nanotubes for device applications, post processing such as sonication is needed to break up the bundles [10, 45].

Chemical vapor deposition (CVD), however, does not suffer from these problems. The schematic and the picture of the CVD system are shown in Figure 1-4. CVD needs transition metals as catalysts to nucleate nanotubes. The transition metals are typically dissolved in liquid solution and deposited on a sample. Then the sample is put inside a furnace and heated up to  $\sim 900^\circ\text{C}$ . The feedstock gases  $\text{C}_2\text{H}_4$  and  $\text{CH}_4$  are flown at  $\sim 900^\circ\text{C}$  to supply the necessary carbon. The diameter of the as-grown nanotubes are typically determined by the catalyst size. Therefore, the catalyst condition is very important during SWNT growth. The chemical vapor deposition method can produce pristine and isolated nanotubes [12].

### **GaN Nanowires**

GaN-based III-V nitride semiconductor materials have attracted significant research attention due to their unique properties, such as high breakdown field, large mobility, high drift velocity, good thermal conductivity, and good chemical and physical stability [30, 46, 47]. More importantly, AlGaInN family of III-V nitride semiconductor alloys have a direct energy

bandgap, which varies between 6.2 eV and 1.95 eV depending on their composition, as shown in Figure 1-5. . As a result, GaN-based III-V nitride semiconductors cover the wavelengths from the green into UV, and have applications in blue/green/UV light-emitting diodes (LEDs) in full-color displays, traffic lights, automotive lighting, and in white LEDs for room lighting [46, 48-61]. Furthermore, blue/green laser diodes [62-69] can be used in high storage-capacity DVDs. In addition, AlGaIn-based photodetectors [70-76] can be used in solar-blind UV detection and have potential for a wide range of applications, such as flame sensors for control of gas turbines and for detection of missiles.

In addition to these well-established applications, there are also many newer applications of III-V nitride semiconductor materials. For example, UV LEDs or laser diodes based on III-V nitrides can be employed as UV optical sources for use in airborne chemical and biological sensing systems, allowing direct multi-wavelength spectroscopic identification and monitoring of UV-induced reactions [48, 77]. The UV wavelengths are necessary in order to cause fluorescence in many of the targeted chemicals and biological agents. This would enable the manufacturing of compact biological or chemical agent warning sensors with fast response and high detection sensitivity.

Furthermore, simple Schottky diode or field-effect transistor structures fabricated in GaN are sensitive to a number of gases, including hydrogen and hydrocarbons. As a result, GaN-based III-V nitride materials can also be used as wide bandgap semiconductor sensors for gas detection. These detectors would have use in automobiles, aircraft, fire detectors, and in diagnosis of exhaust and emissions from industrial processes. The nitrides are also well-suited to high temperature applications because of their wide bandgaps and low intrinsic carrier concentrations. As a result, wide bandgap electronics and sensors based on GaN can operate at

elevated temperatures (600°C, or 1112°F) where conventional silicon (Si)-based devices cannot function. The ability of these materials to function in high temperature, high power, and high energy radiation conditions will enable large performance enhancements in a wide variety of sensing applications where uncooled operation is essential. Uncooled GaN electronics and sensors will reduce sensor package weights and cost and increase functional capabilities [78]. Given the high cost per weight of transporting sensors to remote environments, the weight savings gained by using wide bandgap devices could have large economic implications in the energy and space industries.

Furthermore, III-V nitride materials have significant advantages for high power device applications due to their very high breakdown field, allowing the devices to support large voltages for high power operation [49, 79-81]. For example, they can be used in power amplifiers and monolithic microwave integrated circuits (MMICs) as a part of high performance radar units and wireless broadband communication links, and as ultra high power switches for the control of distribution on electricity grid networks.

Although GaN and related III-V nitride materials in thin film form have been well-established for many of the applications listed above, they have some significant shortcomings:

- 1) It is very expensive to grow thin film GaN-based III-V nitride materials since it requires sophisticated growth equipment such as metalorganic chemical vapor deposition (MOCVD) [82-85] or molecular beam epitaxy (MBE) [86-89].

- 2) It is very expensive to fabricate GaN-based III-V nitride devices since it requires advanced lithography and fabrication techniques to pattern these materials into very small nanoscale dimensions [90].

3) The material quality of thin film GaN is still far-from-ideal. Most commercially available III-V nitride materials are currently grown heteroepitaxially on foreign substrates, such as sapphire and SiC, suffering from a high density of dislocations and microstructural defects due to lattice mismatch (See Figure 1-5. for the lattice constants) [61, 91, 92]. These defects act as leakage paths, nonradiative recombination centers, and impurity and metal migration channels, decreasing device performance. For example, the presence of a high density of dislocations and large residual strain in GaN has been proven to be the limiting factor for LED efficiency and reliability [93]. Although small diameter free-standing bulk GaN substrates are now commercially available, sapphire and SiC will likely remain the common substrates for nitride LEDs before large area low-cost GaN wafers become available. Furthermore, the growth of defect-free III-V nitride semiconductor alloys, such as InGaN and AlGaIn, present problems even on free-standing bulk GaN substrates, due to lattice mismatch.

Consequently, the challenge for III-V nitride semiconductors is to find a cheap, large-scale, nonplanar, non-lithographic, and defect-free nanomanufacturing technique which would solve these shortcomings. GaN-based III-V nitride semiconductor nanowires offer a potential solution to this challenge.

Semiconductor nanowires have recently attracted much attention as promising candidates as building blocks for active electronic and photonic devices, such as photodetectors, LEDs, lasers, and biochemical sensors [27, 94-117]. Nanowires of III-V nitride materials do not suffer from the problems listed above for planar III-V nitride thin films. First of all, nanowires can be grown cheaply and in large-scale using a very simple chemical vapor deposition (CVD) approach, as explained in detail in Chapter 5. Secondly, since these nanomaterials naturally have submicron, nanoscale dimensions, there is no need to do lithographic patterning and

microfabrication after growth. Third, because nanowire synthesis is substrate-free, it should prevent formation of dislocations and defects originating from lattice mismatch [118]. This should enable the growth of defect-free III-V nitride alloy nanowires, such as InGaN and AlGaN.

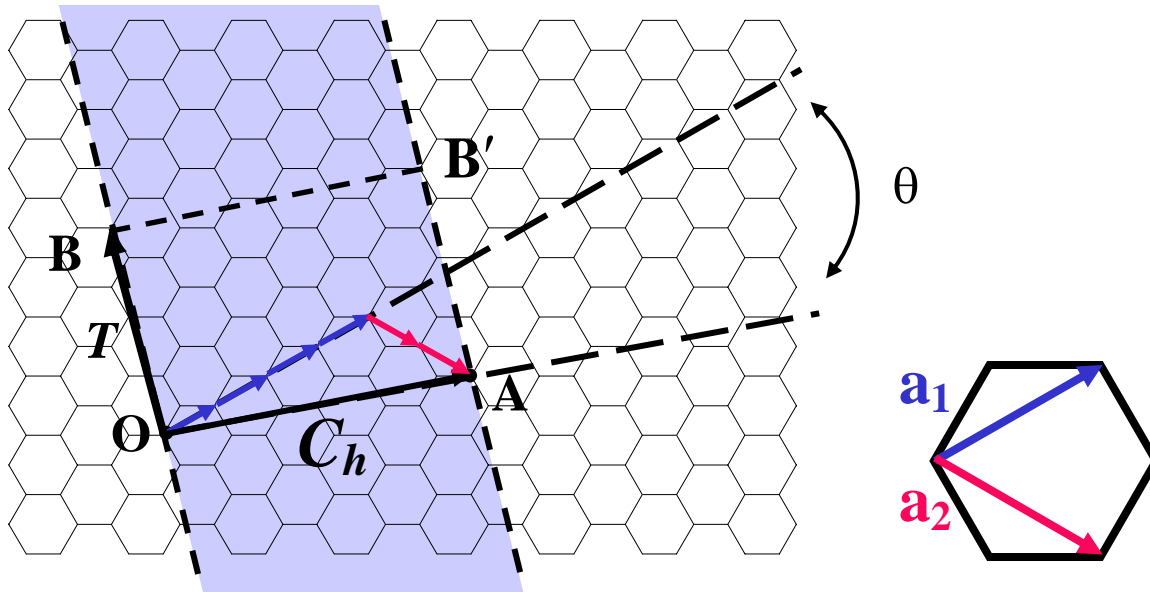


Figure 1-1. Unrolled graphene sheet making up SWNT and its honeycomb lattice.  $C_h$  is the chiral vector and  $T$  is the translational vector. Nanotube is formed when  $O$  is connected to  $A$  and  $B$  is connected to  $B'$ . This structure corresponds to a (4,2) nanotube. Real space unit vectors of graphene,  $a_1$  and  $a_2$ , are shown in the inset on the right.

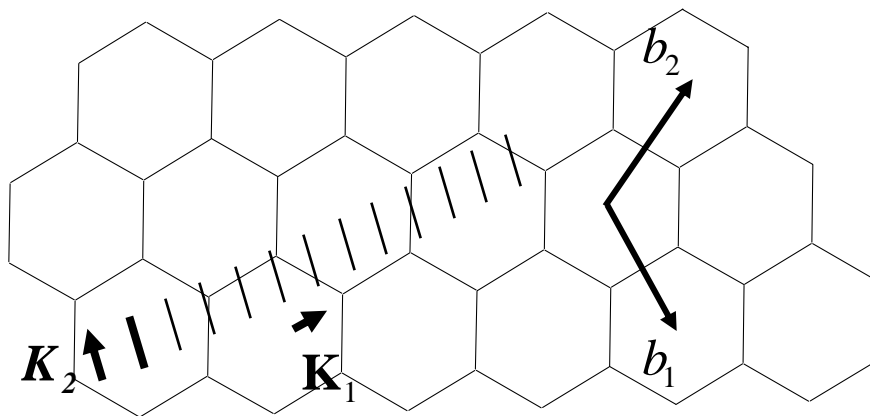


Figure 1-2. Reciprocal lattice of graphene (unrolled carbon nanotube). Reciprocal lattice vectors of SWNT are  $K_1$  and  $K_2$ . The reciprocal lattice vector  $K_1$  corresponds to the circumferential direction and  $K_2$  corresponds to the longitudinal direction.

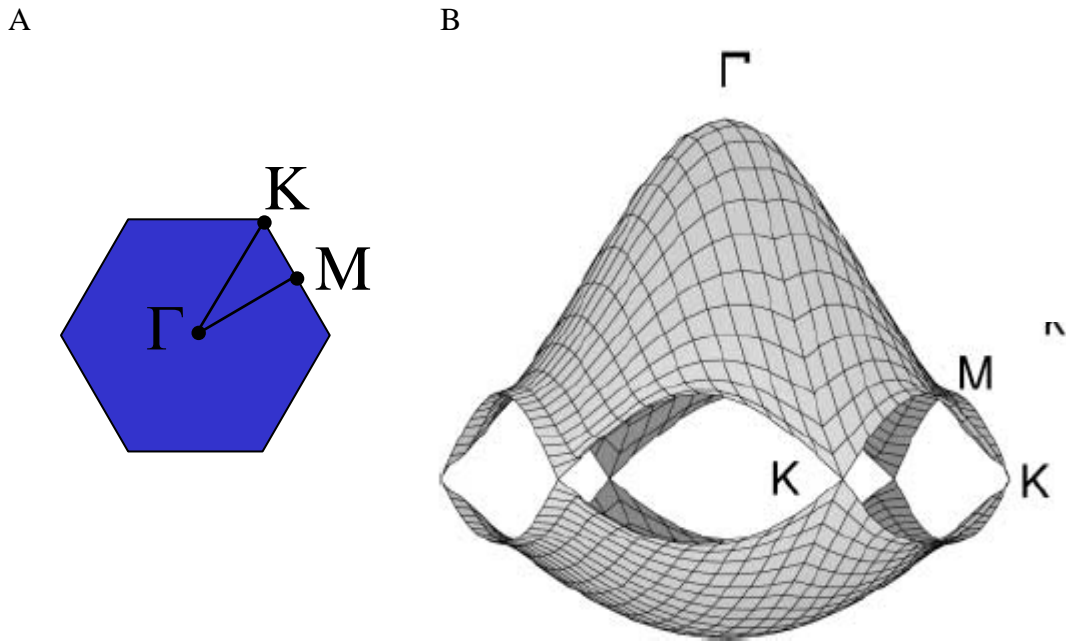


Figure 1-3. Energy dispersion relations for graphen. A) Brillouin zone of graphene.  $\Gamma$ ,  $K$  and  $M$ , are high symmetry points as the center, the corner, and the center of the edge, respectively. B) Energy dispersion relations for graphene shown throughout whole region of the Brillouin zone.

A



B

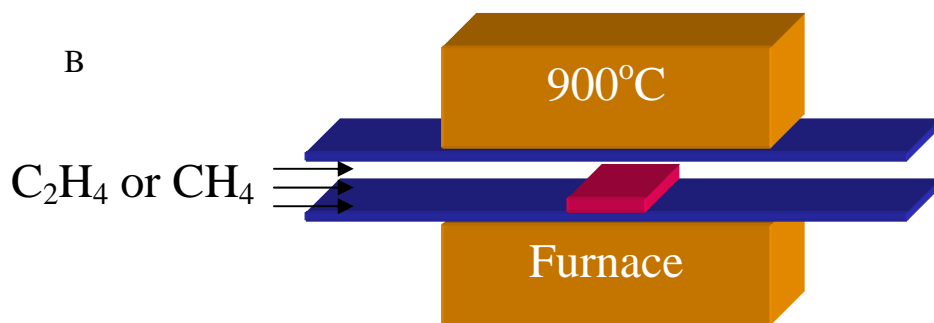


Figure 1-4. Images of CVD system. A) Photograph and B) Schematic of the CVD system used to grow SWNTs. The sample is placed in the 1 inch quartz tube and heated up to 900 °C and annealed for 2 min in Ar and H<sub>2</sub> atmosphere. Feedstock gases C<sub>2</sub>H<sub>4</sub> and CH<sub>4</sub> are then flown at 900 °C to grow nanotubes on the sample.

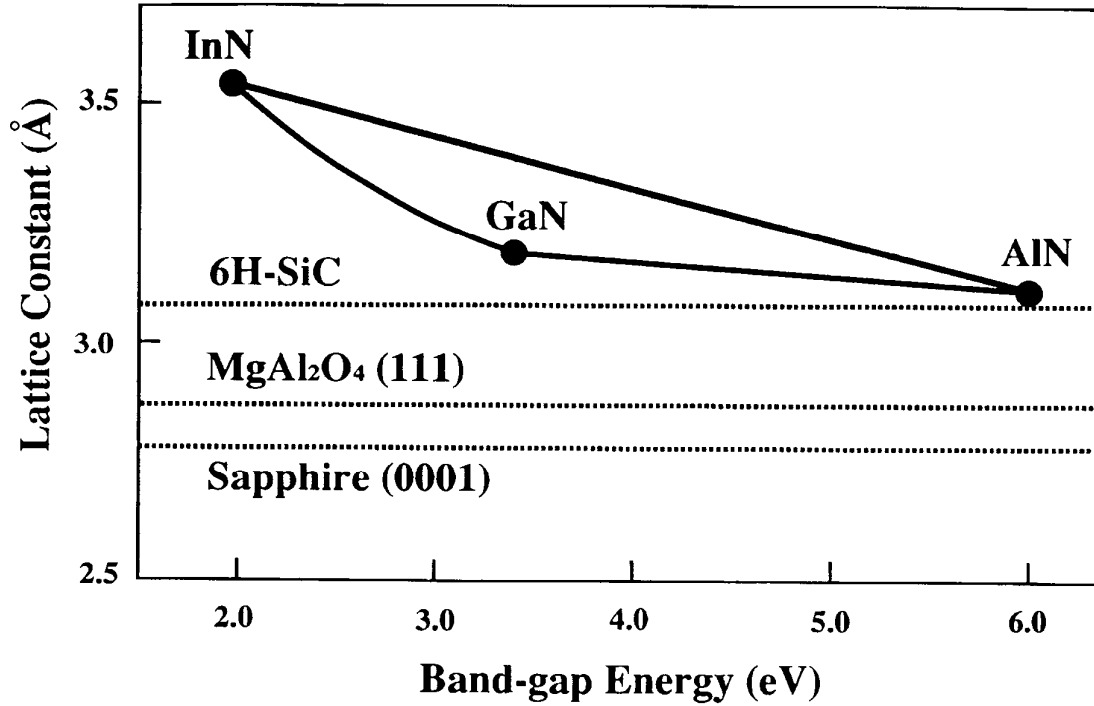


Figure 1-5. Lattice constant of III-V nitride semiconductor materials as a function of their bandgap energy. Also shown for reference are the lattice constants of the commonly used substrates (SiC, MgAl<sub>2</sub>O<sub>4</sub>, and sapphire) for the growth of III-V nitride based materials (from Ref. [46]).

## CHAPTER 2 SINGLE-WALLED CARBON NANOTUBE GROWTH FROM ION IMPLANTED IRON CATALYST

### **Introduction**

An essential component of the CVD growth process is the catalyst material placed on the substrate for nucleating the growth of carbon nanotubes. Typically, transition metal nanoparticles, such as nickel (Ni), iron (Fe), and cobalt (Co), are used as catalyst. For SWNT growth, catalyst is usually spun on or drop-dried from a liquid solution containing iron nanoparticles [11]. More recently, solid thin film layers deposited by evaporation or sputtering have also been used as catalyst [119]. In order to control the origin of nanotubes during CVD growth, the catalyst is typically patterned by lithography into small “islands” [11]. However, it is not possible to pattern the liquid solution-based catalyst into very small dimensions or the thin film catalyst into nonplanar three-dimensional (3D) device structures, such as the sidewalls of high aspect ratio trenches.

In this chapter, we demonstrate that ion implantation, a well-established technique in silicon microfabrication, and subsequent annealing can be used as an alternative method to create catalyst nanoparticles. Ion-implanted catalyst is much easier to pattern into very small features and over high aspect ratio topography compared to other types of catalyst, and it offers extremely accurate control of the number of atoms introduced into the substrate (the dose). Since ion implantation is very reproducible, easily scalable, and compatible with standard silicon microfabrication, it could offer significant technological advantages as a method to form catalyst nanoparticles.

In this chapter, we first introduce ion implantation and liquid-based catalysts for SWNT growth. We then present experimental evidence that single-walled carbon nanotubes can indeed be produced by the process of Fe ion implantation into thermally grown SiO<sub>2</sub> layers,

subsequent annealing, and CVD growth. Finally, we systematically characterize the effect of implantation dose and energy on the structural properties of the catalyst nanoparticles and SWNTs that are formed.

### **Ion Implantation**

Ion implantation is one of the well-established techniques in silicon device fabrication. In the implantation process, ions or molecules are accelerated to high energy and directly introduced into the substrate. The first benefit of this technique is the ability to control the depth of ions implanted into the substrate. To get ions implanted deeper, the accelerating voltage can be increased. The second benefit is the ability to control the quantity of ions implanted. For higher number of ions, the implantation time can be increased. The number of implanted ions can be counted precisely. The ions implanted follow a random trajectory and get scattered by other atoms before losing their energy, which results in a Gaussian-like distribution. The average depth of the implanted ions is called the projected range,  $R_p$ . The total number of ions implanted per unit area is called the dose. As an example, Figure 2-1 shows the distribution of several different ion species implanted into crystalline silicon at an energy of 200 kV.

### **Liquid-Based Catalyst**

The most commonly used catalysts for the CVD growth of SWNTs are liquid-based catalysts. As an example of such a catalyst, Figure 2-2A shows the AFM image of iron nitrate/IPA liquid catalyst after dispersion on a  $\text{SiO}_2$  substrate and Figure 2-2B shows the AFM image of the nanotubes grown from this catalyst by CVD. As mentioned previously, one significant problem with this catalyst is that it is not possible to pattern it into very small dimensions and over high aspect ratio topography.

## Experimental Procedure

500 nm thick SiO<sub>2</sub> layers were first thermally grown on silicon (100) substrates. Fe<sup>+</sup> ions were implanted into these layers at an energy of 60 keV with three different doses (10<sup>14</sup>, 10<sup>15</sup>, and 10<sup>16</sup> cm<sup>-2</sup>) and at a dose of 10<sup>15</sup> cm<sup>-2</sup> with three different energies (25, 60, and 130 keV). The projected range  $R_p$  of the 25, 60, and 130 keV implants in SiO<sub>2</sub> are 23.9, 49.9, and 103.4 nm, respectively, based on SRIM [120] calculations. The as-implanted samples were placed in a 1-inch quartz tube furnace and annealed at 900°C under 300 sccm Ar and 200 sccm H<sub>2</sub> flow for 2 minutes to form the catalyst nanoparticles. (The schematic and photograph of the furnace is shown in Figure 1-4). After annealing, nanotubes were grown at the same temperature by discontinuing the Ar flow and introducing CH<sub>4</sub> at 200 sccm. The co-flow of H<sub>2</sub> remained constant at 200 sccm, and the growth lasted for 10 min. The catalyst nanoparticles and nanotubes obtained were characterized by a Digital Instruments Nanoscope III Atomic Force Microscope (AFM), a JEOL 2010F High Resolution Transmission Electron Microscope (HRTEM) operating at 100 kV, and a Renishaw Raman spectroscopy system.

## Results and Discussion

### AFM Characterization

The AFM images of Figure 2-3A, B, and C show the Fe catalyst nanoparticles formed on the SiO<sub>2</sub> surface from implants of three different doses at 60 keV, after annealing the as-implanted substrates at 900°C for 2 minutes. The average height and density of these nanoparticles are listed in Table 2-1.

Figure 2-3 shows that the low (10<sup>14</sup> cm<sup>-2</sup>) implant dose results in very low density of catalyst particles, whereas the high (10<sup>16</sup> cm<sup>-2</sup>) implant dose results in very large particle size. For the medium (10<sup>15</sup> cm<sup>-2</sup>) dose sample, on the other hand, both small height (~2 nm) and high density Fe nanoparticles are obtained. Using a simple model, the flux of Fe atoms diffusing to

the oxide surface under high temperature is proportional to the dose of the implant. As a consequence too little flux (e.g.  $10^{14}$  cm<sup>-2</sup> dose sample) results in too few particles, and too much flux (e.g.  $10^{16}$  cm<sup>-2</sup> dose sample) results in the aggregation of Fe atoms into larger clusters. Furthermore, we have also studied the effect of implant energy at a dose of  $10^{15}$  cm<sup>-2</sup> on the catalyst particle size and density, as presented in Table 2-1 and Figure 2-4. The low (25 keV) implant energy results in a very high density of catalyst particles with slightly larger average size than those obtained from the medium (60 keV) implant energy, whereas the high (130 keV) implant energy results in very large particle size and low density.

The AFM images of Figure 2-3D,E, and F show the carbon nanotubes grown by CVD at 900°C from the catalyst nanoparticles implanted with 60 keV and  $10^{14}$ ,  $10^{15}$  and  $10^{16}$  cm<sup>-2</sup> dose, respectively. As seen in Figure 2-3D, no nanotubes were grown on the low dose sample, consistent with the very low density of catalyst nanoparticles on that sample. The high and medium dose samples, on the other hand, produced nanotubes with a similar average diameter (2.2 nm), although the density of nanotubes was much less for the high dose sample compared to the medium dose one (See Figure 2-3 and Table 2-1). This is due to the presence of a few small (~2 nm) catalyst nanoparticles on the high dose sample, despite the fact that the average catalyst size is much larger (15 nm).

We have also studied the effect of implant energy at a dose of  $10^{15}$  cm<sup>-2</sup> on the nanotube diameter and density. As shown in Figure 2-4, the high implant energy did not produce any nanotubes due to the very large particle size, and the low implant energy resulted in nanotubes which have a slightly larger average diameter (~3 nm) than the medium energy sample, consistent with the slightly larger catalyst size [121]. We can define the nanotube yield as the number of nanotubes grown per unit area divided by the number of catalyst nanoparticles per

unit area. By this definition, the yield for the 60 keV and 25 keV implants are 0.035 and 0.009, respectively. The yield for the 60 keV implant is about 4 times higher than the 25 keV implant. This could be due to two reasons: The first reason could be that the nanotube yield is a function of catalyst size, and the yield decreases as the average catalyst height increases. Previous studies have observed that smaller Fe catalyst nanoparticles tend to be more active in producing single-walled carbon nanotubes (SWNTs) compared to larger ones [122, 123]. They suggest that this could be due to small nanoparticles allowing carbon supersaturation and facilitating nanotube growth more readily. The larger average catalyst nanoparticle height could partly explain why the yield is lower for the 25 keV implant.

Secondly, the catalyst nanoparticle height and density as shown in Table 2-1 is measured after the 2 min anneal at 900°C, but before the nanotube growth step. During the 10 min nanotube growth step (also at 900°C), the implanted Fe atoms continue to out-diffuse towards the surface, and as a result, the catalyst nanoparticle density and height continue to evolve as the growth proceeds. This is in contrast to solution-based catalyst, where the catalyst “dose” on the surface does not change during growth. To see how much the catalyst nanoparticle density changes during the 10 min nanotube growth, we have measured by AFM, the average density of catalyst nanoparticles after growth for both the 25 keV and 60 keV implants, as shown in Table 2-2.

We can clearly see from Table 2-2 that the catalyst density decreases for the 25 keV implant, whereas it increases for the 60 keV implant as the growth proceeds, becoming comparable at the end of the growth step. The density increase for the 60 keV case could be explained by more Fe out-diffusing to the oxide surface. The density decrease in the 25 keV

case can be explained by Fe nanoparticles aggregating into larger and fewer clusters due to a high Fe surface concentration resulting from out-diffusion.

If we calculate the yield based on the nanotube density after growth, we get 0.015 and 0.013 for the 60 keV and 25 keV implants, respectively, resulting in yield values which are almost identical within experimental error. Along with catalyst height dependent yield, the continued out-diffusion of Fe during the nanotube growth could explain the observed discrepancy in yield between the 25 and 60 keV implants. These experimental findings suggest that a lower implant energy does not necessarily result in a higher nanotube density.

### **TEM Characterization**

In order to verify by HRTEM that the nanotubes grown from ion implanted catalyst are single-walled, we have fabricated special micromachined silicon substrates with narrow open slits on them, as shown in Figure 2-5A and B.[124-126] The fabrication of the TEM grid will be discussed in detail in Chapter 3. Briefly, 350 nm oxide was grown on both the front and the back side of a (100) Si wafer and thin membranes of 1 mm<sup>2</sup> area were wet-etched using a buffered oxide etch (BOE) solution. 1 mm<sup>2</sup> windows etched from the back side silicon using a TMAH solution until ~15 μm thick silicon membranes remain. Narrow open slits of width ranging from 1.5 to 4.5 μm are dry etched on the top side oxide and open slits of the same dimension are dry etched in silicon from the top using a deep silicon etcher. Following the etch, the wafer is implanted with 60 keV, 10<sup>15</sup> cm<sup>-2</sup> Fe<sup>+</sup> ions. After dicing the wafer, the resulting SiO<sub>2</sub>/Si substrates are annealed and grown by CVD, following the same procedure given above. The nanotubes grown on these substrates are completely suspended over the width of the slits, enabling direct TEM characterization of as-grown SWNTs from ion implanted catalyst. The HRTEM images we have obtained show clear evidence that the as-grown nanotubes are single-

walled with a diameter range in agreement with the AFM data [See Figure 2-5C and D]. The reason that only SWNTs are obtained is due to the particular growth condition used. Previous work in the literature by several groups has also obtained only SWNTs using growth conditions similar to the one used in this work [121-123]. For example, Liu et al. have grown nanotubes (using monodispersed Fe-Mo nanoparticles as catalyst) by CVD at 900°C under hydrogen and methane flow. SWNT growth was observed when the average catalyst size was 3.6 nm, but no growth occurred when the average catalyst size was 8.5 nm [123]. Furthermore, using identical growth conditions as in our case (i.e. 900°C, 200 sccm methane and 200 sccm hydrogen) and discrete iron oxide nanoparticles as catalyst, Dai et al. found that no nanotubes (including multi-walled) were produced for large nanoparticles (> 5 - 6 nm) [122]. In addition, Lieber et al. has found that a low supply of carbon precursor gas produces only small diameter SWNTs even when the catalyst also contains large iron nanoparticles [121]. Furthermore, theoretical work by Kanzow et al. has suggested that for MWNT growth, one requires large catalyst particle size, high carbon supply, and lower temperatures [127]. The condition of high carbon supply and lower temperatures is not met in our growth condition. In fact, the growth conditions used in this work were chosen based on the literature and our previous experiments with solution-based Fe catalyst in order to be able to obtain only SWNTs. In short, the fact that multi-walled nanotubes and larger single-walled nanotubes are not formed in our growth can be explained by the particular growth condition used and this observation is consistent with previous work in the literature using similar growth conditions.

### **Raman Spectroscopy Characterization and Discussion**

We have also characterized the nanotubes grown from the ion implanted catalyst (60 keV,  $10^{15} \text{ cm}^{-2} \text{ Fe}^+$ ) using micro-Raman spectroscopy, as shown in Figure 2-6. The Raman spectra were obtained by a Kr ion laser with an excitation wavelength of 647.1 nm and a spot

size of about 1  $\mu\text{m}$ . The observation of characteristic multi-peak tangential mode (G band) features around  $1580\text{ cm}^{-1}$  provides a signature of single-walled nanotubes [128]. A Lorentzian fit of the G-band spectrum in Figure 2-6 yields peaks at  $1570$ ,  $1579$ , and  $1593\text{ cm}^{-1}$ . Furthermore, a Radial Breathing Mode (RBM) peak at  $200\text{ cm}^{-1}$  is observed, as shown in the inset of Figure 2-6, which corresponds to a SWNT diameter of around  $1.2\text{ nm}$  [128], falling within the diameter range of  $0.8\text{-}3.5\text{ nm}$  obtained by AFM. Raman measurements performed at a fixed laser energy give an idea of nanotubes that are in resonance with the particular laser line used, but do not give a complete characterization of the diameter distribution in a sample, since resonant Raman experiments only detect nanotubes whose electronic energy spacings between van Hove singularities match the laser excitation energy [128, 129]. AFM and HRTEM analysis, on the other hand, give a more complete characterization of the diameter distribution of nanotubes in a sample. Nonetheless, Raman data provides an independent confirmation of the existence of SWNTs in a sample and remains a very useful analytical tool for nanotube characterization. The radial breathing mode (RBM) Raman features, typically appearing between  $120\text{-}250\text{ cm}^{-1}$  for SWNTs with diameters between  $1\text{-}2\text{ nm}$  correspond to the atomic vibration of the carbon atoms in the radial direction.

For isolated SWNTs on an oxidized silicon substrate, the following relationship has been found between the RBM peak frequency  $\omega_{RBM}$  and the SWNT diameter  $d_t$ ,

$$\omega_{RBM} = 248 / d_t, \quad (11)$$

where  $\omega_{RBM}$  is in units of  $\text{cm}^{-1}$  and  $d_t$  is in units of  $\text{nm}$  [128, 129]. However, for  $d_t < 1$ , this relationship is not expected to hold due to nanotube lattice distortions leading to a chirality dependence of  $\omega_{RBM}$ , and for large diameter SWNTs with  $d_t > 2\text{ nm}$ , the intensity of the RBM feature is weak and is hardly observable [128, 129]. As a result, diameter characterization

using the RBM features is typically limited to  $1 < d_t < 2$  nm. Furthermore, as mentioned above, an observable Raman signal from a SWNT can only be obtained when the energy of the laser line used is equal to the energy separation between van Hove singularities in the valence and conduction bands [128, 129]. As a result, for a given laser energy, Raman analysis can only observe SWNTs with certain diameters. A plot of the optically allowed transition energies versus the nanotube diameter, known as the Kataura plot [128-130], is shown in Figure 2-7. By drawing a line at  $E_{ii} = 1.92$  eV in Figure 2-7 (which corresponds to the  $\lambda = 647.1$  wavelength Kr ion laser that we have used), we can find out which nanotube diameters are in resonance with our laser. In the diameter range  $1 < d_t < 2$  nm, only diameters between approximately 1.2-1.35 nm and 1.6-1.8 nm would be observable with the particular laser energy we are using. The inset of Figure 2-6 shows a peak at  $\omega_{RBM} = 200$   $\text{cm}^{-1}$ , which using the equation (12) corresponds to  $d_t \cong 1.2$  nm. This is indeed in the diameter range 1.2-1.35 nm observable by our laser energy.

We found during Raman characterization that in most cases the RBM features were buried under the noise. As a result, we could only characterize the diameters of a few nanotubes using the RBM Raman features. (In contrast, we have characterized the diameters of about 200 nanotubes by AFM.) In the other few cases, we have also observed RBM peaks at frequencies corresponding to diameters of around 1.2-1.3 nm. As a result, the significance of the 1.2 nm diameter value is not that it is the modal value, but it is the value detectable by our Raman laser energy. The Raman RBM data we have obtained is not sufficient to give a statistical characterization of the nanotube diameters, but provides an independent confirmation of the existence of SWNTs in our samples. For the  $60\text{keV}/10^{15}\text{cm}^{-2}$  implant condition, the diameter range of nanotubes measured by AFM was found to be between 0.8 and 3.5 nm, with a mean of 2.2 nm (as tabulated in Table 2-1) and a standard deviation of 0.6 nm. As a result, the 1.2 nm

nanotubes observed by Raman RBM features fall within the diameter range observed by AFM. Although the nanotubes shown in the HRTEM images of Figure 2-5 have diameters around 2-2.5 nm, we have also observed smaller and larger diameter SWNTs by HRTEM. Our HRTEM characterization yielded a diameter range similar to the one obtained by AFM (i.e. 0.8-3.5 nm).

### **Electrical Characterization**

In addition to structural characterization, we have also measured the electrical characteristics of the as-grown nanotubes from ion-implanted catalyst. For this purpose, the as-grown nanotube sample (implantation condition of  $10^{15}$  cm<sup>-2</sup> dose and  $10^{16}$  keV energy) was patterned by a lithographic process and Au was evaporated on the sample to form electrodes. Figure 2-8 shows the cross-sectional schematic of the process flow for SWNT device fabrication. The as-grown sample has nanotubes randomly distributed on thermally grown SiO<sub>2</sub> on a silicon substrate. The next stage is the spin coating of the lift-off resist (LOR) (Microchem LOR3B), and the photoresist (Shipley S1813) on the sample as shown in Figure 2-8B. Using LOR prevents sidewall coverage and aids in the lift-off process. The next stage is to expose the sample by ultraviolet light through a mask. The mask was designed to have several different sizes of electrode widths and spacings in order to increase the possibility of having individual nanotube connections between the electrodes. The mask layout is shown in Appendix A. Briefly, the mask has four different electrode widths (7, 14, 28 and 100  $\mu$ m) and each width has four different electrode spacings (2, 4, 6, and 10  $\mu$ m). It has about 100 devices in  $\sim 1$  cm<sup>2</sup> area. After exposure, the sample is immersed in the developer (Microchem MF-319) and the exposed photoresist and LOR under that exposed region is removed (Figure 2-8C). The next step is the Au deposition on the sample by e-beam evaporation, as shown in Figure 2-8D. After the deposition, the sample is covered with 100 nm of Au. The final patterning step is the lift-off

process. The sample is immersed in the PG remover (Microchem) and sonicated briefly at low power. Figure 2-8E shows the resulting structure. Figure 2-9 is an optical microscope image showing the top view of the fabricated sample. The width of electrode is 14  $\mu\text{m}$  and the spacing between two electrodes is 6  $\mu\text{m}$ , in this case. Figure 2-10 shows the cross-sectional schematic of the nanotube device and its  $I_{DS}$  vs.  $V_{GS}$  curve. The silicon substrate plays the role of a back gate and the drain voltage is applied to the Au electrode on one end of the nanotube, and the Au electrode on the other end (source) is grounded. As the  $I_{DS}$  vs.  $V_{GS}$  data shows, the device functions as a *p*-type transistor.

### **Conclusions**

In conclusion, we have shown experimental evidence that single-walled carbon nanotubes can be grown by Fe ion implantation into  $\text{SiO}_2/\text{Si}$  substrates, subsequent annealing, and CVD growth. For a given growth condition, there is a dose and energy window in which nanotube growth is observed. This work opens up the possibility of controlling the origin of SWNTs at the nanometer scale using advanced lithography techniques, such as electron-beam lithography, and of integrating nanotubes into nonplanar 3D device structures with precise dose control. Ion implantation could offer significant technological advantages as a method to form catalyst nanoparticles for a wide range of nanoscale device applications.

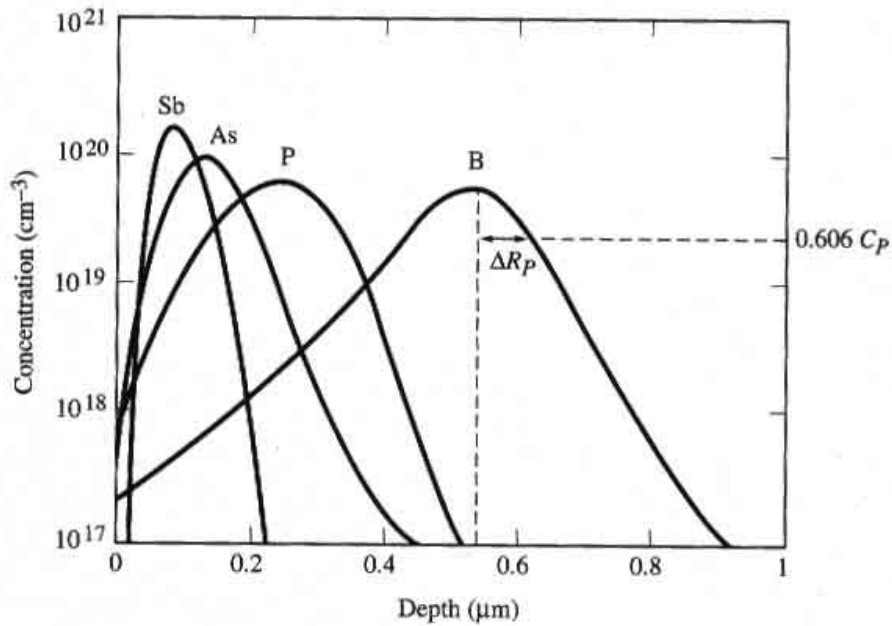


Figure 2-1. Distribution profiles of various ions in crystalline silicon after implantation at an energy of 200 keV. Heavy ions travel shallower and have a narrower distribution than light ions.  $\Delta R_p$  is the standard deviation and  $C_p$  is the peak concentration of the implant. (Adapted from Ref. [131])

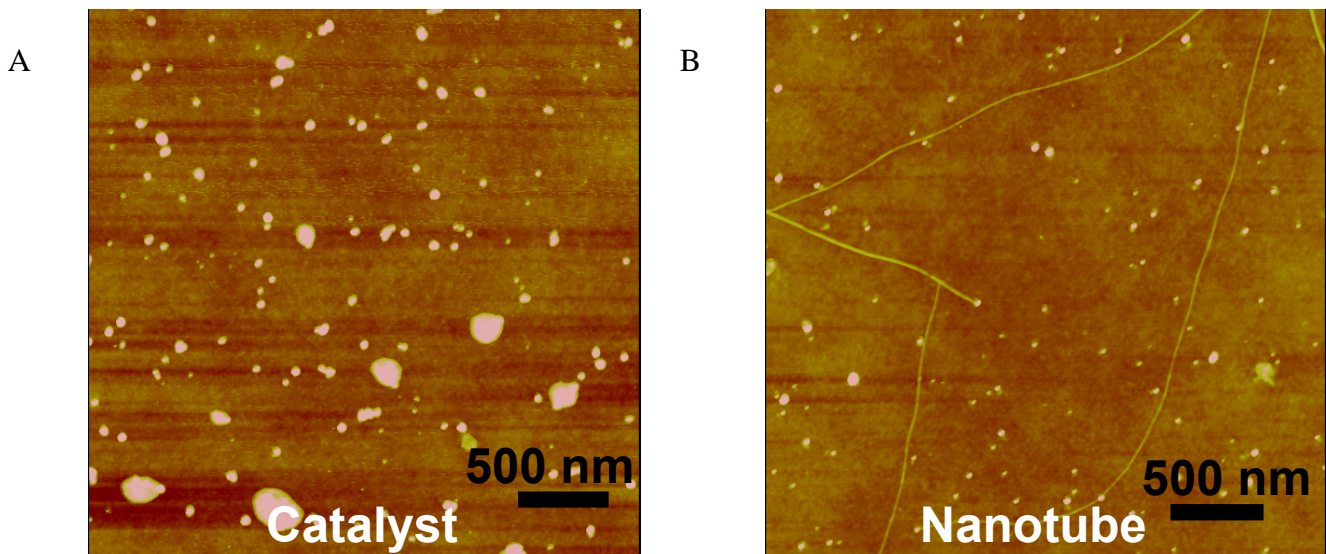


Figure 2-2. AFM image of A) iron nitrate/IPA liquid catalyst dispersed on a  $\text{SiO}_2$  substrate and B) the SWNTs grown from the catalyst of part A.

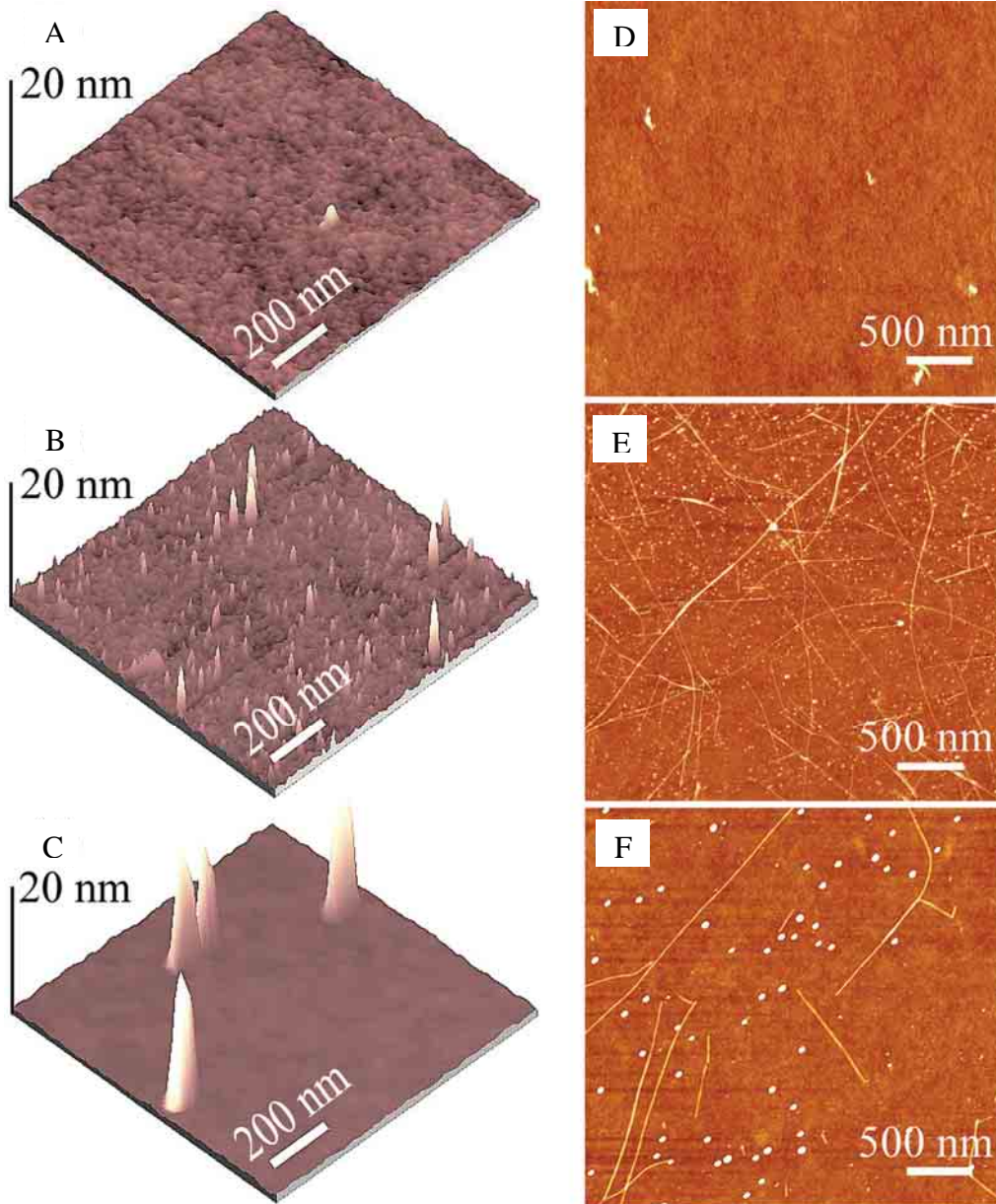


Figure 2-3. AFM images of A-C) Fe catalyst nanoparticles formed after annealing as-implanted  $\text{SiO}_2$  substrates, and D-F) Carbon nanotubes grown by CVD from the catalyst nanoparticles of A-C, respectively. The  $\text{Fe}^+$  implant doses are A, D  $10^{14}$ , B, E  $10^{15}$ , and C, F  $10^{16} \text{ cm}^{-2}$  at an energy of 60 keV.

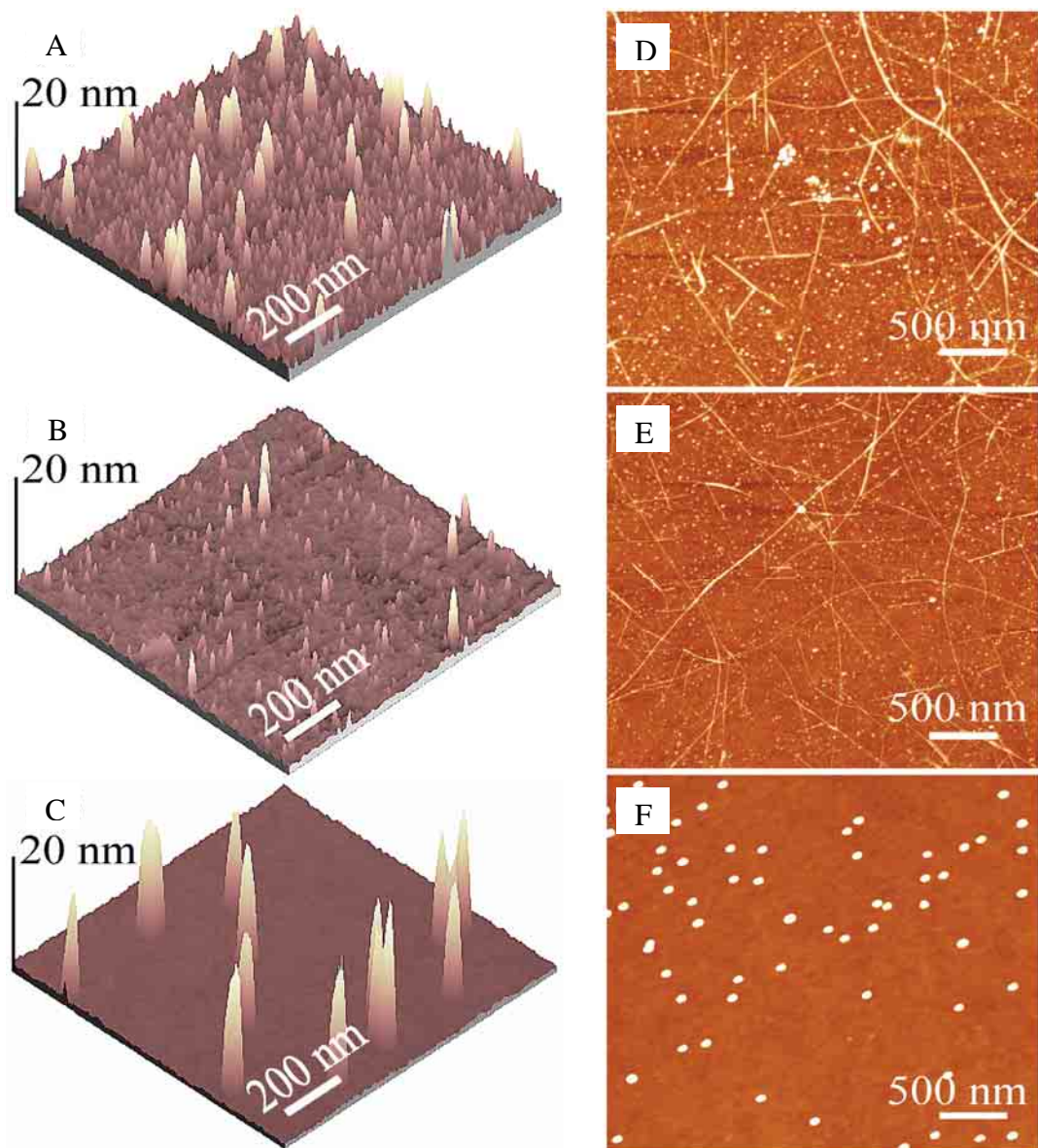


Figure 2-4. AFM images of A-C) Fe catalyst nanoparticles formed after annealing as-implanted SiO<sub>2</sub> substrates, and D-F) Carbon nanotubes grown by CVD from the catalyst nanoparticles of A-C, respectively. The Fe<sup>+</sup> implant energy are A, D 25, B, E 60, and C, F 130 keV with a dose of 10<sup>15</sup> cm<sup>-2</sup>.

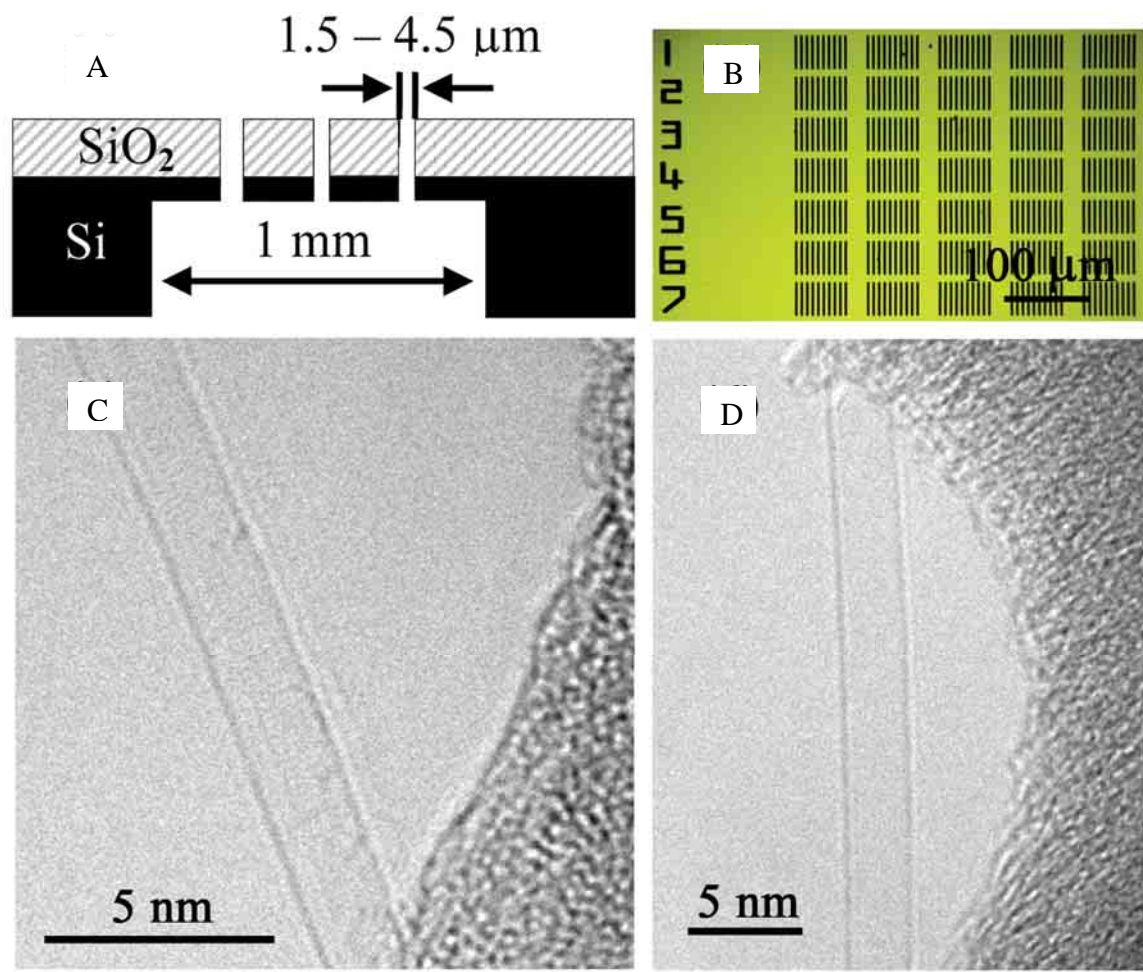


Figure 2-5. Images of as-grown SWNTs. A) Cross-sectional schematic (not to scale) and B) top view optical microscope image of the micromachined Si TEM grids that we have fabricated (not to scale). C), D) HRTEM images obtained from the 60 keV,  $10^{15} \text{ cm}^{-2}$  Fe<sup>+</sup> implanted micromachined TEM grids, showing SWNTs. All of the 85 nanotubes imaged by HRTEM were single-walled, and no multi-walled nanotubes were observed.

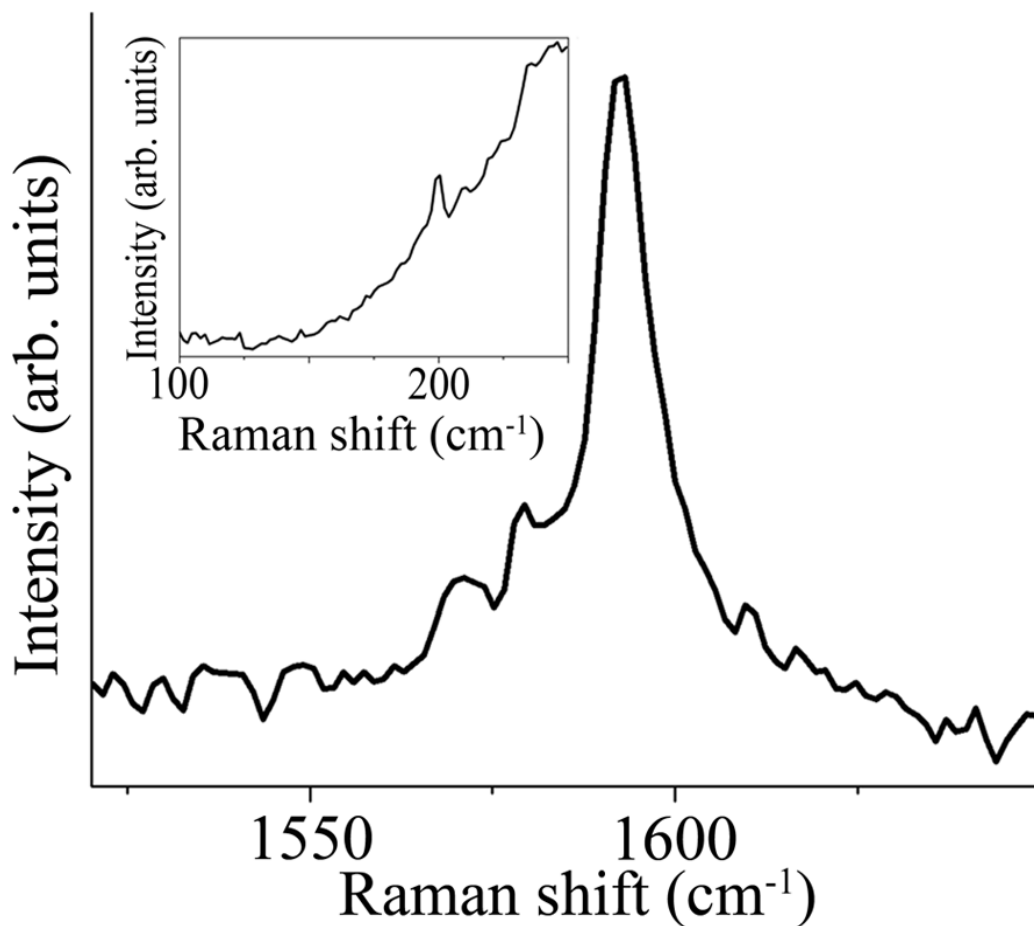


Figure 2-6. Tangential mode (G band) micro Raman spectra of nanotubes grown from 60 keV,  $10^{15}$  cm<sup>-2</sup> Fe<sup>+</sup> implanted catalyst. A Lorentzian fit of the G-band spectrum yields peaks at 1570, 1579, and 1593 cm<sup>-1</sup>. Inset shows Radial Breathing Mode (RBM) Raman spectrum with a peak at 200 cm<sup>-1</sup>, which corresponds to a SWNT diameter of around 1.2 nm [128].

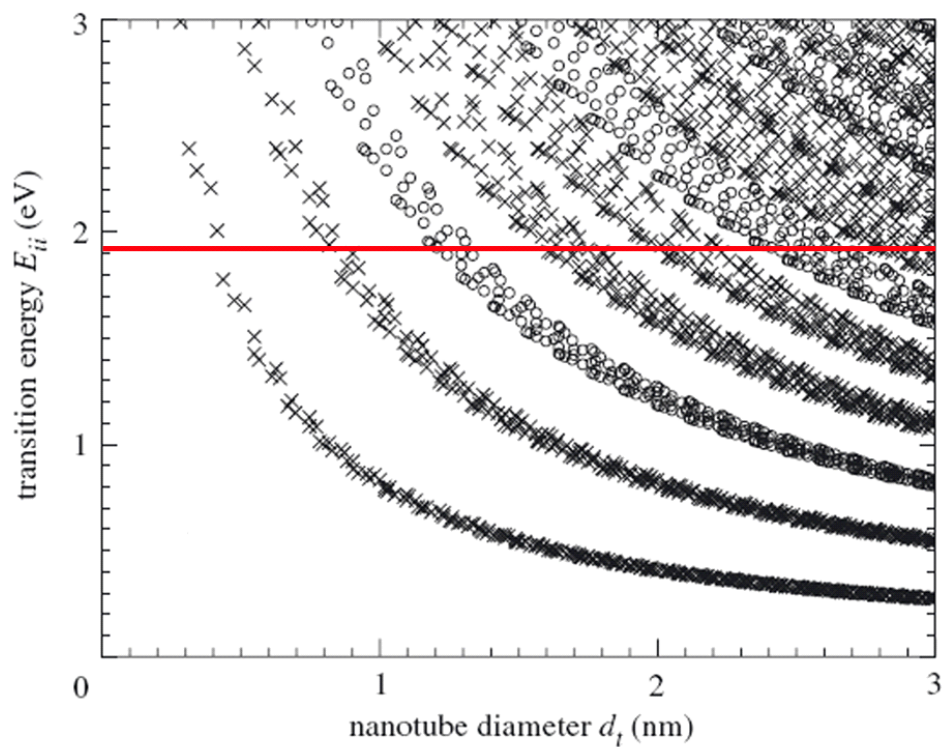


Figure 2-7. Kataura plot showing the electronic transition energies for all possible SWNTs as a function of diameter. Each data point denotes a particular SWNT. The red line is drawn at the laser energy we have used in our Raman experiments. (Adapted from Ref. [128]).

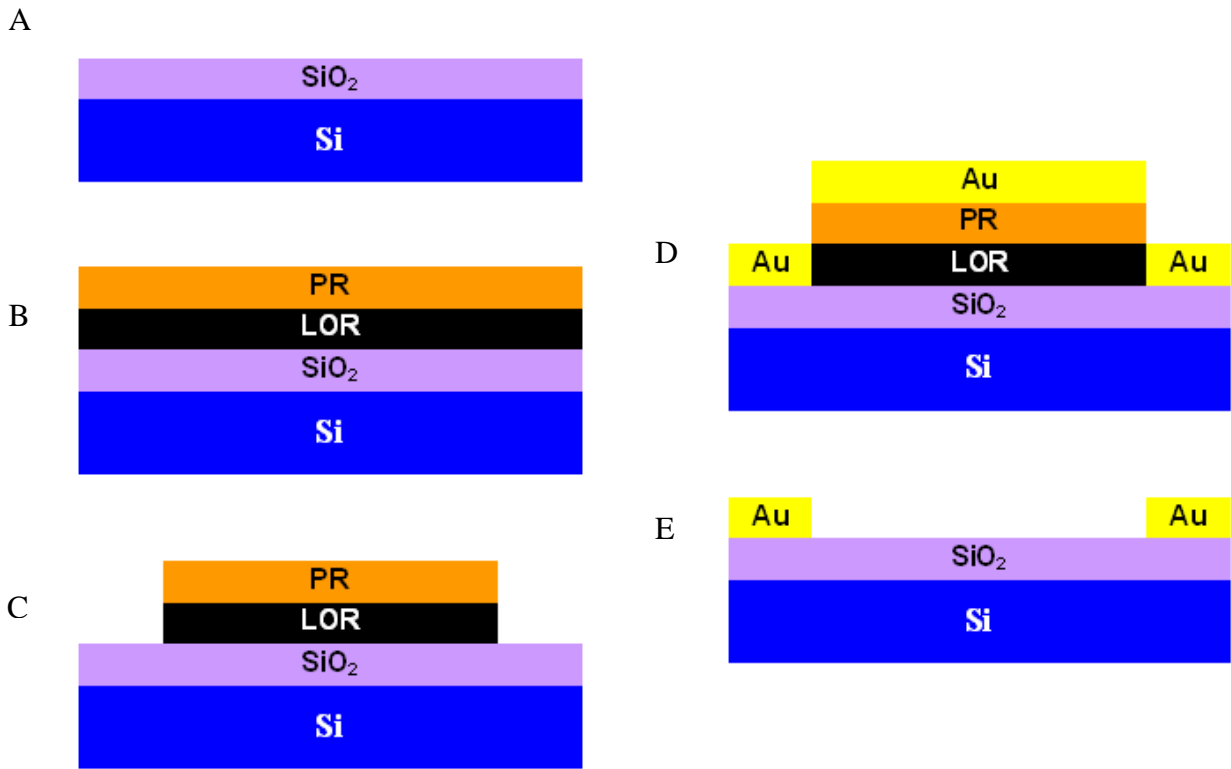


Figure 2-8. Cross-sectional schematic of process flow for SWNT transistor. Figures are not to scale. A) As-grown nanotube sample which has nanotubes randomly distributed on thermally grown SiO<sub>2</sub>. Nanotubes are not shown in the figure. B) Spin coating of the sample with the lift-off resist (LOR) and the photoresist (PR). C) Sample is exposed by ultraviolet light through mask and immersed in developer and the exposed photoresist and LOR under that region is removed. D) Au deposition by e-beam evaporation. 100 nm of Au covers the whole surface of the sample. E) Sample is immersed in PG remover and sonicated briefly at low power. The metal on top of the resist is removed.

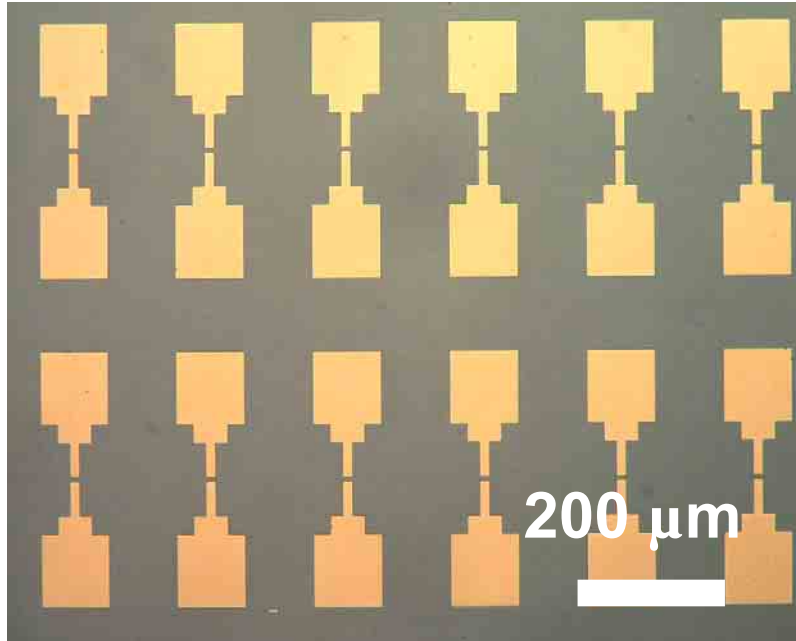


Figure 2-9. Top view optical microscope image of the fabricated nanotube device sample. The yellow area is Au electrodes and the gray area is SiO<sub>2</sub>. The SWNTs are randomly distributed and the number of nanotube connections for each device is random.

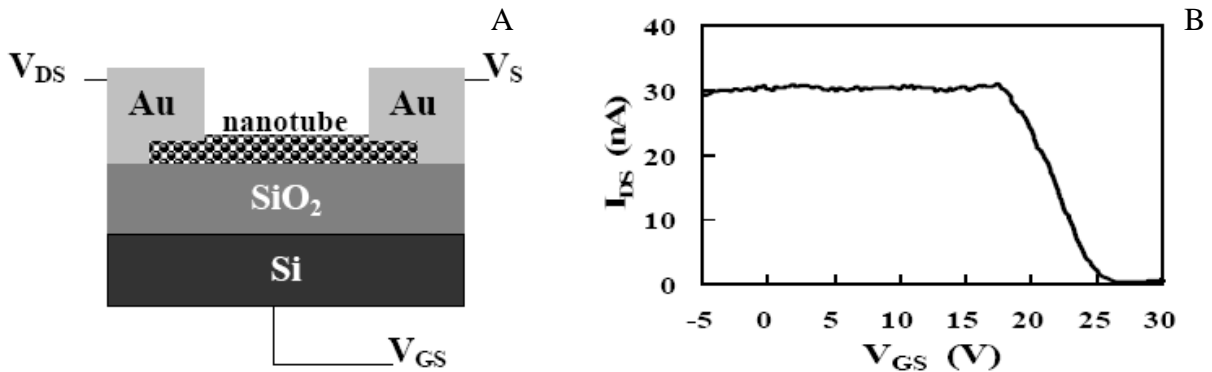


Figure 2-10. Electrical characterization of SWNT transistor. A) Cross-sectional schematic view of the SWNT transistor device. Back gate voltage is applied to the silicon substrate which is below the nanotube channel. B)  $I_{DS}$ - $V_{GS}$  curve of the SWNT transistor device and showing  $p$ -type behavior.

Table 2-1. Average height and density of catalyst nanoparticles formed after annealing and the average diameter and density of nanotubes grown for each Fe ion implantation condition.

Fe <sup>+</sup> ion implantation energy/dose (keV/cm <sup>-2</sup> )	Catalyst nanoparticle height (nm)	Catalyst nanoparticle density (μm <sup>-2</sup> )	Nanotube diameter (nm)	Nanotube density (μm <sup>-2</sup> )
60 / 10 <sup>14</sup>	2.2	< 1	-	-
60 / 10 <sup>15</sup>	2.0	170	2.2	6
60 / 10 <sup>16</sup>	15	4	2.2	1
25 / 10 <sup>15</sup>	2.7	800	2.8	7
130 / 10 <sup>15</sup>	21	6	-	-

Note: Between 60-400 catalyst nanoparticles and 130-200 nanotubes from several different samples were characterized to obtain the values listed for each implantation condition.

Table 2-2 Density of catalyst nanoparticles formed after growth for each Fe ion implantation condition.

Fe <sup>+</sup> ion implantation energy/dose (keV/cm <sup>-2</sup> )	Catalyst nanoparticle density (μm <sup>-2</sup> )	
	Before growth	After growth
25 / 10 <sup>15</sup>	800	525
60 / 10 <sup>15</sup>	170	400

CHAPTER 3  
MICROMACHINED SILICON TRANSMISSION ELECTRON MICROSCOPY GRIDS FOR  
DIRECT CHARACTERIZATION OF AS-GROWN NANOTUBES AND NANOWIRES

**Introduction**

Structural characterization of carbon nanotubes is typically performed by atomic force microscopy (AFM), scanning electron microscopy (SEM), micro-Raman spectroscopy, and transmission electron microscopy (TEM). AFM and SEM can only image the outer wall of a nanotube lying on a substrate. As a result, they cannot determine whether a carbon nanotube is single-walled or multi-walled, or give information about the number of walls of a multi-walled carbon nanotube (MWNT). Furthermore, there has been recent interest in nanotube “peapods,” which are single-walled carbon nanotubes filled with C<sub>60</sub> [132, 133].

Structural characterization of peapods is not possible with AFM and SEM, since they are incapable of determining whether a nanotube is filled or not [132]. High resolution TEM (HRTEM), on the other hand, is ideal for such nanostructure characterization. However, TEM requires very thin samples, which are electron transparent. The best images are obtained if the nanotubes are suspended freely over a gap. Therefore, for TEM analysis, nanotubes are typically sonicated off the substrate in a solvent (such as methanol, N,N-dimethylformamide (DMF), or 1,2-dichloroethane) and a few drops of the resulting suspension is deposited on commercially available holey-carbon TEM grids [12, 134]. This procedure has two potential problems: It can damage the nanotubes or alter their structural properties, and it does not work efficiently and reliably if the nanotube density is too low. This becomes a problem particularly for single-walled carbon nanotubes grown by chemical vapor deposition (CVD) at high temperatures on bulk substrates, such as SiO<sub>2</sub>/Si. Typically, the density of such nanotubes, used mainly for nanoelectronic device applications [25, 26], is very low. As a result, characterization and optimization of CVD growth conditions becomes a tedious task.

The ability to do TEM directly on as-grown nanotubes lying on silicon substrates would solve these problems. For this purpose, in this chapter, we fabricate micromachined Si TEM grids with narrow open slits on them, and demonstrate that they can be used for direct TEM, as well as AFM, SEM, and Raman characterization of as-grown nanotubes. The application of these grids is not limited to nanotubes, and can easily be extended to a wide range of nanomaterials, such as peapods, nanowires, nanofibers, and nanoribbons. Furthermore, these substrates are compatible with further microfabrication processes, such as lithography and thin film deposition. As a result, these micromachined Si substrates provide a low cost, mass producible, efficient, and reliable platform for direct structural characterization of as-grown nanotubes, nanowires, and other nanomaterials.

In recent work, nanotube-based nanoelectronic devices compatible with TEM characterization have been presented. For example, devices attached to metal electrodes after cleaving and etching a Si wafer [135] have been fabricated. In addition, devices have been suspended over windows etched in self-supporting silicon nitride membranes by e-beam lithography [132] or by a focused ion beam (FIB) [136, 137], or over windows etched in a silicon-on-insulator (SOI) wafer [138]. The micromachined Si TEM grids fabricated in this chapter offer a simpler, faster, and more efficient method for nanomaterials characterization.

### **Design of the TEM Grids**

In our experimental design, each Si TEM grid occupies an area of 2 mm by 2.6 mm on a ~500  $\mu\text{m}$  thick Si substrate, and the open slits are located in the center 1 mm by 1 mm windows where the Si substrate is thinned down to a membrane of approximately 15  $\mu\text{m}$ , as shown in Figure 3-1B. The size of the grid was chosen such that it fits into a standard TEM sample holder, as shown in Figure 3-1A. Each TEM grid contains 1440 slits with widths of 1.5, 2.5, 3.5

or 4.5  $\mu\text{m}$  and lengths of 50  $\mu\text{m}$  [see Figure 3-1C and D]. On a 4 inch silicon wafer, 743 such Si TEM grids are fabricated. As a result, taking advantage of standard silicon microfabrication, these grids can be easily mass produced at a low cost in a massively parallel fashion.

### **Microfabrication of the TEM Grids**

To fabricate the TEM grids, a 350 nm oxide was first thermally grown on both the front and the back side of a  $\sim 500$   $\mu\text{m}$  thick 4-inch (100) Si wafer, as shown in Figure 3-2A. Following the oxidation, a 1.6  $\mu\text{m}$  thick Shipley SPR 3612 photoresist was spun on both the back and front side of the wafer. Photolithography was then performed on the back side. After exposure and development, 1 mm by 1 mm windows were etched on the back side oxide using a buffered oxide etch (BOE) solution until the windows were hydrophobic [see Figure 3-2B]. After stripping the photoresist, 1 mm by 1 mm windows were etched from the back side Si using a 25% tetramethylammonium hydroxide (TMAH) solution in  $\text{H}_2\text{O}$  in a beaker at  $95^\circ\text{C}$  until approximately 15  $\mu\text{m}$  thick Si membranes remained. The etch rate of the TMAH solution is approximately 60  $\mu\text{m}/\text{hr}$ , and the etch end point was determined by periodic visual inspection [Figure 3-2C]. After the TMAH etch, top side lithography was performed aligned to the back side membranes using a 3  $\mu\text{m}$  thick Shipley SPR 220-3 photoresist. After exposure and development, slits of width ranging from 1.5 to 4.5  $\mu\text{m}$  and lengths of 50  $\mu\text{m}$  were dry etched on the top side oxide using an Applied Materials P5000 magnetically-enhanced reactive ion etcher (MERIE) with a 35 sccm  $\text{CHF}_3$ , 15 sccm  $\text{CF}_4$ , and 100 sccm Ar chemistry at 200 mTorr pressure, 420 W rf power, and 60 Gauss magnetic field [Figure 3-2D]. Following the oxide etch, slits of the same dimension were dry etched in the silicon membranes from the top using an STS Multiplex Inductively Coupled Plasma (ICP) Deep Reactive Ion Etcher (RIE) until punchthrough. After resist strip, the wafers were then coated with more photoresist to protect the surface and

diced into 2 mm by 2.6 mm grids using a wafersaw. The final cross-sectional structure is shown in Figure 3-2E.

### **Nanotube Growth on the TEM Grids**

After the TEM grids were fabricated, nanotubes were deposited on them using three different methods, to illustrate the versatility of these grids for different applications. In the first case, commercial SWNT powder purchased from Iljin Nanotech Co. Ltd. (Seoul, Korea) was dispersed in DMF and spin coated on these TEM grids. In the second case, SWNTs were grown by CVD using a 20  $\mu\text{g/mL}$  solution of iron(III) nitrate nonahydrate in 2-propanol as catalyst [24]. The grids were then placed in a 1-inch quartz tube furnace and grown at 940°C under 1,000 sccm  $\text{CH}_4$ , 20 sccm  $\text{C}_2\text{H}_4$ , and 500 sccm  $\text{H}_2$  flow for 10 minutes. In the third case, the Si TEM grids were ion implanted with  $\text{Fe}^+$  at an energy of 60 keV and a dose of  $10^{15} \text{ cm}^{-2}$ . The as-implanted grids were again placed in a 1-inch quartz tube furnace and heated up to 900°C under 300 sccm Ar and 200 sccm  $\text{H}_2$  flow, which lasted 11 min. When the temperature reached 900°C, the grids were annealed under the same argon and hydrogen flow rates for 2 min. As demonstrated in Chapter 2, this annealing step forms ~2 nm average size catalyst nanoparticles on the  $\text{SiO}_2$  surface, and these nanoparticles later act as catalyst for SWNT growth [139-141]. After annealing, nanotubes were grown at the same temperature, without removing the ion implanted TEM grids from the tube furnace, under 200 sccm  $\text{CH}_4$  and 200 sccm  $\text{H}_2$  flow for 10 min.

### **Characterization of Nanotubes Grown on the TEM Grids**

SWNTs obtained were characterized by a Digital Instruments Nanoscope III Atomic Force Microscope (AFM) operated in the tapping mode, a JEOL 2010F high resolution transmission electron microscope (HRTEM) operating at 100 kV, a JEOL JSM-6335F field emission gun

scanning electron microscope (FEG-SEM) operating at 15 kV, and a Renishaw Raman spectroscopy system.

Figure 3-3A, B and C, and D and F show HRTEM images of SWNTs deposited from the commercial powder, grown by CVD using the solution-based catalyst, and grown by CVD using the ion implanted catalyst, respectively. All images were taken using the micromachined Si TEM grids. Note that very high quality images of single-walled carbon nanotubes of a few nm diameter are very easily obtained using these grids. Furthermore, since there are many slits on the TEM grid, and all slits have multiple nanotubes suspended across them, these micromachined grids reduce the TEM characterization time significantly.

Figure 3-4A and B show SEM images of nanotubes freely suspended across the narrow slits of the micromachined TEM grids. These nanotubes were grown by CVD using the ion implanted catalyst, and the images were taken from the same sample that was used for the TEM images of Figure 3-3D, E, and F. Furthermore, Figure 3-4C and D show AFM images of SWNTs on the TEM grid samples CVD-grown from the ion implanted catalyst and the solution-based catalyst, respectively. AFM imaging was performed on the areas of the grids which do not have the slits. The grids are strong enough to support AFM imaging. These SEM and AFM results clearly show that TEM, AFM, and SEM characterization can be performed directly on the *same* as-grown sample. This is not possible with commercial TEM grids.

We have also characterized the SWNTs grown from the ion implanted catalyst on these grids by micro-Raman spectroscopy. The Raman spectra were obtained by a Kr ion laser with an excitation wavelength of 647.1 nm and a spot size of about 1  $\mu\text{m}$ . In order to increase the signal to noise ratio, the Raman spectra were accumulated many times over the same SWNT. Figure 3-5 shows micro-Raman spectra of SWNTs suspended freely over the slits on the TEM

grid. Characteristic multi-peak features around  $1580\text{ cm}^{-1}$  (called the tangential mode or the G band) are observed [128, 129], as shown in Figure 3-5A. Figure 3-5B shows the radial breathing mode (RBM) spectra characteristic of SWNTs obtained from the same nanotube. The RBM peak occurring at  $189\text{ cm}^{-1}$  corresponds to a SWNT diameter of 1.31 nm [128, 129]. The peak at  $310\text{ cm}^{-1}$  comes from the Si substrate. Since nanotubes were freely suspended, the background signal from the substrate was minimized, and the signal-to-noise ratio was significantly improved. As a result, in addition to TEM, the micromachined Si grids also improve the characterization of carbon nanotubes by Raman spectroscopy.

### **Conclusions**

In conclusion, we have fabricated micromachined Si TEM grids with narrow open slits on them, and demonstrated that they can be used for direct TEM, as well as AFM, SEM, and Raman characterization of as-grown nanotubes. As a result, these micromachined TEM grids offer fast, easy, and reliable structural characterization of as-grown carbon nanotubes. Although we present data here only on SWNT characterization, the application of these grids is not limited to nanotubes, and can be used for characterizing a wide range of nanomaterials, such as peapods, nanowires, nanofibers, and nanoribbons. Furthermore, depending on the application, smaller or larger slit widths can be designed, or other dielectric materials, besides oxide can be used. As a result, these substrates provide a low cost, mass producible, and efficient, reliable, versatile platform for direct TEM, AFM, SEM, and Raman analysis of as-grown nanomaterials, eliminating the need for any post-processing after CVD growth.

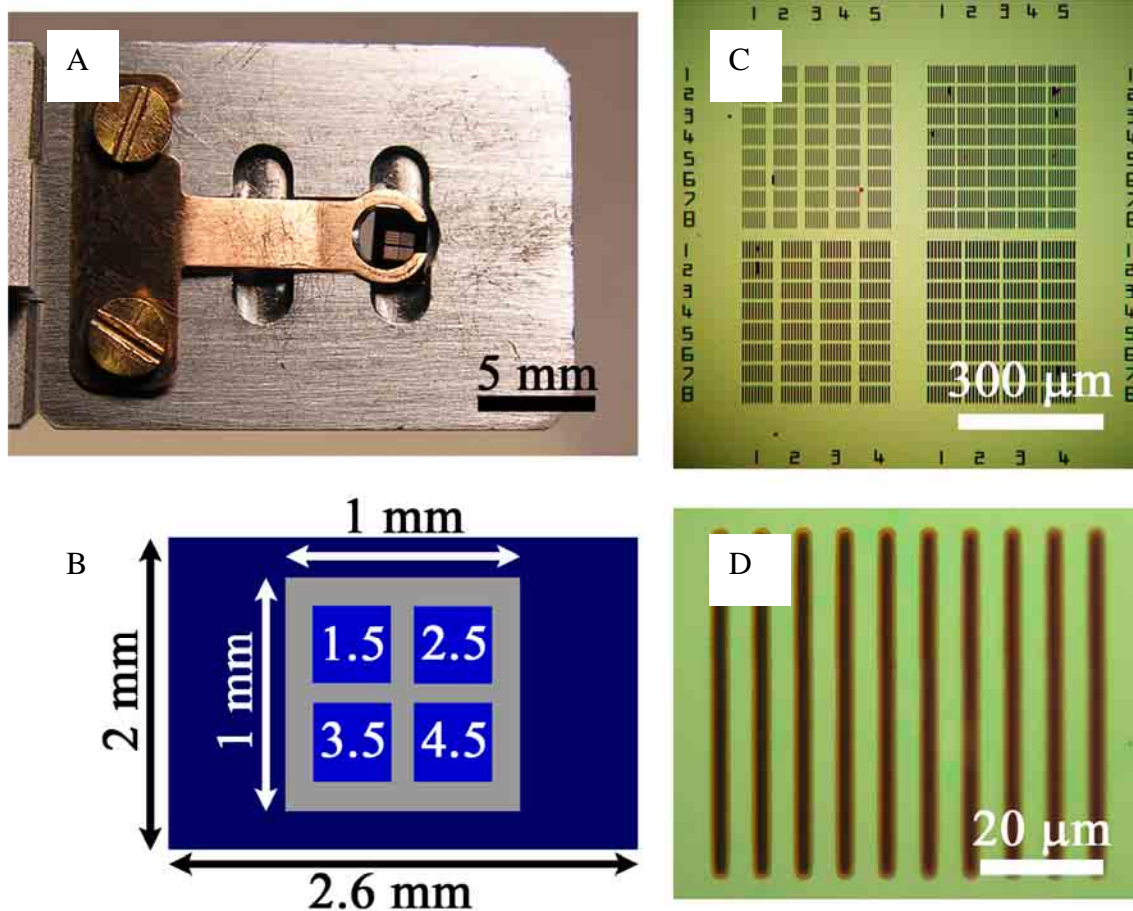


Figure 3-1. Images of fabricated Si TEM grid. A) Digital photograph of TEM sample holder with micromachined Si TEM grid clamped in the groove on the right. The size of the grid was designed such that it fits easily into a standard TEM sample holder. B) Top view schematic of the micromachined Si TEM grid. It occupies a 2 mm by 2.6 mm area with a thickness of  $\sim 500 \mu\text{m}$ . The open slits are located in the center 1 mm by 1 mm area, where the Si substrate is thinned down to  $\sim 15 \mu\text{m}$  to form a membrane. This center area is divided into 4 quadrants, each labeled by a number (1.5, 2.5, 3.5 or 4.5) corresponding to the width of the narrow open slits in that quadrant in units of  $\mu\text{m}$ . C) Optical microscope image of the center area of the TEM grid in B, showing the 4 quadrants with the narrow open slits. Each TEM grid contains 1440 slits, and a four inch wafer contains 743 such grids. D) Close up optical microscope image of an array of slits.

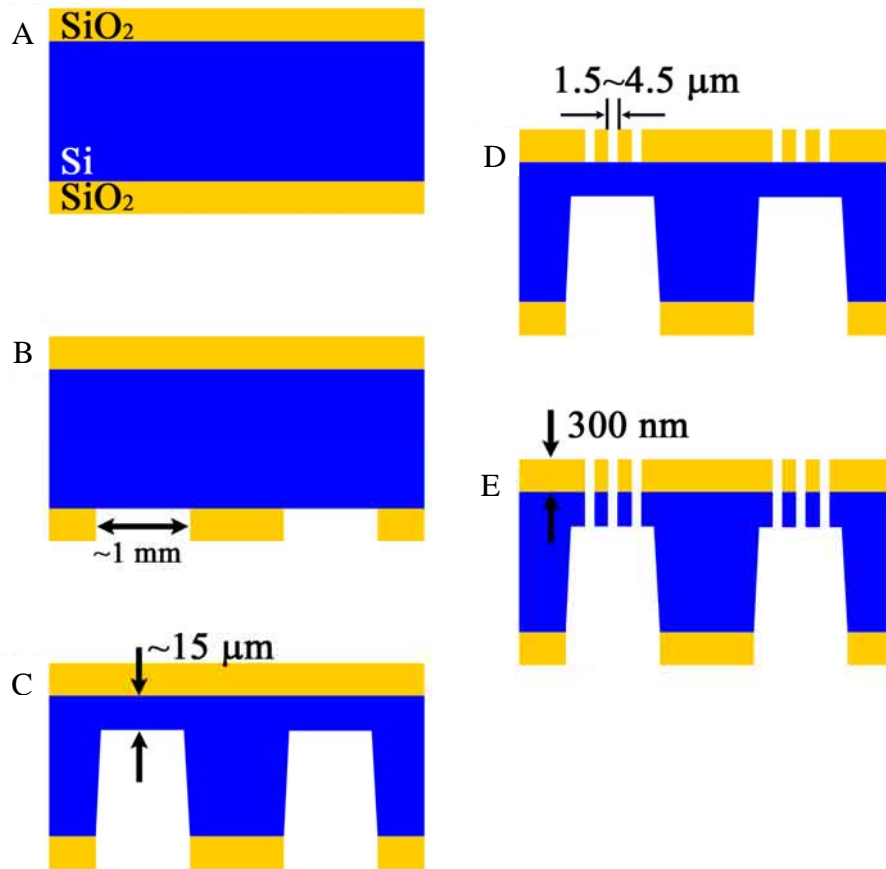


Figure 3-2. Cross-sectional schematic of process flow for the micromachined Si TEM grids. Some intermediate steps are not shown. Figures are not to scale. A) Thermally grown 350 nm oxide on both the front and the back side of a (100) Si wafer. B) 1 mm by 1 mm windows etched on the back side oxide using a buffered oxide etch (BOE) solution. C) 1 mm by 1 mm windows etched from the back side Si using a TMAH solution until ~15 μm thick Si membranes remain. TMAH etches the {100} planes faster than the {111} planes. As a result, the sidewalls formed during the etch are not vertical as sketched in the figure, but sloped. D) Narrow open slits of width ranging from 1.5 to 4.5 μm dry etched on the top side oxide. E) Open slits of the same dimension dry etched in silicon from the top using a deep silicon etcher.

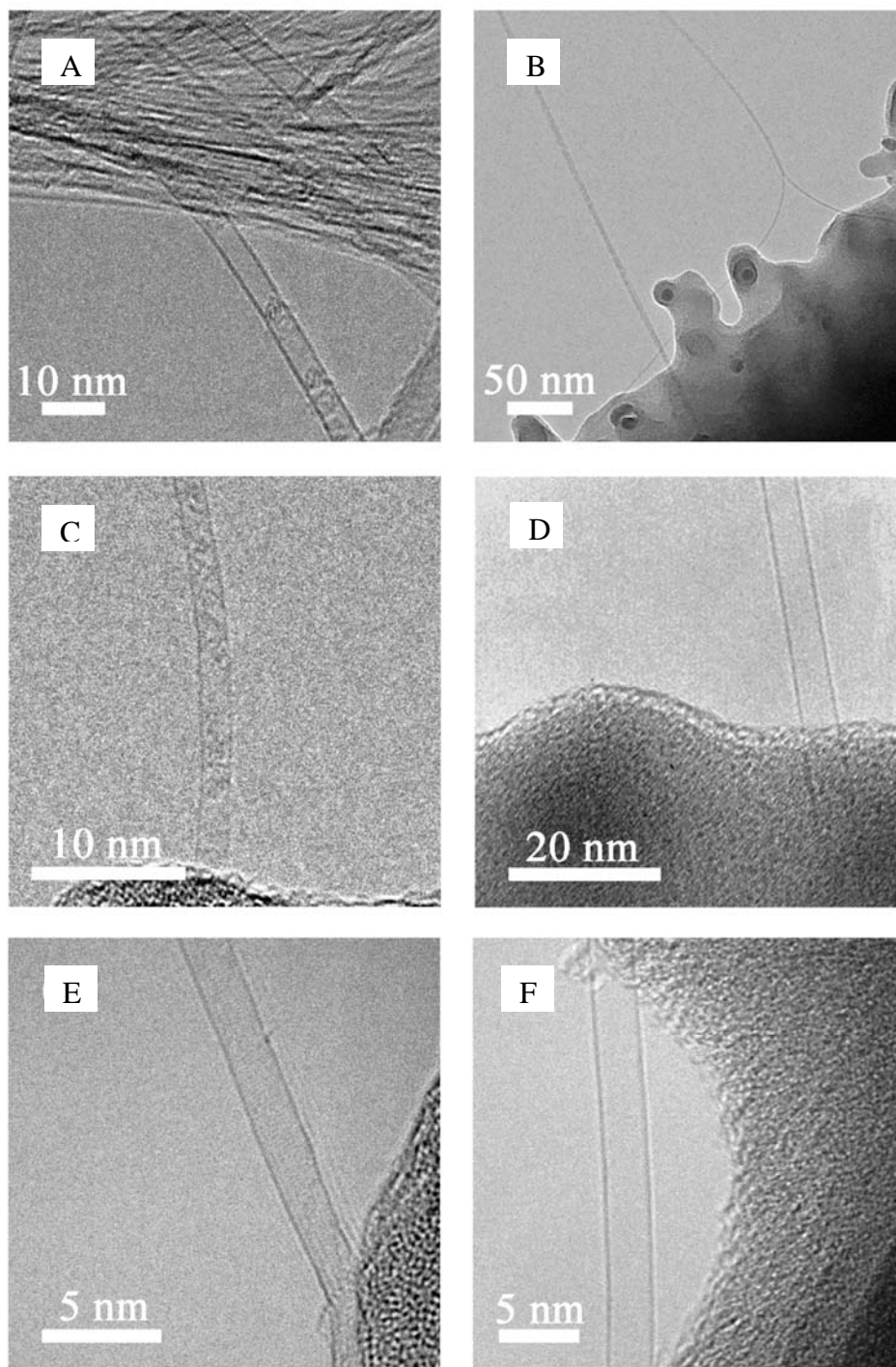


Figure 3-3. HRTEM images of SWNTs taken using the micromachined Si TEM grids. A) SWNTs deposited from commercial powder B and C) SWNTs grown by CVD using the solution-based catalyst, and D-F) SWNTs grown by CVD using the ion implanted catalyst. The details of the catalyst and growth conditions are given in the text. Since there are many slits on the TEM grid, and all slits have multiple nanotubes suspended across them, these micromachined grids reduce the TEM characterization time significantly.

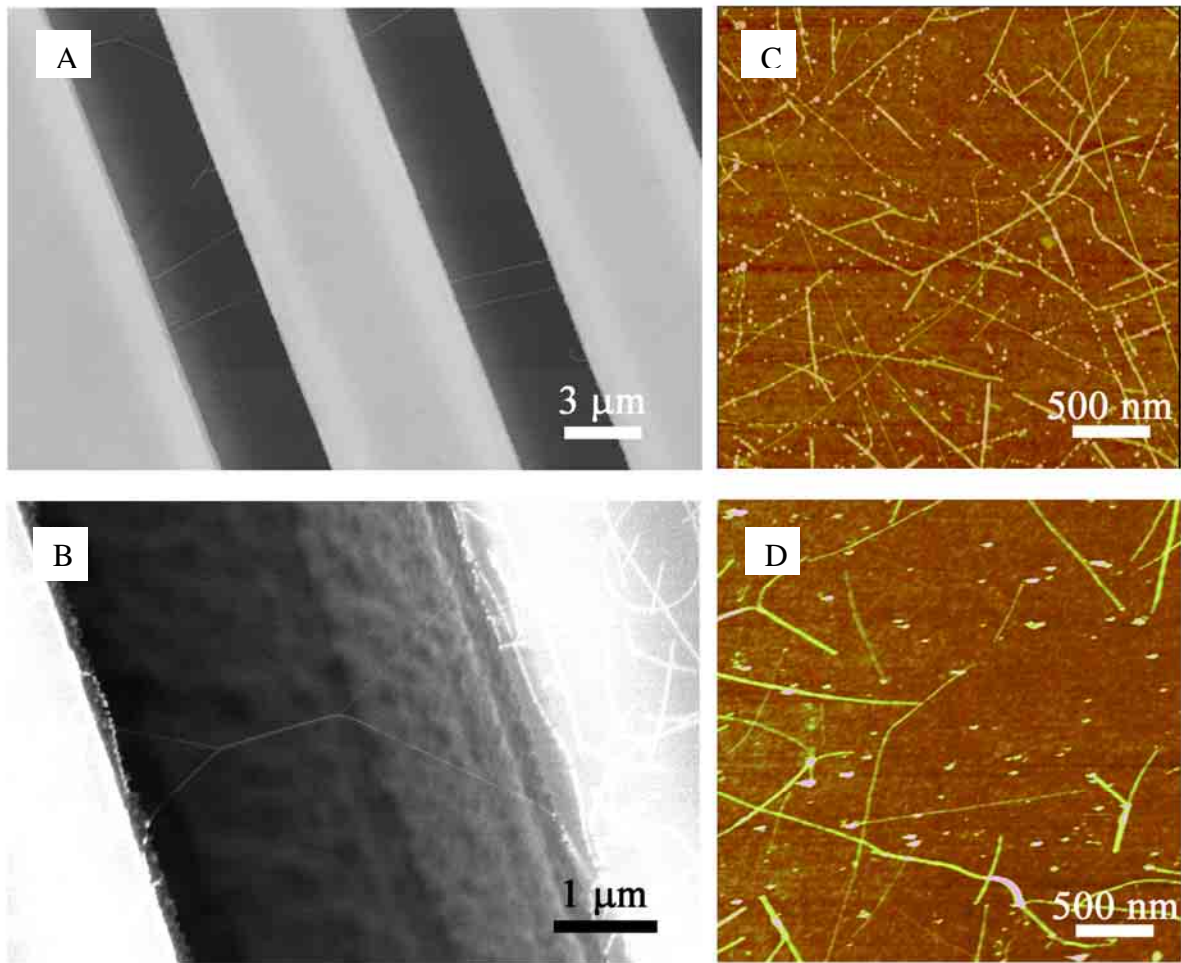


Figure 3-4. Images of SWNTs grown on micromachined Si TEM grid. A and B) SEM images of nanotubes suspended across the slits of the micromachined TEM grids. These nanotubes were grown by CVD using the ion implanted catalyst, and the images were from the same sample as the TEM images of Figure 3-3 D-F). Nanotubes suspended across the slits is clearly observed. C and D) show from ion implanted catalyst and solution-based catalyst, respectively. AFM imaging was AFM images of SWNTs on the solid parts of the TEM grid samples for CVD grown nanotubes performed on the solid areas of the grid which do not have the slits.

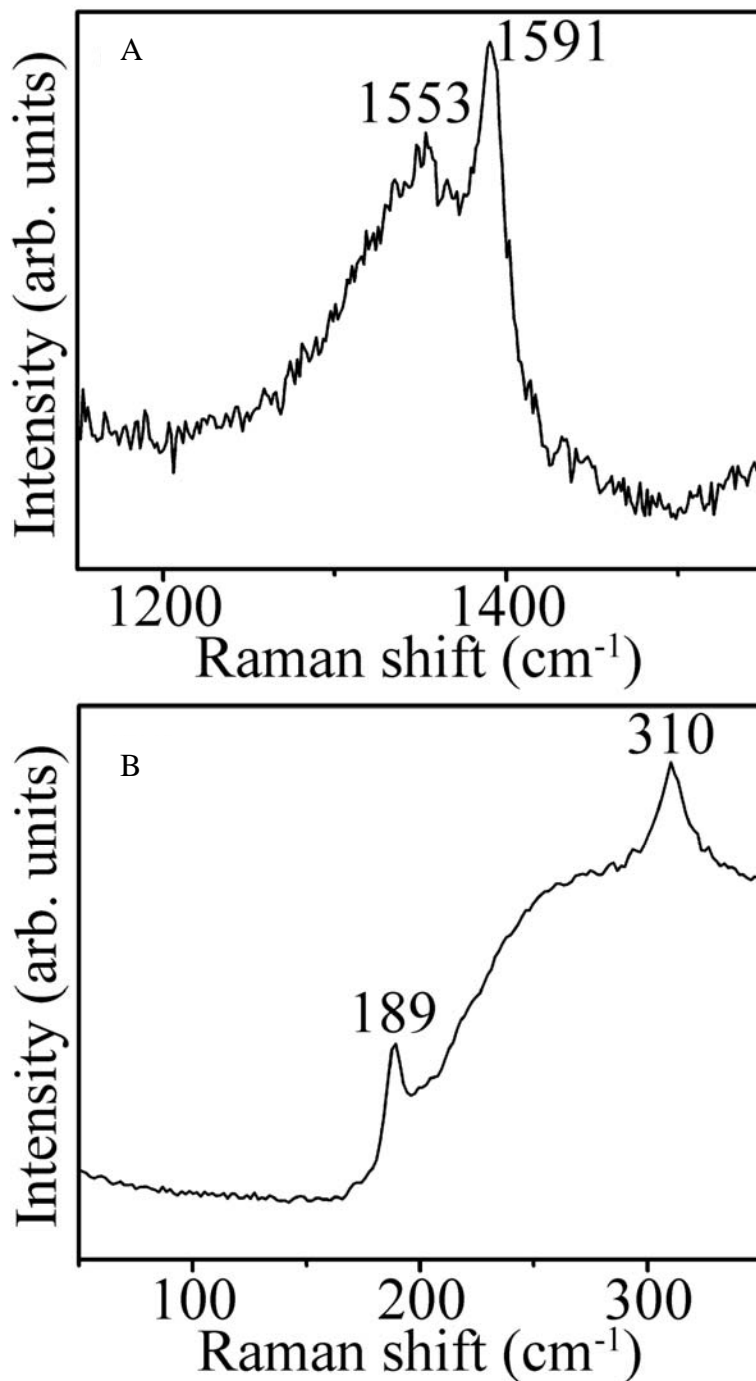


Figure 3-5. Micro-Raman spectra of SWNTs grown from the ion implanted catalyst, suspended freely over the slits on the TEM grid. A) Tangential mode (G band) spectra of nanotubes showing multi-peaks characteristic of a metallic SWNT [128, 129] at 1553 and 1591 cm<sup>-1</sup>. B) Radial Breathing Mode (RBM) Raman spectra with a peak at 189 cm<sup>-1</sup>, which corresponds to a SWNT diameter of 1.31 nm [128, 129]. The signal-to-noise ratio was significantly reduced by performing Raman on suspended nanotubes.

## CHAPTER 4 SILICON OXIDE NANOWIRE GROWTH FROM IRON ION IMPLANTED SiO<sub>2</sub> SUBSTRATES

### **Introduction**

As mentioned in the introduction, one-dimensional (1D) nanostructures, such as nanotubes and nanowires, have attracted significant research attention in recent years due to their unique structural and electronic properties. SiO<sub>2</sub> is a material which is of great technological importance in silicon VLSI technology. Nanowires of silicon oxide have a great potential in applications such as low dimensional waveguides, scanning near-field optical microscopy, blue light emitters, nanoscale optical devices and sensors, sacrificial templates, and biosensors [142-144].

Several methods have been used to grow silicon oxide nanowires, such as laser ablation [143], thermal evaporation [145], and chemical vapor deposition (CVD) [146]. In most of these cases, a growth model based on the vapor-liquid-solid (VLS) growth mechanism [147] has been used to explain the observed results. An essential component of the VLS growth process is the nanoscale catalyst particles required to nucleate the growth of nanowires. For example, several recent studies have demonstrated the growth of silicon oxide nanowires from a variety of different catalyst nanoparticles, including sputtered or evaporated metal thin films (such as Pt [142, 148], Au [149], Pd [149], and Ni [150]), molten Ga [146, 151-153], and Sn powder [154, 155]. In some of these studies, Si was supplied as a powder [143, 145] or in gaseous phase as silane (SiH<sub>4</sub>) [146]. In a number of other studies, on the other hand, the catalyst material was deposited directly on the Si substrate [142, 148-155]. In these studies, the Si reactant is supplied by the solid Si substrate during growth, and the oxygen is supplied in gaseous form either intentionally by introducing oxygen or air into the chamber or unintentionally as a residual gas due to leakage or impurities in the carrier gases used.

In Chapter 2, we have demonstrated that single-walled carbon nanotubes (SWNTs) can be produced by the process of iron (Fe) ion implantation into thermally grown SiO<sub>2</sub> layers, subsequent annealing, and CVD growth [139]. In this chapter, we experimentally demonstrate a similar approach for silicon oxide nanowire growth by implanting Fe<sup>+</sup> ions directly into thermally grown SiO<sub>2</sub> layers on Si wafers to nucleate silicon oxide nanowires during subsequent annealing in argon and hydrogen. In contrast to the previous work [144], both reactants (Si and O) come from the SiO<sub>2</sub> substrate, which acts as a solid source. As a result, this work integrates and simultaneously demonstrates three important results: (1) The use of ion implantation as a versatile method to create catalyst nanoparticles for silicon oxide nanowire growth, (2) The use of Fe, a commonly used catalyst for single-walled carbon nanotube growth, as an efficient catalyst also for silicon oxide nanowire growth, and (3) The use of SiO<sub>2</sub> layers as a solid source in a solid-liquid-solid (SLS) growth mechanism to achieve a Si:O ratio close to 1:2. Furthermore, we study the effect of temperature, H<sub>2</sub> gas flow, and growth time on the silicon oxide nanowire growth and explain the results in terms of a simple physical growth model based on the SLS mechanism.

### **Experimental Method**

In our experiment, 500 nm thick SiO<sub>2</sub> layers were first thermally grown on silicon (100) substrates. Fe<sup>+</sup> ions were ion implanted into the SiO<sub>2</sub> layers at energy of 60 keV with a dose of 10<sup>15</sup> cm<sup>-2</sup>, as illustrated in Figure 4-1A. The implantation depth profile calculated by SRIM simulations [120] is shown in Figure 4-1B, where the projected range  $R_p$  is 50 nm, and the peak concentration  $C_p$  is  $\sim 1.5 \times 10^{18}$  cm<sup>-3</sup>. For the growth of silicon oxide nanowires, the as-implanted samples were placed in a one inch quartz tube furnace. The quartz tube was then purged at room temperature with 350 sccm flow rate of Ar and 200 sccm flow rate of H<sub>2</sub> for 15 min. After purging the tube, the temperature was increased to 1100°C and the samples were

annealed for 30 min under the same gas flow rates (350 sccm Ar and 200 sccm H<sub>2</sub>) to grow the silicon oxide nanowires. The system was then cooled down to room temperature under the same gas flow rates and the samples were taken out of the furnace and characterized.

The as-grown samples were characterized by a JEOL JSM-6335F field emission gun scanning electron microscope (SEM) operating at 10 kV, a JEOL 2010F high resolution transmission electron microscope (HRTEM) operating at 100 kV equipped with selected area electron diffraction (SAED) and energy dispersive X-ray spectroscopy (EDS) capability, and a Digital Instruments Nanoscope III Atomic Force Microscope (AFM) operated in the tapping mode. For the HRTEM characterization, the as-grown nanowires were dispersed in 2-propanol, the solution was sonicated, and a few drops of the resulting suspension was deposited on commercially available Cu TEM grids coated with a holey carbon film [156].

### **Results and Discussion**

Figure 4-2 shows SEM images of the as-grown silicon oxide nanowires at 1100°C under 350 sccm Ar and 200 sccm H<sub>2</sub> flow rates. Based on SEM observations, the density of nanowires is high and most nanowires are longer than 10 μm. Furthermore, based on analysis of SEM and TEM images, the diameter of the silicon oxide nanowires were found to be in the range between 10 and 40 nm. Figure 4-3A and B show TEM images of the as-grown silicon oxide nanowires. The inset of Figure 4-3B shows the SAED pattern of an individual silicon oxide nanowire. The high resolution TEM image [Figure 4-3B] and the SAED pattern confirm that the as-grown silicon oxide nanowires are amorphous. In addition, Figure 4-4 shows the EDS spectrum of a silicon oxide nanowire. The copper and carbon peaks in the spectrum come from the TEM grid [156] that the nanowires are deposited on. The only other visible peaks are oxygen and silicon, confirming that the as-grown nanowires are indeed silicon oxide. Furthermore, quantitative EDS analysis revealed that the atomic ratio of Si to O is 1:2.6,

implying that the as-grown nanowires are close to SiO<sub>2</sub> nanowires. The use of a thermally grown SiO<sub>2</sub> layer as the source material could have played an important role in getting close to a 1:2 ratio. Three other growth conditions were investigated in order to gain a further understanding of the effect of growth parameters on the ion implanted catalyst nanoparticle formation and nanowire growth. In the first case, the growth temperature was lowered to 1000°C, keeping all the other parameters the same.

Due to the dense growth at 1100°C (Figure 4-2), however, it is not possible to obtain exact information about the catalyst nanoparticle density and height for that high temperature growth condition for a direct comparison. Secondly, as it will be mentioned later, the proposed solid-liquid-solid (SLS) growth model involves the formation of a liquid alloy droplet containing Fe, Si, and O, which then nucleates the silicon oxide nanowire. Figure 4-5A shows the AFM image of the sample after growth at 1000°C. It is clear from the AFM image that no nanowires have been grown at this lower temperature. The average height of the catalyst nanoparticles on the surface of the substrate extracted from cross-sectional AFM analysis is 8.2 nm. The absence of nanowires at 1000°C could be explained by two factors: First, the diffusion rate of implanted Fe atoms towards the surface depends exponentially on temperature. As a result, the density and height of catalyst nanoparticles formed on the SiO<sub>2</sub> surface by the out-diffusion of Fe atoms could be too small to nucleate nanowire growth at lower temperatures. If the temperature drops below the melting point of this alloy, nanowires cannot be nucleated. As a result of these two reasons, temperature is found to be a critical factor for determining nanowire growth. This observation is in agreement with previous work, which also found that high temperatures were required for the growth of silicon oxide nanowires [142, 144]. In the second growth condition investigated, the growth temperature was kept at 1100°C, but no H<sub>2</sub> gas was supplied during the

growth process, keeping all the other parameters the same. Figure 4-5B shows the AFM image of the sample surface after growth without any H<sub>2</sub>. As clearly seen in the figure, no nanowires have been grown in the absence of H<sub>2</sub> flow. The average catalyst nanoparticle height measured by cross-sectional AFM analysis is about 1 nm in this case. It has been well demonstrated that the diameter of nanowires is correlated with the size of the catalyst nanoparticles [157]. In this case, it is clear from the AFM image that the catalyst nanoparticle size (~ 1nm) is too small to nucleate silicon oxide nanowires, which typically have diameters of tens of nanometers. Hydrogen is known to enhance the diffusion of impurities in SiO<sub>2</sub> [158, 159]. The observed increase in the catalyst nanoparticle size when H<sub>2</sub> is flown during the growth can be explained by a similar enhancement of Fe diffusion in SiO<sub>2</sub> in H<sub>2</sub> ambient. These observations confirm that the presence of H<sub>2</sub> gas flow is also a critical factor for the catalyst nanoparticle formation.

In the third growth condition, the growth time was reduced to 10 min at 1100°C (instead of 30 min), keeping all the other parameters the same. Figure 4-5C shows the AFM image of the sample surface after growth for 10 min. It is clear from the figure that no nanowires have been grown when the growth time is short. The average catalyst nanoparticle height measured by cross-sectional AFM analysis is 6.2 nm in this case, which (similar to the previous cases) is too small to nucleate silicon oxide nanowires. As a result, growth time is also an important parameter, since the catalyst nanoparticle size increases as a function of time due to the continuous out-diffusion of implanted Fe atoms to the sample surface.

We have also performed growth on a control SiO<sub>2</sub> substrate with no Fe ion implantation. The growth temperature was 1100°C and all the other growth parameters were the same as before. No nanowire growth took place in the absence of Fe ion implantation. As a result,

this control experiment provided direct evidence that the presence of Fe nanoparticles is essential for nucleating the growth of silicon oxide nanowires.

The vapor-liquid-solid (VLS) growth mechanism [147] has been commonly used to explain the growth of nanowires from catalyst nanoparticles. In VLS growth, the precursor is initially provided in gas-phase and forms a liquid alloy with the catalyst nanoparticles. In contrast, in our silicon oxide nanowire growth process, silicon and oxygen are provided from the solid SiO<sub>2</sub> substrate, resulting in a solid-liquid-solid (SLS) growth mechanism. In analogy to the VLS case, the physical model for the SLS growth of silicon oxide nanowires can be proposed as follows: First, the as-implanted Fe atoms [Figure 4-6A] out-diffuse to form catalyst nanoparticles on the SiO<sub>2</sub> surface [Figure 4-6B]. The catalyst nanoparticles from which nanowire growth has not yet nucleated could also get larger by a surface diffusion and Ostwald ripening process. Liquid alloy droplets containing Fe, Si, and O form from these catalyst nanoparticles [Figure 4-6C]. When these liquid alloy droplets become supersaturated in silicon and oxygen, solid silicon oxide nanowires nucleate and precipitate out of these droplets [Figure 4-6D]. EDS characterization over the whole area of the nanowire TEM specimen showed no Fe peak and further investigation of the nanowires by SEM and TEM revealed no iron catalysts at the tip of the nanowires. These results indicate that the iron catalysts remain on the SiO<sub>2</sub> substrate during the growth of nanowires, which implies a base-growth mechanism as indicated in Figure 4-6D.

### **Conclusions**

In conclusion, we have experimentally demonstrated the growth of silicon oxide nanowires from Fe<sup>+</sup> ions implanted into thermally grown SiO<sub>2</sub> layers on Si. We explained the growth results in terms of a physical model based on the solid-liquid-solid (SLS) growth mechanism. We also showed that the nanowires are silicon oxide with a Si:O ratio of 1:2.6. Furthermore,

high temperature, hydrogen gas flow, and growth time were found to be critical parameters for silicon oxide nanowire growth. This work opens up the possibility of growing nanowires directly from solid substrates, controlling the origin of nanowires at the nanometer scale, and integrating them into nonplanar three-dimensional device structures with precise dose control. This method of nucleating nanowire growth is not limited to silicon oxide nanowires; it could also be generally applied to the growth of other types of nanowires for potential applications.

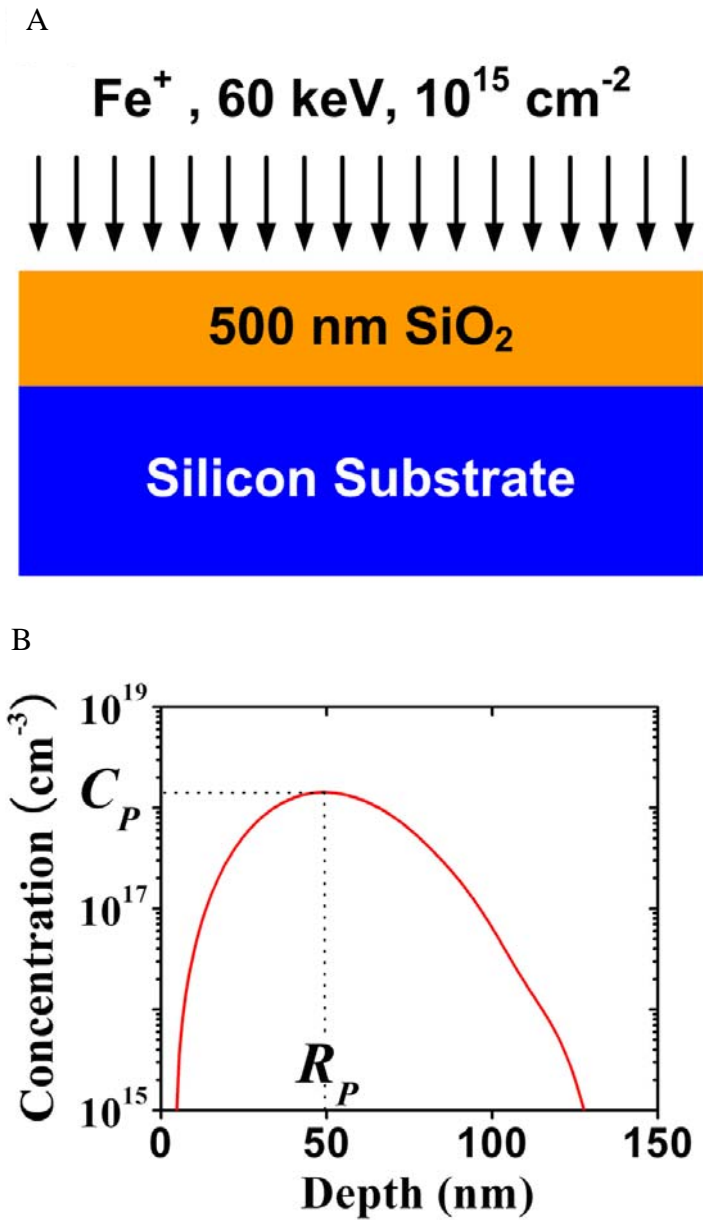


Figure 4-1. Conditions of ion implantation. A) Schematic of SiO<sub>2</sub>/Si substrate and Fe ion implantation condition used for catalyst nanoparticle formation for silicon oxide growth. B) Depth profile of Fe atoms ion-implanted into thermally grown SiO<sub>2</sub> at an energy of 60 keV and a dose of 10<sup>15</sup> cm<sup>-2</sup>, calculated by SRIM simulations, giving a projected range of  $R_p = 50$  nm and a peak concentration of  $C_p \sim 1.5 \times 10^{18}$  cm<sup>-3</sup>, as labeled.

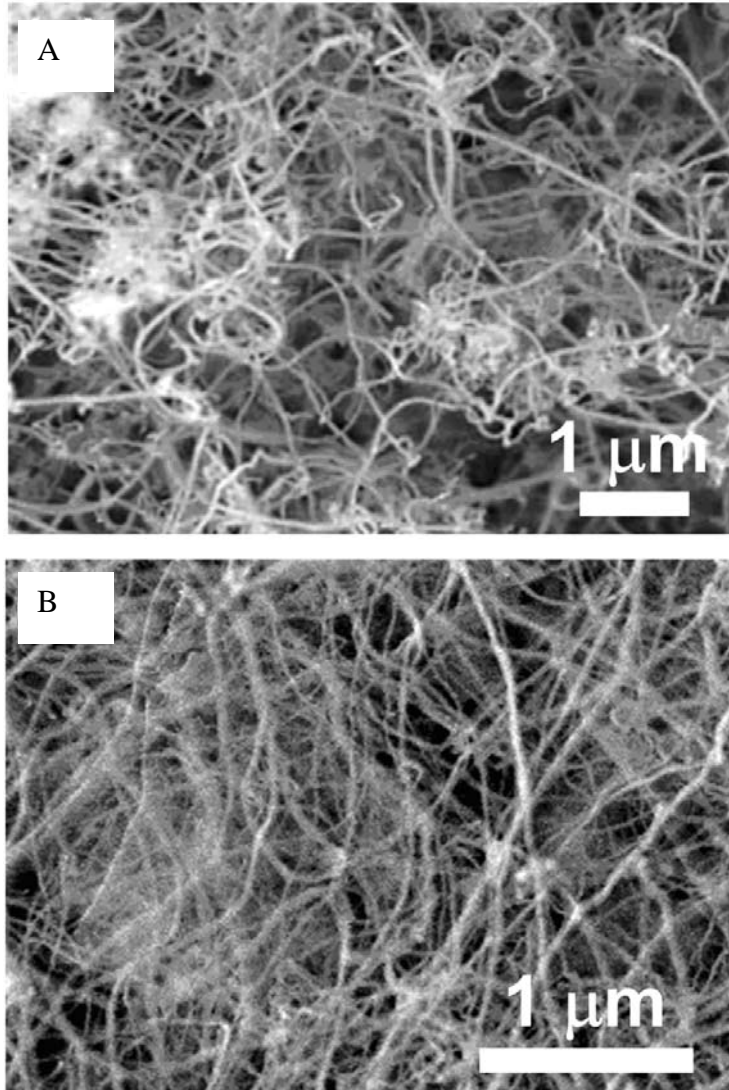


Figure 4-2. Scanning electron microscopy (SEM) images of silicon oxide nanowires grown from Fe catalyst ion implanted (60 keV energy and  $10^{15} \text{ cm}^{-2}$  dose) into thermally grown  $\text{SiO}_2$  layers. The diameters of the nanowires range between 10 and 40 nm.

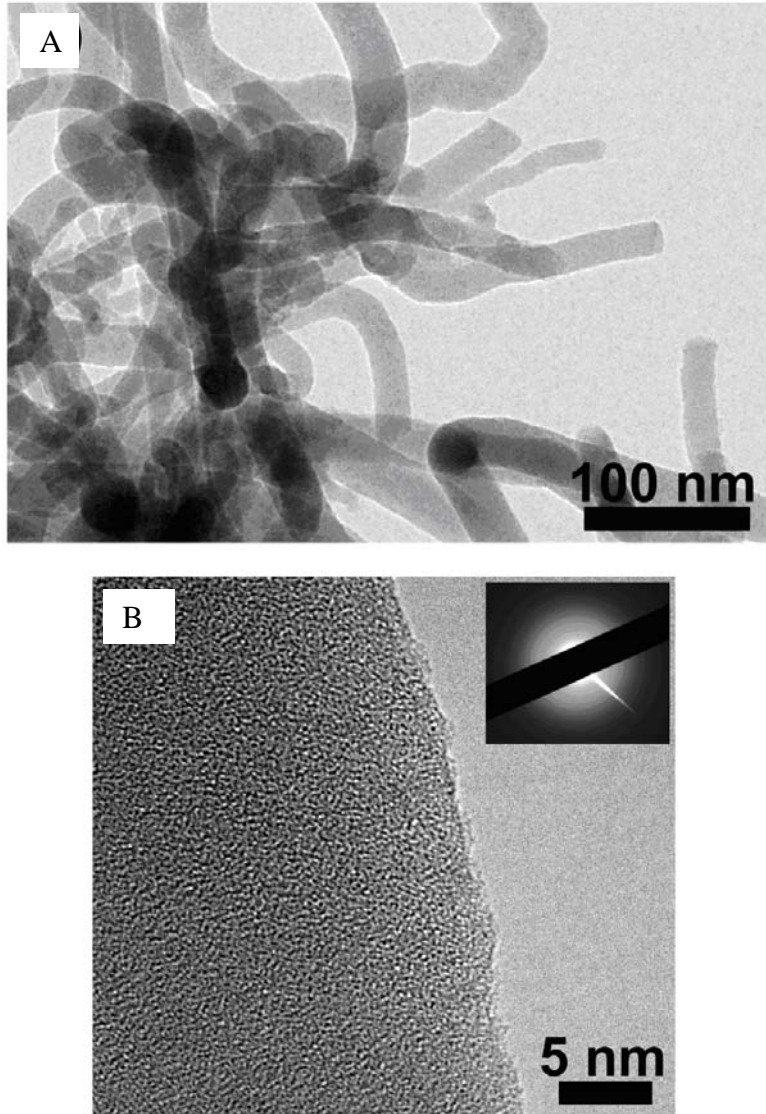


Figure 4-3. Images of silicon oxide nanowires. A) Low resolution and B) high resolution transmission electron microscopy (TEM) images of silicon oxide nanowires. The inset of B shows the selected area electron diffraction (SAED) of an individual nanowire. The high resolution TEM image and the SAED pattern confirm that the silicon oxide nanowires are amorphous.

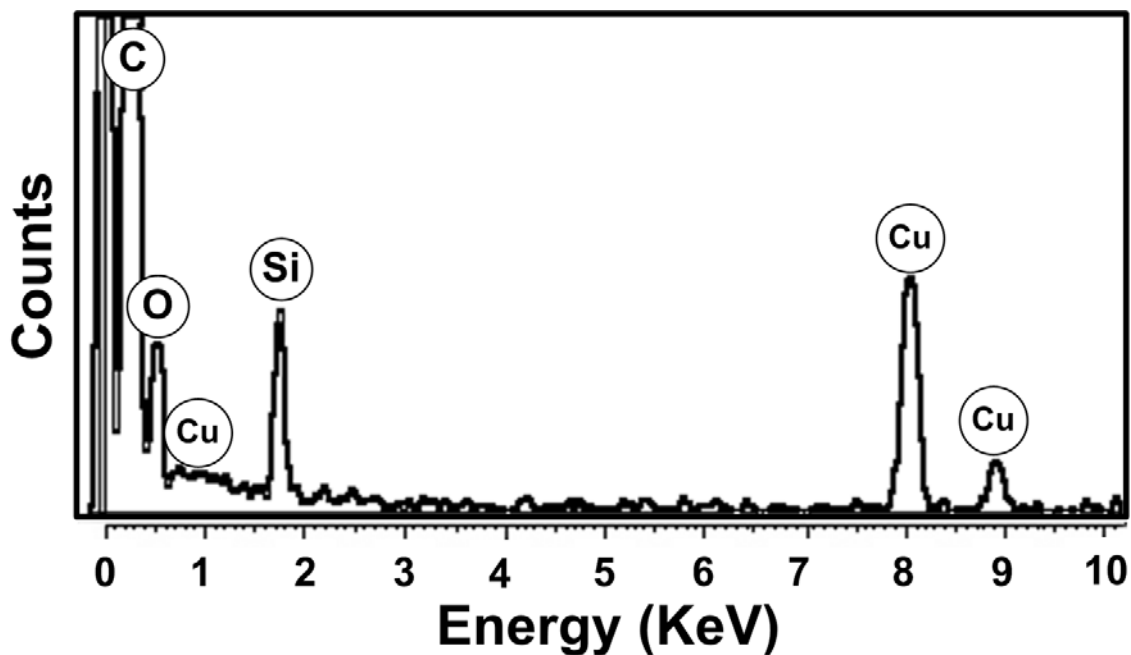


Figure 4-4. Energy dispersive X-ray spectroscopy (EDS) spectrum of an individual silicon oxide nanowire. The Cu and C peaks in the spectrum come from the TEM grid that the nanowires are deposited on. The only other visible peaks are Si and O, confirming that the as-grown nanowires are silicon oxide. Quantitative EDS analysis revealed that the Si:O atomic ratio is 1:2.6, implying that the nanowires are close to  $\text{SiO}_2$  nanowires.

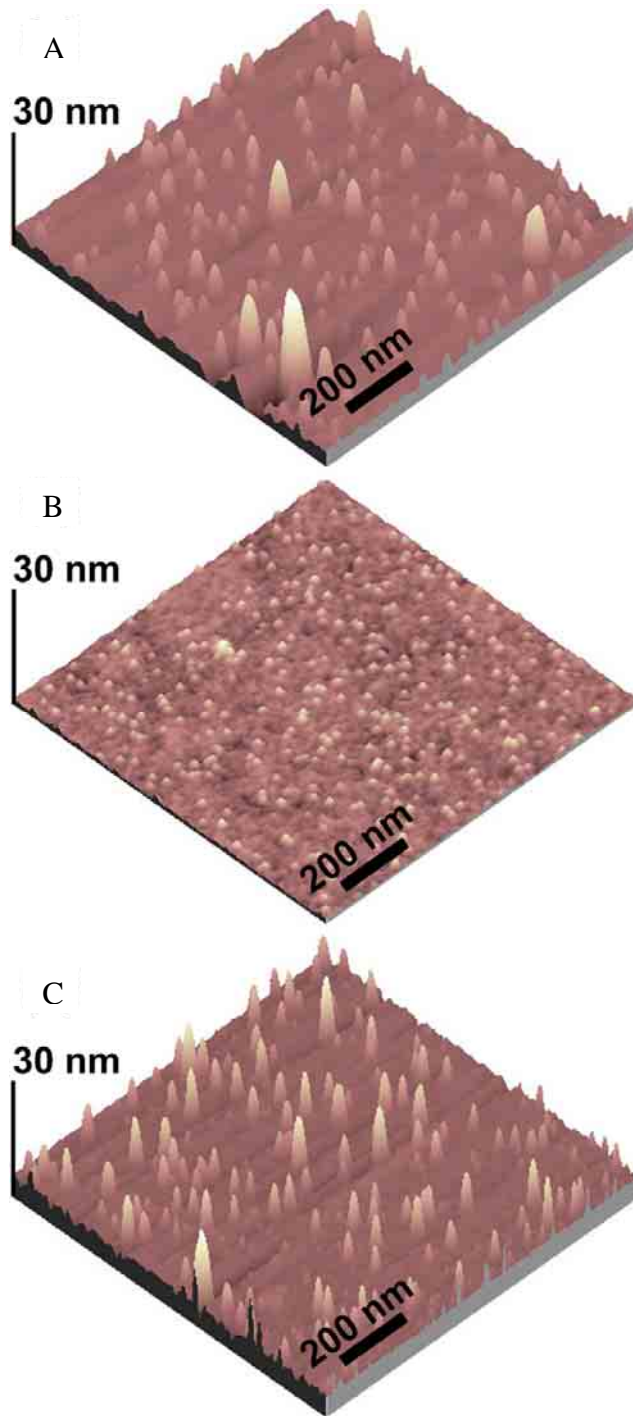


Figure 4-5. AFM images of the SiO<sub>2</sub> sample surface A) grown at 1000°C, B) grown at 1100°C, but with no H<sub>2</sub> gas supplied during the growth process, and C) grown at 1100°C, but for only 10 min, keeping all the other parameters the same as in Figure 4-2. No silicon oxide nanowire growth was observed in any of these cases.

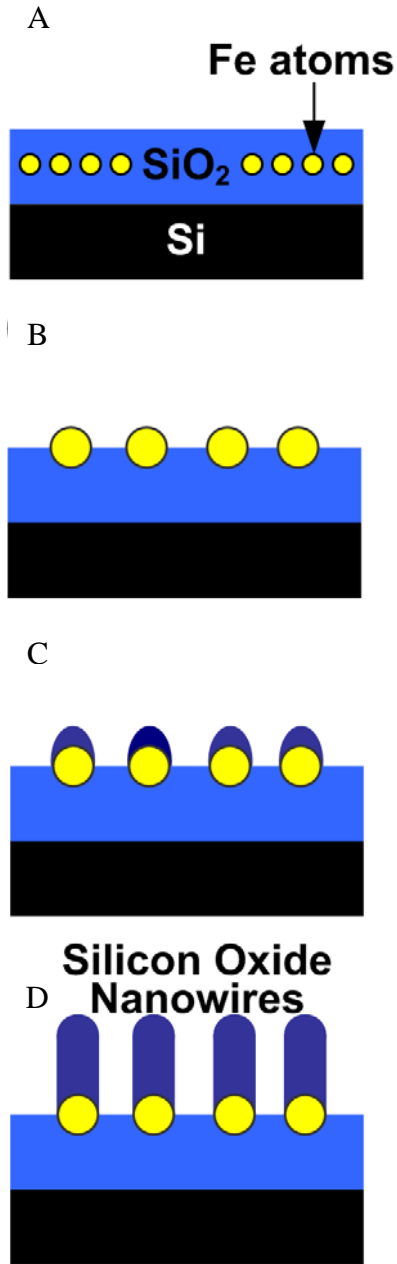


Figure 4-6. Schematic diagram of the proposed solid-liquid-solid (SLS) growth model of silicon oxide nanowires: A) First, Fe atoms are ion-implanted into the SiO<sub>2</sub> substrate. B) At high temperature, Fe atoms out-diffuse to form catalyst nanoparticles on the SiO<sub>2</sub> surface. C) Liquid alloy droplets containing Fe, Si, and O form on the SiO<sub>2</sub> surface. The source of the silicon and oxygen is the SiO<sub>2</sub> substrate. D) Silicon oxide nanowires nucleate and precipitate out of the liquid alloy droplets.

## CHAPTER 5 GAN NANOWIRE GROWTH FROM ION IMPLANTED IRON CATALYST

### Introduction

One-dimensional (1D) nanowires of GaN have been grown in recent years using a variety of techniques including laser ablation [102, 160], arc discharge [161], template-assisted growth [162], thermal evaporation [116], metal-organic chemical vapor deposition (MOCVD) [163], molecular beam epitaxy (MBE) [164], and chemical vapor deposition (CVD) [165-168].

For most of the synthesis using CVD, a growth model based on the vapor-liquid-solid (VLS) growth mechanism [147] has been used to explain the observed results. As explained in Chapter 4, an essential component of the VLS growth process is the nanoscale catalyst particles required to nucleate the growth of nanowires. For example, for GaN nanowire growth, nanoparticles of metals such as In [167], Ni [167, 169], Co [167], Au [170], or Fe [167, 171] have been used as catalyst. In particular, Fe has been shown to be a good catalyst for GaN nanowire growth since it dissolves both Ga and N and does not form a more stable compound than GaN [102, 171].

In this chapter, similar to SWNTs and SiO<sub>x</sub> nanowires, we experimentally demonstrate a simple and efficient approach for nucleating the growth of GaN nanowires by ion implantation of Fe<sup>+</sup> ions directly into thermally grown SiO<sub>2</sub> layers and subsequent annealing to form catalyst nanoparticles. This work experimentally shows that ion implantation can be used as a versatile method to create catalyst nanoparticles for wide bandgap semiconductor nanowire growth, as well. Furthermore, we systematically characterize the as-grown nanomaterials, discuss the effect of growth parameters on the nanostructures grown, and explain the growth results in terms of simple physical models based on the VLS growth mechanism.

## Experimental Method

For our experiment, a 500 nm thick SiO<sub>2</sub> layer was thermally grown on silicon (100) substrates. Fe<sup>+</sup> ions were implanted into these substrates at an energy of 60 keV with a dose of 10<sup>15</sup> or 10<sup>16</sup> cm<sup>-2</sup>. The implantation depth profile calculated by SRIM simulations [120] for the 10<sup>16</sup> cm<sup>-2</sup> dose is shown in Figure 5-1A, where the projected range  $R_p$  is 50 nm, and the peak concentration  $C_p$  is  $\sim 1.5 \times 10^{19}$  cm<sup>-3</sup>. The as-implanted samples were then placed into a 1-inch atmospheric quartz tube furnace and annealed at 900°C under 300 sccm Ar and 200 sccm H<sub>2</sub> flow for 30 minutes to form iron catalyst nanoparticles on the oxide surface. After this annealing step, the gallium metal source (5N purity, Alfa Aesar) was poured into a quartz boat and placed in the tube furnace, as shown in Figure 5-1B. Next, the ion implanted and annealed substrate was placed  $\sim 3$  cm downstream of the gallium metal source. The substrate was heated up to 850°C and annealed at 850°C for 15 min under 500 sccm Ar flow. After this step, the growth was performed at 850°C for  $\sim 2$  hours with 15 sccm flow rate of NH<sub>3</sub> and 300 sccm flow rate of H<sub>2</sub>. As grown nanotubes were characterized, the as-grown nanowire samples were characterized by a JEOL JSM-6335F field emission gun scanning electron microscope (SEM), a JEOL 2010F high resolution transmission electron microscope (HRTEM) operating at 200 kV equipped with selected area electron diffraction (SAED) and energy dispersive X-ray spectroscopy (EDS) capability, a Phillips MRD X'Pert X-ray Diffraction (XRD) spectrometer with Cu K $\alpha$  radiation, and a Digital Instruments Nanoscope III Atomic Force Microscope (AFM) operated in the tapping mode. For the HRTEM characterization, the as-grown nanowires were dispersed in 2-propanol, the solution was sonicated, and a few drops of the resulting suspension was deposited on commercially available Cu TEM grids coated with a holey carbon film.

## Results and Discussion

Figure 5-2A and B show the AFM images of the SiO<sub>2</sub> substrate after the ion implantation of iron and subsequent 900°C, 30 min annealing step mentioned above for the 10<sup>15</sup> and 10<sup>16</sup> cm<sup>-2</sup> dose implants, respectively. We observed that, under the same anneal and growth conditions, the higher implant dose substrates (10<sup>16</sup> cm<sup>-2</sup>) result in a higher nanowire density compared to the lower dose ones (10<sup>15</sup> cm<sup>-2</sup>). This could be explained by the higher density of larger catalyst nanoparticles formed on the higher implant dose substrate, as evident from Figure 5-2. The flux of Fe atoms diffusing to the oxide surface is proportional to the dose of the implant; as a consequence, a higher dose results in larger nanoparticles. It is also worth noting that the AFM images in Figure 5-2 were taken after the 30 min anneal step at 900°C. During the 2 hr growth step at 850°C, the implanted Fe atoms continue to out-diffuse towards the surface, and as a result, the density and size of catalyst nanoparticles continue to evolve as the growth proceeds. This is in contrast to solution-based or thin-film catalyst, where the catalyst “dose” on the surface does not change during growth.

Next, we present the growth results of GaN nanowires from these catalyst nanoparticles for the higher implant dose substrate (10<sup>16</sup> cm<sup>-2</sup>), which was found to result in a higher density of nanowires. Figure 5-3A shows an SEM image of GaN nanowires grown from the 10<sup>16</sup> cm<sup>-2</sup> dose ion implanted iron catalyst. The diameters of the as-grown nanowires range from 15-60 nm and their lengths are between 1-20 μm based on SEM and TEM analysis. XRD measurements were performed on bulk samples to determine overall crystal structure and phase purity of the as-grown GaN nanowires. Figure 5-3B shows the XRD pattern of the as-grown GaN nanowires where the diffraction peaks labeled by their Miller indices are indexed to wurtzite GaN with lattice constants  $a = 0.3186$  nm and  $c = 0.5178$  nm.

We have also characterized the detailed structure and composition of individual GaN nanowires by HRTEM, SAED, and EDS as shown in Figure 5-4A and B, providing further experimental evidence that the as-grown nanowires are single-crystal hexagonal wurtzite GaN.

The effect of the various CVD parameters on the growth of GaN nanowires from ion implanted Fe catalyst was also investigated. The overall reaction of gallium metal vapor and ammonia to form GaN nanowires can be expressed as



First, by varying the distance between the Ga source and the substrate [see Figure 5-1B], we observed that the density of nanowires is reduced as the distance increases above 3 cm.

Furthermore, we found that increasing the growth time increases the average GaN nanowire length. Increasing the growth temperature above 900°C was found to reduce the density of GaN nanowires, most likely due to the evaporation of too much Ga from the source material at higher temperatures. In addition, having either a high (~30 sccm) or low (~5 sccm) NH<sub>3</sub> flow rate was observed to significantly reduce the density and length of as-grown GaN nanowires. These findings indicate that too much or too little supply of Ga or NH<sub>3</sub> impede GaN nanowire growth.

The presence of H<sub>2</sub> co-flow was found to be a crucial factor for GaN nanowire growth, as well. Any residual oxygen in the CVD chamber easily oxidizes the nanowires, yielding Ga<sub>2</sub>O<sub>3</sub> nanowires instead of GaN. The hydrogen co-flow prevents the oxidation of GaN nanowires, as well as reducing the decomposition rate of ammonia.

As mentioned previously in the experimental procedure, we have performed a 15 min anneal in Ar atmosphere after the furnace temperature has reached the growth temperature of 850°C. We found that this anneal step increases the GaN nanowire length and density. This

could be due to the fact that Ga begins to evaporate from the source material during this anneal step, providing a sufficient supply of Ga vapor as soon as the  $\text{NH}_3$  is introduced into the chamber in the growth step.

The growth of the GaN nanowires can be explained by the vapor-liquid-solid (VLS) growth model [147] as illustrated in Figure 5-5: First, the  $\text{SiO}_2$  substrate is implanted with  $\text{Fe}^+$ . Then, during the subsequent anneal step, the as-implanted Fe atoms out-diffuse to the surface and aggregate to form catalyst nanoparticles on the  $\text{SiO}_2$  surface. The catalyst nanoparticles from which nanowire growth has not yet nucleated could also get larger by a surface diffusion and Ostwald ripening process. During the CVD growth, liquid alloy droplets containing Fe, Ga, and N form from these catalyst nanoparticles. When these liquid alloy droplets become supersaturated in Ga and N, solid GaN nanowires nucleate and precipitate out of these droplets.

### **Conclusions**

In conclusion, we have experimentally demonstrated the catalytic CVD growth of GaN nanowires from Fe catalyst nanoparticles formed by ion implantation into thermally grown  $\text{SiO}_2$  layers and subsequent annealing. This work provides experimental evidence that ion implantation can also be used as a versatile method to create catalyst nanoparticles for wide bandgap semiconductor nanowire growth. Furthermore, we have systematically characterized the structural properties of the as-grown nanowires. We have found that the distance between the Ga source and the substrate, growth temperature, growth time, and gas flow rates are all critical parameters for nanowire growth. The growth of GaN nanowires can be explained by the catalytic VLS growth mechanisms.

This work opens up the possibility of controlling the origin of wide bandgap semiconductor nanowires at the nanometer scale using the technique of catalyst ion implantation

through a lithographically defined mask, of integrating nanowires into non-planar 3D device structures.

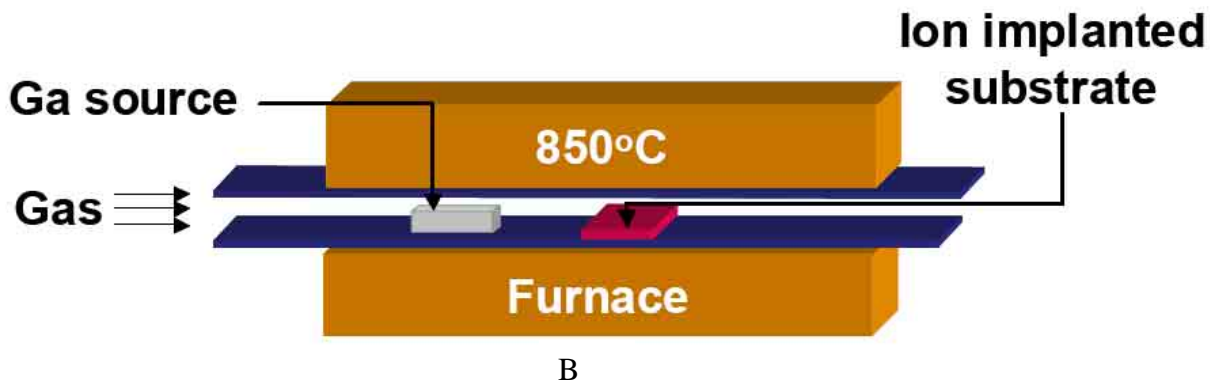
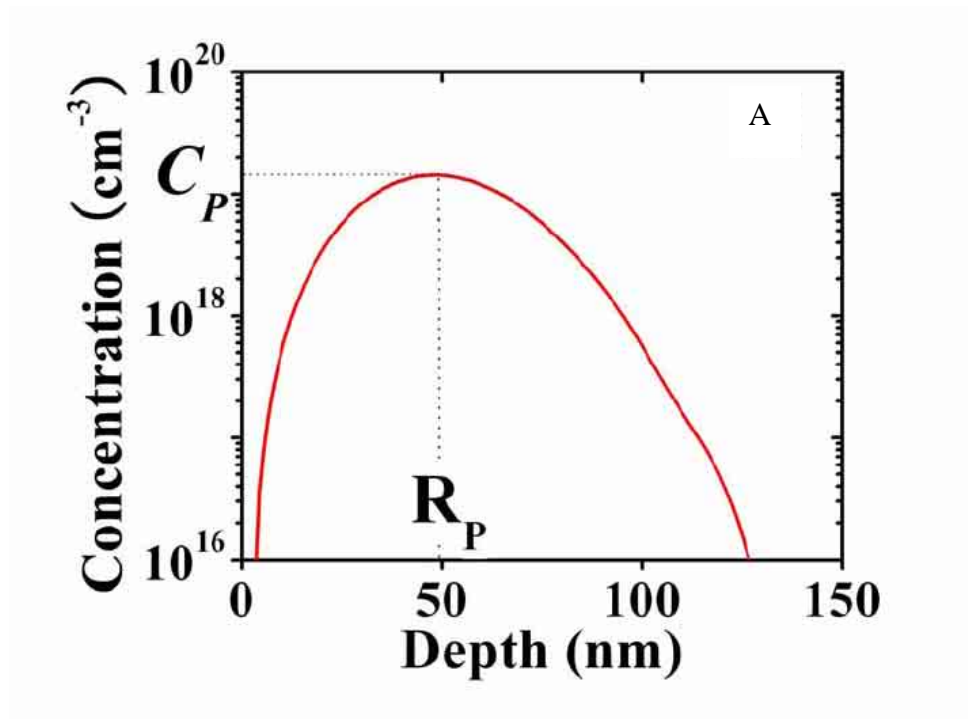


Figure 5-1. Preparation of GaN nanowire growth from ion implanted catalyst. A) Depth profile of Fe atoms ion-implanted into thermally grown SiO<sub>2</sub> at an energy of 60 keV and a dose of 10<sup>16</sup> cm<sup>-2</sup> calculated by SRIM simulations, giving a projected range of  $R_p = 50$  nm and a peak concentration of  $C_p \sim 1.5 \times 10^{19}$  cm<sup>-3</sup>, as labeled. B) Schematic of the chemical vapor deposition (CVD) setup used for GaN nanowire growth, indicating the Ga source and the ion implanted substrate.

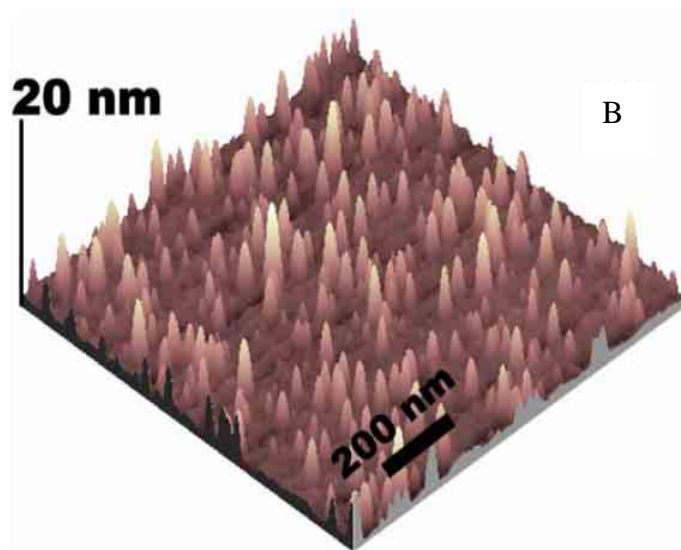
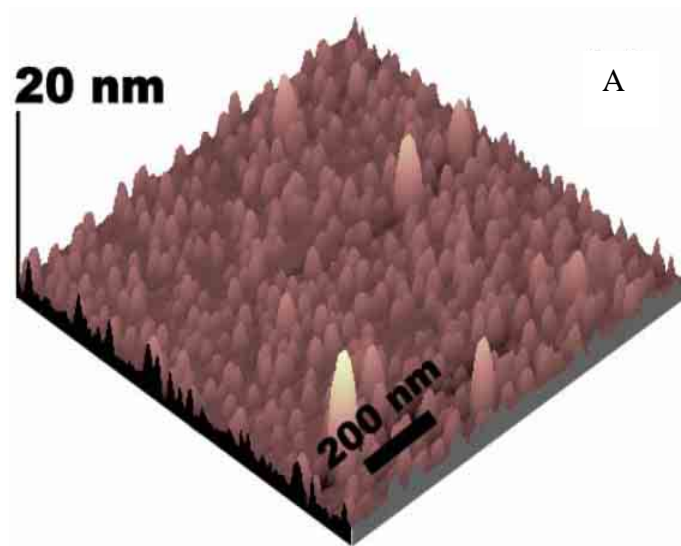


Figure 5-2. AFM images of Fe catalyst nanoparticles formed after annealing the as-implanted  $\text{SiO}_2$  substrates for 30 min at  $900^\circ\text{C}$  under Ar and  $\text{H}_2$  flow. The ion implantation energy is 60 keV and the implant doses are A)  $10^{15}$  and B)  $10^{16} \text{ cm}^{-2}$ .

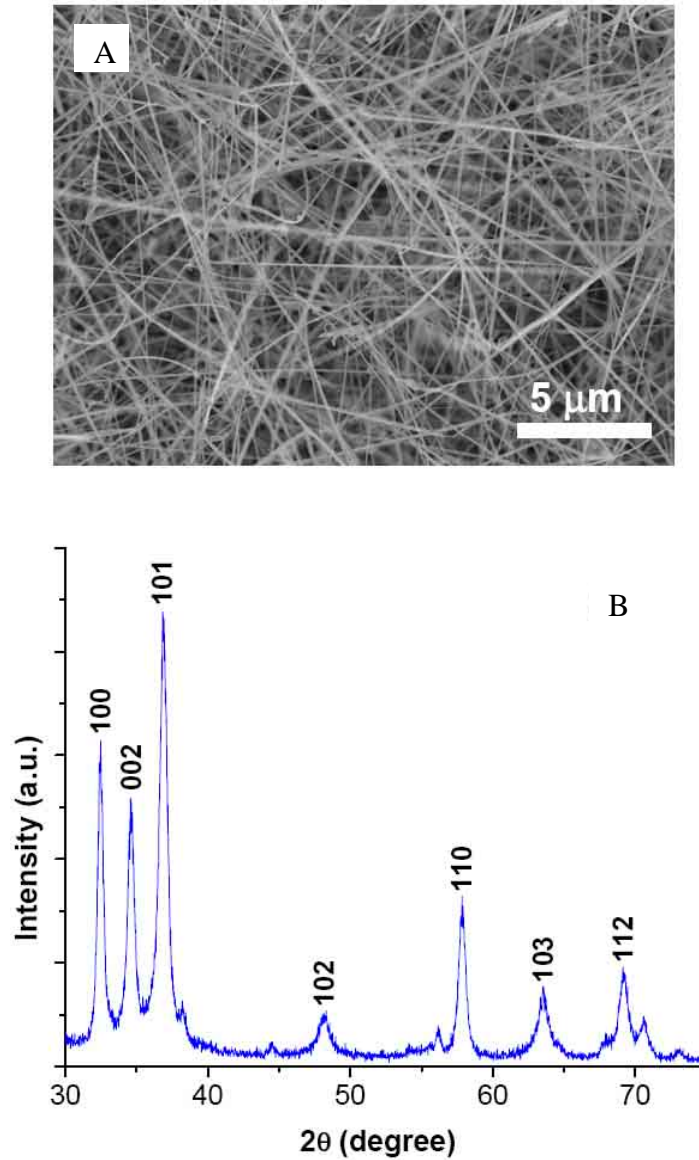


Figure 5-3 Characterizations of grown GaN nanowires. A) SEM image and B) XRD pattern of the as-grown GaN nanowires (from the  $10^{16} \text{ cm}^{-2}$  dose ion implanted Fe catalyst) where the diffraction peaks labeled by their Miller indices are indexed to wurtzite GaN with lattice constants  $a = 0.3186 \text{ nm}$  and  $c = 0.5178 \text{ nm}$ .

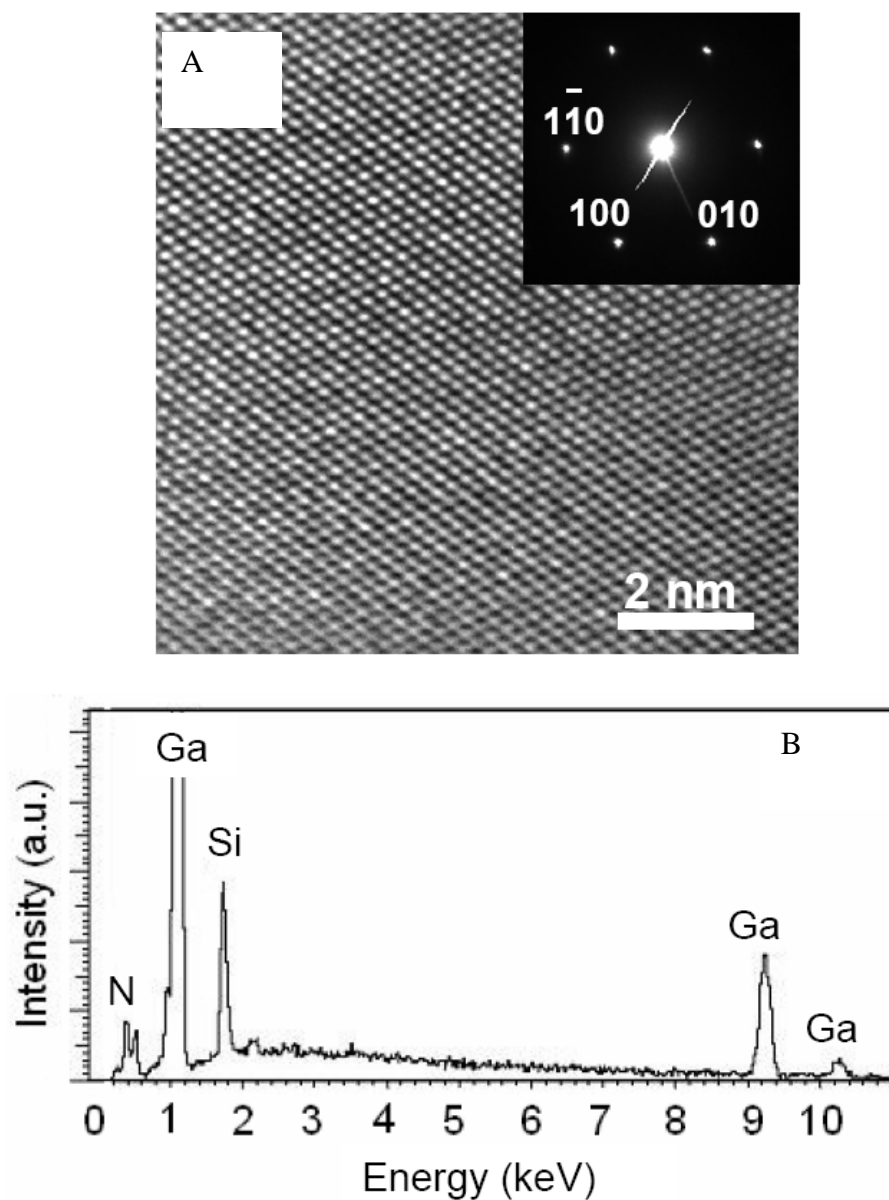


Figure 5-4. Characterizations of grown GaN nanowires. A) HRTEM image showing the selected area electron diffraction (SAED) pattern ( $\langle 001 \rangle$  zone axis) in the inset and B) Energy dispersive X-ray spectroscopy (EDS) spectrum of an individual GaN nanowire, providing further experimental evidence that the as-grown nanowires are single-crystal wurtzite GaN. The Si peak is from the substrate.

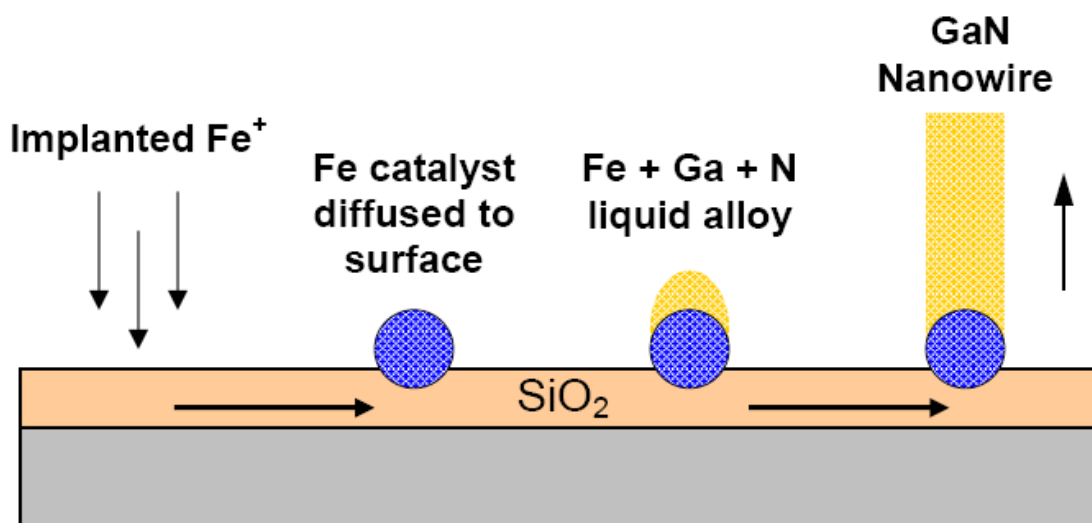


Figure 5-5. Schematic illustration of the vapor-liquid-solid (VLS) growth mechanism for GaN nanowires. First, Fe atoms are ion-implanted into the  $\text{SiO}_2$  substrate. During the subsequent anneal step, the as-implanted Fe atoms out-diffuse to the surface and aggregate to form catalyst nanoparticles on the  $\text{SiO}_2$  surface. Next, during the CVD growth, liquid alloy droplets containing Fe, Ga, and N form from these catalyst nanoparticles. Finally, when these liquid alloy droplets become supersaturated in Ga and N, solid GaN nanowires nucleate and precipitate out of these droplets.

CHAPTER 6  
NANOLITHOGRAPHIC PATTERNING OF TRANSPARENT, CONDUCTIVE SINGLE-  
WALLED CARBON NANOTUBE FILMS BY INDUCTIVELY COUPLED PLASMA  
REACTIVE ION ETCHING

**Introduction**

A single-walled nanotube film (SWNT film) is a three-dimensional film of tens of nanometers thickness, consisting of an interwoven mesh of single-walled nanotubes, as shown in Figure 6-1A. In the case of SWNT films, individual variations in diameter and chirality are ensemble averaged to yield uniform physical and electronic properties [172-175]. As a result, the reproducibility and reliability problems found in individual nanotubes are solved, and carbon nanotube film based devices can easily be mass produced in a cost effective manner. Furthermore, what makes SWNT films even more attractive for device applications is that they are flexible, transparent, and conductive. SWNT films have a resistivity on the order of  $10^{-4}$   $\Omega\text{cm}$ , and it is also optically transparent over the visible and near-infrared (near-IR) portions of the spectrum. For example, Rinzler *et al.* have demonstrated that an as-prepared nanotube film of 50 nm thickness has a transmittance greater than 70% over the visible part of the spectrum, and this transmittance increases to more than 90% in the near-IR at a wavelength of 2  $\mu\text{m}$  [172], as shown in Figure 6-1B. This transmittance is comparable to ITO [176].

These outstanding properties have established SWNT films as a new class of optically transparent and electrically conducting materials that can be used in applications such as thin film transistors [31, 32], flexible microelectronics [33-35], chemical sensors [36-39], and optoelectronic devices [40-43].

Any potential device application utilizing SWNT films requires the capability to efficiently pattern them. In this chapter, we use photolithography and e-beam lithography, and subsequent  $\text{O}_2$  plasma etching in an ICP-RIE system to pattern nanotube films down to submicron lateral

dimensions. We experimentally show that features with linewidths less than 100 nm can be successfully patterned using this technique with good selectivity and directionality. In addition, we systematically study the effect of ICP-RIE etch parameters, such as the substrate bias power and chamber pressure, on the SWNT film etch rate and etch selectivity. We also compare O<sub>2</sub> plasma etching of SWNT films in an ICP-RIE system to that in a conventional parallel plate RIE system. We find that using an ICP-RIE system significantly increases the SWNT film etch rate and the etch selectivity between the SWNT film and polymethylmethacrylate (PMMA) compared to a conventional RIE system, making it possible to pattern lateral features as small as 100 nm. The simple and efficient “top-down” patterning capability opens up tremendous opportunities for integrating SWNT films into a wide range of electronic and optoelectronic devices.

### **SWNT Film Deposition**

SWNT films were deposited by a vacuum filtration method as described in detail previously [37, 40, 172]. In summary, a dilute suspension of purified SWNTs was vacuum-filtered onto a filtration membrane. The nanotubes deposit as a thin film on the membrane with the thickness of the film controlled by the concentration of nanotubes in the suspension and the volume of the suspension filtered. The film can then be transferred onto a desired substrate by placing the film side against the substrate, applying pressure, and drying the film. To complete the process, the filtration membrane is dissolved in a solvent, leaving only the nanotube film adhered to the substrate. The substrates used in this work were (100) silicon with a 500 nm layer of thermally grown SiO<sub>2</sub> on top.

### **Lithography**

After the deposition step, the SWNT film was patterned either by photolithography or e-beam lithography. For photolithography, three different types of resist processes were used as

the mask. The first process used a 1.3  $\mu\text{m}$  thick layer of Shipley Microposit S1813 photoresist. It was found by extensive AFM imaging that when the S1813 resist is deposited directly on top of individual nanotubes, it leaves a residue [134]. On the other hand, it was observed that Microchem LOR3B lift-off resist and PMMA do not contaminate nanotubes [134]. To protect the SWNT film from potential contamination due to the S1813 resist, for the second process, a dual layer resist structure consisting of a 1.3  $\mu\text{m}$  thick S1813 layer on top of a 250 nm thick LOR3B layer was used. Finally, for the third process, a dual layer resist process consisting of a 1.3  $\mu\text{m}$  thick Shipley S1813 layer on top of a 250 nm thick PMMA layer (950K, 4% in anisole) was used. Since the S1813 resist is not in direct contact with the nanotubes in the second and third processes, no residue is left on the nanotube film during fabrication. However, PMMA cannot be exposed by the 365 nm light source available in the Karl Suss MA-6 contact mask aligner that was used for photolithography. As a result, for the third process, the S1813 layer was first exposed by the mask aligner and developed. Subsequently, the PMMA layer was patterned by  $\text{O}_2$  plasma etching with the S1813 layer acting as the mask. In all three resist processes, Shipley Microposit MF319 was used as the developer. For e-beam lithography, a single layer of PMMA (950K, 2 or 4% in anisole depending on the feature size patterned and PMMA thickness desired) was used as the masking layer, and a Raith 150 e-beam writer was used for exposure.

### **$\text{O}_2$ Plasma Etching**

After exposure and development, the nanotube film not protected by the resist mask was etched using an  $\text{O}_2$  chemistry in a Unaxis Shuttlelock ICP-RIE system. The schematic of the ICP etcher is shown in Figure 6-2. The ICP-RIE system decouples plasma density (controlled by the ICP power supply) and ion energy (controlled by the substrate power supply). As a

result, compared to conventional diode RIE systems, very high plasma densities ( $>10^{11}$  ions  $\text{cm}^{-3}$ ) can be achieved at lower pressures, resulting in more anisotropic etch profiles and significantly higher etch rates [131, 177]. Etching in ICP systems has a large physical component due to the ions combined with a chemical component.  $\text{O}_2$  plasma is commonly used for removing organic materials such as photoresist, and has also been used to etch carbon nanotubes [31, 178]. The reaction between oxygen and organic materials produces volatile species such as CO and  $\text{CO}_2$ , which are pumped out during the etch process [131]. The etch parameters for our initial SWNT etch recipe were 300 W power on the 2 MHz ICP rf supply, 100 W power on the 13.56 MHz substrate rf supply, 45 mTorr chamber pressure, and a 20 sccm  $\text{O}_2$  flow rate. In addition, a helium flow rate of 10 sccm was used to cool down the substrate. We will discuss below how changing various etch parameters affects the etch rates of the SWNT film and resists. After the ICP-RIE etch, the resist mask layers were stripped in acetone when S1813 or PMMA were used as the mask, and in Microchem Nanoremove PG when LOR3B was included in the mask, since LOR3B does not dissolve in acetone.

## **Results and Discussion**

Resulting SWNT film etch profiles were characterized by a Digital Instruments Nanoscope III AFM. Figure 6-3A shows an AFM image of a  $\sim 3$   $\mu\text{m}$  line etched in a  $\sim 20$  nm thick nanotube film using the LOR3B/S1813 dual resist photolithography process (i.e. the second process) and the initial ICP etch recipe given above. The cross-sectional height profile for the same AFM image is plotted in Figure 6-3B, showing clearly the transition between the film and the etched regions. Similar etch profiles were obtained using the other two resist processes described above. Figure 6-3C shows an AFM image of a series of lines with nanotube film width and spacing of about 200 nm patterned by e-beam lithography and ICP etching of a SWNT film

of about 14 nm thickness. The cross-sectional height profile for the same AFM image is plotted in Figure 6-3D, showing a clear transition between the film and the etched regions even at these submicron lateral dimensions.

Furthermore, Figure 6-4A and B show AFM and SEM images, respectively, of letters printed on nanotube film using e-beam lithography and ICP-RIE etching. The width of the text characters are on the order of 200-300 nm and the SWNT film thickness is 20 nm, demonstrating that the nanotube film can indeed be patterned into nanometer size structures of arbitrary shape by this fabrication method.

In order to characterize quantitatively the SWNT film and resist etch rates using the initial ICP-RIE etch recipe given above, a series of lines with equal width and spacing were partially etched in 50-100 nm thick nanotube films, such that some nanotube film still remained in the etched areas. Figure 6-5A shows an AFM image of such a series of lines with ~200 nm width and spacing partially etched in a 75 nm thick SWNT film. Unlike the lines in Figure 6-3C, the lines in Figure 6-5A have not been etched all the way down to the substrate, as evident from the texture of the remaining film visible in the etched areas. By measuring the height difference between the partially etched and not-etched film lines using cross-sectional AFM analysis, the average etch depth, and as a result, the etch rate can be calculated. For example, Figure 6-5B shows the cross-sectional AFM profile for the lines shown in Figure 6-5A, giving an average etch depth of about 19 nm for this particular sample. Dividing this depth by the etch time of 8 s, a nanotube film etch rate of ~2.4 nm/s is obtained. Furthermore, the S1813, LOR3B, and PMMA etch rates were determined by measuring the initial and final resist thicknesses using a Nanometrics Nanospec spectrometer, and dividing by the etch time. Using the initial recipe (i.e. 300 W ICP power, 100 W substrate bias power, 45 mTorr chamber pressure, 20 sccm O<sub>2</sub> flow

rate, and 10 sccm helium flow rate for substrate cooling), etch rates of 2.37, 4.59, 4.58, and 6.65 nm/s were observed for SWNT film, S1813, LOR3B, and PMMA, respectively, as listed in the first column of Table 6-1. The error bar on these etch rates is approximately  $\pm 10\%$ .

The SWNT film etch rate is similar in magnitude to the  $\sim 4$  nm/s observed in recent work using another ICP system [178]. For SWNT films of tens of nm thickness, such as those used in this work, the 2.37 nm/s etch rate of the initial recipe provides both reasonably short etch times and a good control of the etch uniformity. The selectivity  $S$  of the etch between the nanotube film and the resist mask is defined by  $S = r_{SWNT} : r_{RESIST}$ , where  $r_{SWNT}$  is the etch rate of the SWNT film and  $r_{RESIST}$  is the etch rate of the particular resist used as the mask. Using this definition, selectivity values of 1:1.94, 1:1.93, and 1:2.81 are obtained for S1813, LOR3B, and PMMA masking layers, respectively. Carbon nanotubes are much harder to etch compared to photoresists since they are chemically resistant and structurally stable [28]. As a result, the etch rate of the SWNT film is slower than that of resists in an  $O_2$  plasma, and the selectivity values are less than unity. Since the resists are used as the etch mask, they need to be thick enough to withstand the nanotube film etch. The minimum resist thickness required for a given SWNT etch process is determined by the selectivity  $S$  of the etch process. Typical S1813 and LOR3B resist thicknesses used for photolithography are larger than 1  $\mu\text{m}$ ; as a result, based on the selectivity values given above, hundreds of nm thick SWNT films can easily be patterned by photolithography. More importantly, since the PMMA etch rate is not significantly higher than the nanotube film etch rate, typical PMMA thicknesses necessary for e-beam lithography (100-300 nm) can be used to pattern thin SWNT films (i.e. less than 100 nm) down to very small ( $<100$  nm) lateral features. In short, although the etch selectivity between the SWNT film and PMMA is less than unity ( $S = 0.36$ ), it is still large enough to allow for e-

beam patterning of SWNT films. We show below that this selectivity value is much smaller ( $S = 0.09$ ) for a conventional parallel plate diode RIE system. We also show below that the SWNT film etch rate is much faster in a ICP-RIE system compared to that in a conventional RIE system. The high density plasma and low pressure achievable in an ICP-RIE system provides a large physical etch component, which results in significantly higher etch rates. As a result, the use of an ICP-RIE system is crucial in the ability to pattern SWNT films down to  $\sim 100$  nm lateral dimensions by e-beam lithography.

Aspect ratio dependent etching has been observed in some etch processes, such as silicon trench etching, resulting in a lower etch rate for smaller width trenches [131]. Using the approach described in the preceding paragraph, we systematically studied the effect of the line width on the nanotube film etch rate for widths ranging from  $50\ \mu\text{m}$  all the way down to  $100\ \text{nm}$ . The spacing between the etched lines was set equal to the width of the lines in all cases. The etch rate was found to be almost constant at  $2.37 \pm 0.3\ \text{nm/s}$ , independent of the line width etched. This is most likely due to the fact that all our samples have a SWNT film thickness  $t < 100\ \text{nm}$ . The aspect ratio  $AR$  of the nanotube film etched, defined as  $t/w$ , where  $w$  is the width of the line etched, always satisfies  $AR \leq 1$  for all the samples. In other words, the plasma density is high enough and the aspect ratio is small enough so that reactant species are able to make it to the bottom of the etched lines even for the smallest ( $100\ \text{nm}$ ) linewidths.

### **Effect of Substrate Bias Power**

Furthermore, we systematically studied the effect of changing various ICP etch parameters on the etch rates of the SWNT film and different resists, as listed in Table 6-1, using the procedure described above. To investigate the effect of the substrate bias power on the etch rate, we decreased the substrate power from  $100\ \text{W}$  to  $15\ \text{W}$ , keeping all the other etch

parameters constant as in the initial recipe. Table 6-1 shows that the nanotube film and resist etch rates are decreased by about a factor of 10 compared to those of the initial recipe. By reducing the substrate bias, the ion energy is reduced resulting in a substantially slower etch rate. A slow etch rate could be useful in applications where the SWNT film thickness is very small and the etch rate and uniformity needs to be precisely controlled.

### **Effect of Chamber Pressure**

To investigate the effect of chamber pressure on the etch rate, we decreased the chamber pressure from 45 mTorr to 10 mTorr, keeping all the other etch parameters constant as in the initial recipe. Table 6-1 shows that the nanotube film and resist etch rates increase by a factor between 1.7 and 3.5 compared to those of the initial recipe. A lower chamber pressure results in a more directed etch because of fewer gas-phase collisions in the sheath, and also increases the etch rates due to a larger physical etch component. A faster etch rate could be useful in applications where the SWNT film thickness is large. Furthermore, by taking the ratio of the etch rates listed in Table 6-1, selectivity values of 1:0.95, 1:1.21, and 1:1.59 are obtained for S1813, LOR3B, and PMMA masking layers, respectively. These selectivity values are higher than those of the initial recipe. This is likely due to an increase in the physical etch component, which etches the nanotube film and resists at similar rates. In addition, increasing the chamber pressure from 45 mTorr to 100 mTorr (maximum pressure achievable in our system) was found not to change the etch rates of the nanotube film and resists significantly.

### **Effect of Substrate Cooling**

Furthermore, we have investigated the effect of substrate cooling on the etch rates of the SWNT film and resists. Increasing the helium flow rate (which actively cools the substrate) from 10 sccm to 40 sccm, keeping all other etch parameters constant as in the initial recipe, did not change the etch rates of the SWNT film and resists compared to those of the initial recipe.

## **Comparison to Parallel-Plate RIE System**

To compare the etch rates of SWNT film and the three resists in an ICP-RIE system to those in a conventional parallel plate RIE system, we have also etched the SWNT film and resists using a Plasma Sciences RIE 200W etcher, in which there is only one rf power source of 13.56 MHz frequency, and as a result, the plasma density and the ion energy are no longer decoupled. Using an rf power of 30 W, O<sub>2</sub> flow rate of 12.5 sccm, and a chamber pressure of 140 mTorr, we have observed that the etch rates of both the SWNT film and resists are substantially lower in this system, as listed in the last column of Table 6-1. The etch rate of the SWNT film in the conventional RIE system was 0.05 nm/s, which is about 5 times slower than that in the ICP-RIE system even with a low substrate bias power of 15 W (See Table 6-1). This is due to a lower plasma density in the conventional RIE system. Furthermore, for the conventional RIE system, the etch selectivity between the SWNT film and the resist mask has decreased to 1:2.8, 1:3.8, and 1:11 for S1813, LOR3B, and PMMA, respectively. This is due to a reduction in the physical etching component using the conventional RIE system. These results demonstrate that the use of an ICP etcher provides significant advantages, such as faster etch rates and better selectivity, over conventional parallel plate plasma systems in order to be able pattern submicron features in nanotube films.

## **Conclusions**

In conclusion, in this chapter, we have demonstrated the ability to efficiently pattern SWNT films with good selectivity and directionality down to submicron lateral dimensions by photolithography or e-beam lithography and O<sub>2</sub> plasma etching using an ICP-RIE system. We systematically studied the effect of ICP-RIE etch parameters on the nanotube film etch rate and etch selectivity. Decreasing the substrate power from 100 W to 15 W, decreased the nanotube film and resist etch rates by about a factor of 10. Decreasing the chamber pressure from 45

mTorr to 10 mTorr increased the nanotube film and resist etch rates by a factor between 1.7 and 3.5. It also increased the etch selectivity between the nanotube film and the resist masks. On the other hand, increasing the chamber pressure from 45 mTorr to 100 mTorr did not change the etch rates of the nanotube film and resists significantly. Similarly, increasing the helium flow rate (which actively cools the substrate) from 10 sccm to 40 sccm did not produce a significant change on the etch rates of the SWNT film and the three resists. Furthermore, the SWNT film etch rate was found to be independent of the line width etched for linewidths ranging from 50  $\mu\text{m}$  down to 100 nm. In addition, by comparing the etch rates of SWNT film and the three resists in an ICP-RIE system to those in a conventional parallel plate RIE system, we have demonstrated that using an ICP-RIE system provides significant advantages, such as faster etch rates and better etch selectivity, over conventional parallel plate RIE plasma systems, making it possible to pattern lateral features as small as 100 nm in nanotube films.

In short, the simple and efficient “top-down” patterning capability developed in this chapter could open up tremendous opportunities for integrating single-walled nanotube films into a wide range of electronic and optoelectronic devices.

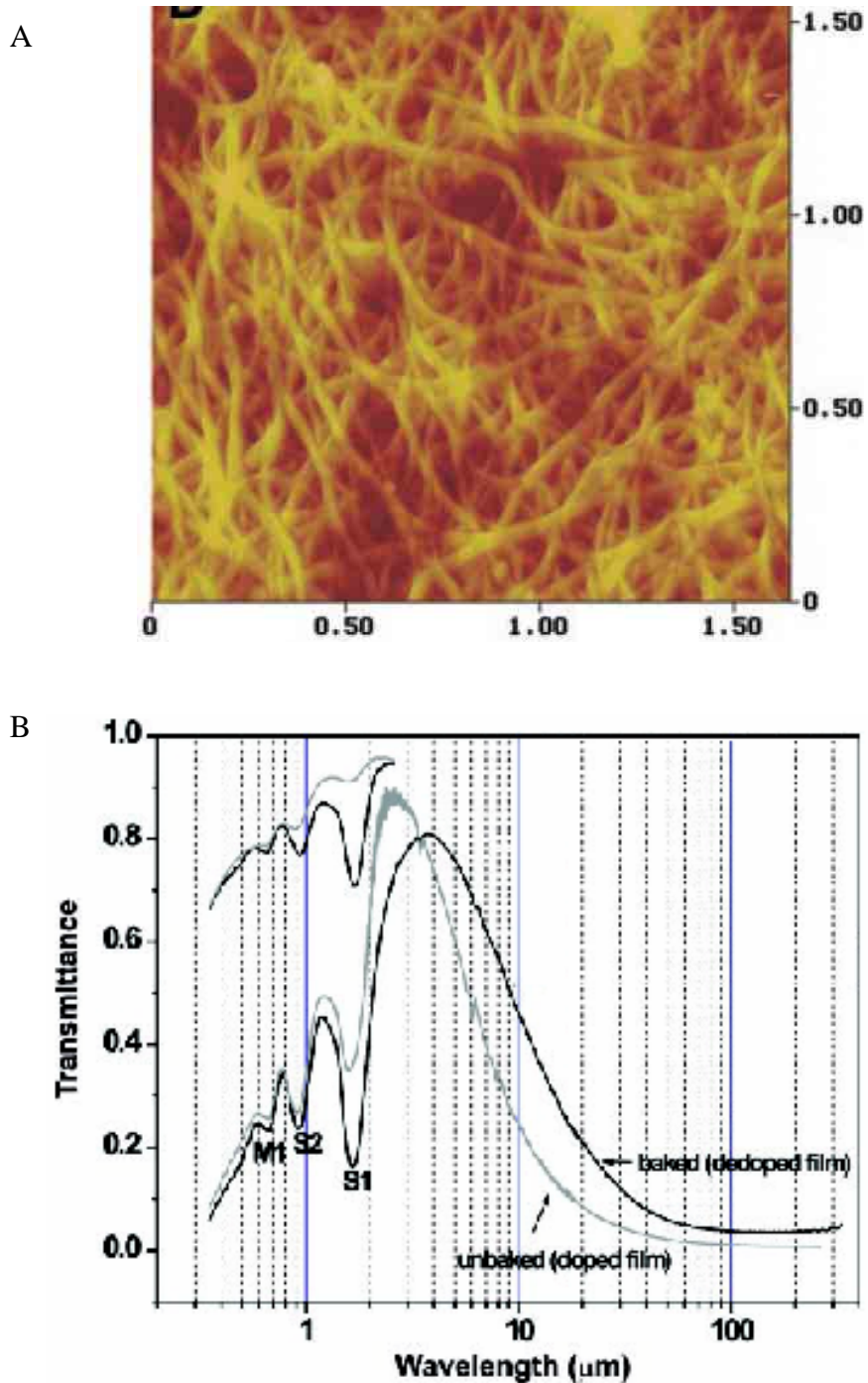


Figure 6-1. Image and optical properties of SWNT films. A) Atomic force microscope (AFM) image of a 150 nm thick film and B) transmittance spectra for two films of thickness 50 nm and 240 nm. The curves with higher transmittance shown in the upper left are for the 50 nm film. The gray curve shows the transmittance of unbaked film and the black curve represents the transmittance of baked (dedoped) film. (Taken from Ref. [172])

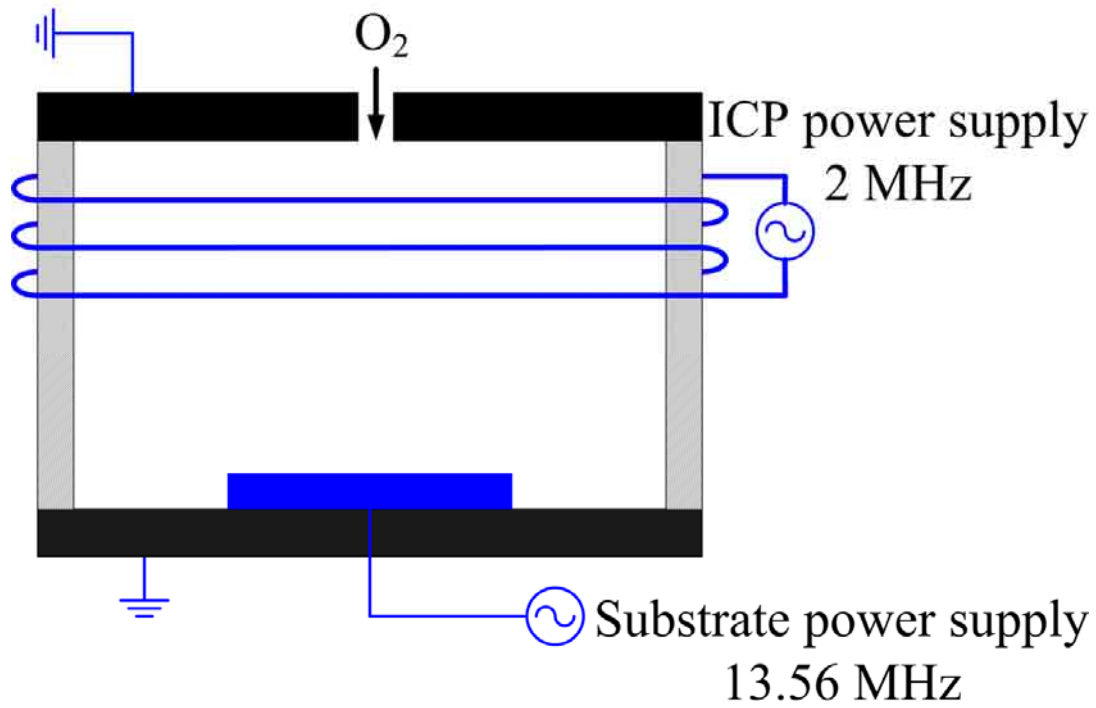


Figure 6-2. Schematic of ICP-RIE system showing separated ICP and substrate power supplies.

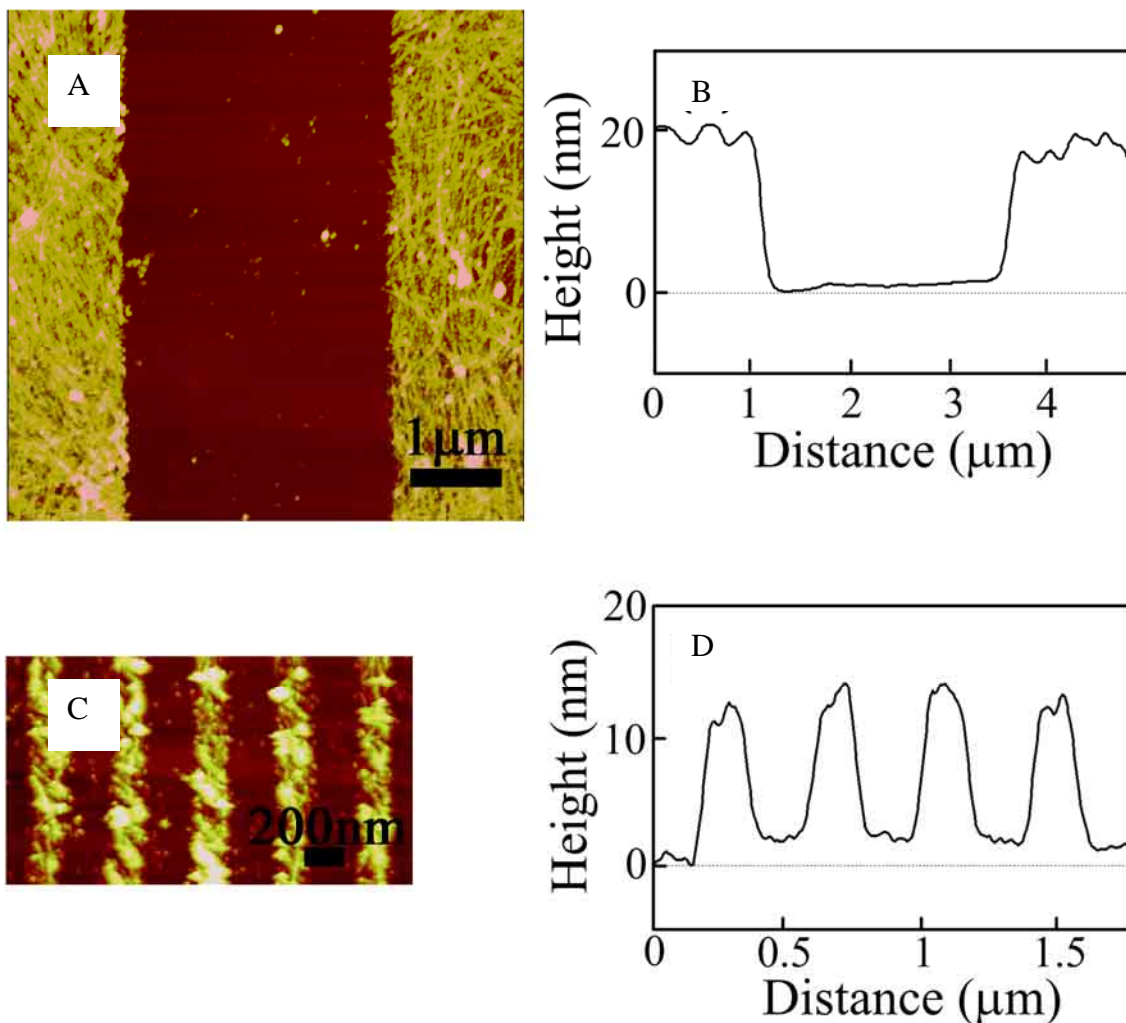


Figure 6-3. Images of patterned SWNT films. A) Top view AFM image of a  $\sim 3 \mu\text{m}$  line etched in a  $\sim 20 \text{ nm}$  thick SWNT film using the LOR3B/S1813 dual layer resist photolithography process and the initial ICP etch recipe described in the text. The  $\text{SiO}_2$  substrate is exposed in the center area, where the film is completely removed. The SWNT mesh making up the nanotube film is clearly visible at the left and right of the AFM image. B) Cross-sectional height data for the AFM image of part A. C) AFM image of a series of nanotube film lines having equal widths and spacings of  $\sim 200 \text{ nm}$ , patterned on  $\text{SiO}_2$  by e-beam lithography and ICP-RIE etching, as described in the text. The film thickness is  $\sim 14 \text{ nm}$ . D) Cross-sectional height data for the AFM image of part C.

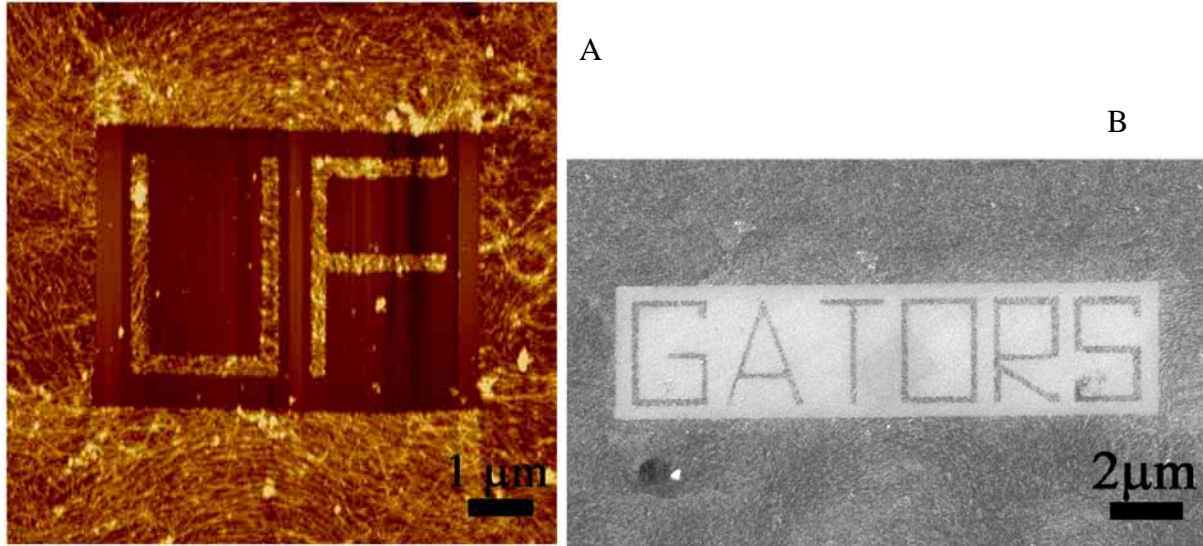


Figure 6-4. Text characters printed in SWNT film by e-beam lithography and ICP-RIE etching, A) AFM image of “UF” and B) SEM image of “GATORS”. The width of the text characters are on the order of 200-300 nm and the SWNT film thickness is 20 nm.

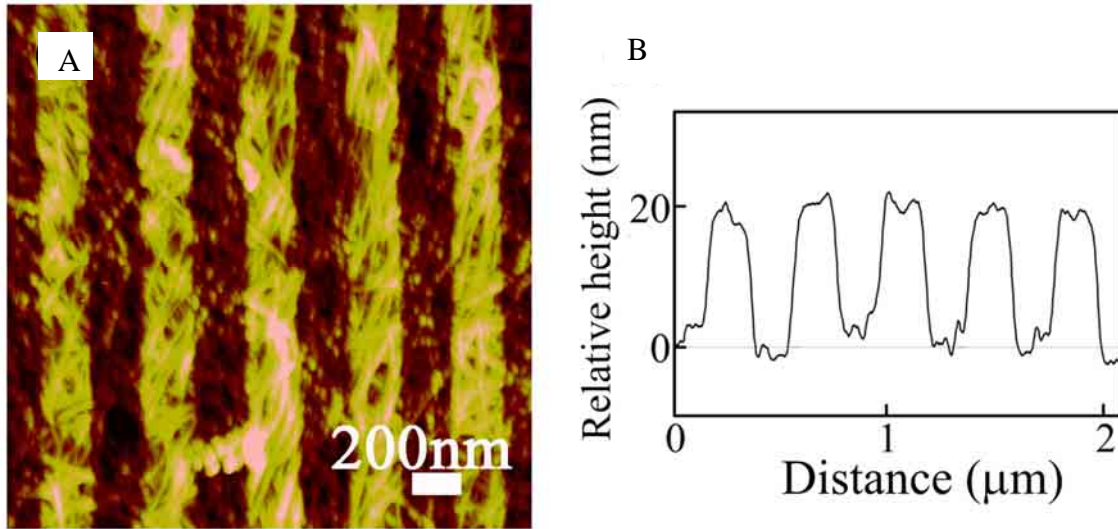


Figure 6-5. Images of patterned SWNT films. A) AFM image of a series of nanotube film lines having equal widths (and spacings) of  $\sim 200$  nm half-way etched in a 75 nm thick SWNT film by e-beam lithography and ICP-RIE etching, as described in the text. Unlike the lines shown in the AFM image of Figure 6-3C, the lines in this AFM image have not been etched all the way down to the substrate, as evident from the texture of the remaining film mesh visible in the etched areas. The scale bar is 200 nm. B) Cross-sectional height data for the AFM image of part A, showing an average etch depth of about 19 nm for this particular sample. The etch rate can be calculated by dividing this etch depth by the total etch time.

Table 6-1 Etch rates of SWNT film and three different resists (S1813, LOR3B, and PMMA) under different plasma etch conditions using Unaxis Shuttlelock ICP-RIE system and Plasma Sciences RIE 200W system.

Material	ICP-RIE System Etch Rates (nm/s)			Parallel Plate RIE System Etch Rate (nm/s)
	Initial recipe	Low Substrate Bias Power (15 W)	Low Chamber Pressure (10 mTorr)	
SWNT film	2.37	0.23	8.28	0.05
S1813	4.59	0.39	7.85	0.14
LOR3B	4.58	0.44	10.0	0.19
PMMA	6.65	0.63	13.2	0.55

Note: The initial ICP-RIE recipe in column I corresponds to an ICP power of 300 W, substrate bias power of 100 W, chamber pressure of 45 mTorr, and O<sub>2</sub> flow rate of 20 sccm. In addition, a Helium flow rate of 10 sccm was used to cool down the substrate. The headings of the other columns indicate the parameters changed compared to the initial recipe, with all the other parameters kept constant. The parallel plate RIE system etch parameters were rf power of 30 W, O<sub>2</sub> flow rate of 12.5 sccm, and a chamber pressure of 140 mTorr.

CHAPTER 7  
FABRICATION AND DARK CURRENT CHARACTERIZATION OF METAL-  
SEMICONDUCTOR-METAL (MSM) PHOTODETECTORS WITH TRANSPARENT AND  
CONDUCTIVE CARBON NANOTUBE FILM SCHOTTKY ELECTRODES

**Introduction**

Among various photodetector structures, metal-semiconductor-metal (MSM) photodetectors (PDs) are one of the most promising candidates for monolithic integration in optoelectronic integrated circuits (OEICs). An MSM photodetector is an optoelectronic device that absorbs optical energy and converts it to electrical energy in the form of a photocurrent. Photodetectors are widely used in optical communication systems. An MSM photodetector is fabricated by forming two Schottky contacts on an undoped semiconductor layer. The typical configuration is metal contacts in the form of interdigitated finger electrodes placed on a semiconductor substrate, as shown in Figure 7-1. The semiconducting material is reverse biased to form a depletion layer and create an electric field for photogenerated carriers to flow through. This produces a small leakage current called the dark current, and should be minimized to reduce power dissipation of the device, and increase its sensitivity. When the device is exposed to light, its absorption in the semiconductor layer creates electron/hole pairs that are swept out of the absorbing semiconducting layer by the electric field, creating the photocurrent. The advantages of MSM PDs compared to other commonly used detectors, such as PIN diodes and avalanche photodiodes, are simplicity of fabrication, low cost, opportunity for monolithic integration, potentially large bandwidth, and very low capacitance [179]. The low capacitance can be extremely useful in reducing the amplifier noise and increasing signal to noise ratio of an optical link [180]. However, the main disadvantage limiting the widespread use of MSM PDs is their low responsivity due to the reflection of light by the metal electrodes on

top of the semiconductor. This results in a low photocurrent-to-dark current ratio defined as  $PDR = I_{photo} / I_{dark}$ .

In this chapter, we successfully integrate transparent and conductive single-walled carbon nanotube film (SWNT film) electrodes with GaAs substrates to make hybrid Schottky MSM PDs. We demonstrate the Schottky behavior of SWNT film contacts on GaAs by fabricating and characterizing Metal-Semiconductor-Metal (MSM) devices with SWNT film electrodes. Furthermore, we study the effect of device geometry on the dark current of these SWNT film-GaAs MSM devices. In recent previous work, SWNT films have only been demonstrated as ohmic contacts in optoelectronic devices, such as GaN light-emitting diodes (LEDs) [40], organic solar cells [41, 43], and organic LEDs [42]. Furthermore, unlike applications based on individual SWNTs, SWNT films do not suffer from reliability and reproducibility problems, since individual variations in diameter, chirality, location, and direction are ensemble averaged to yield uniform physical and electronic properties.

### **Experimental Method**

MSM photodetectors with SWNT film electrodes were fabricated on nominally undoped ( $\sim 2.1 \times 10^8 \Omega\text{cm}$ ) (100) GaAs substrates. After the GaAs substrate was cleaned by solvents, a  $\sim 100$  nm thick silicon nitride (SiN) isolation layer was deposited on the substrate using plasma enhanced chemical vapor deposition (PECVD) [Figure 7-2A]. Subsequently, active area windows of various dimensions were opened in the SiN film using plasma etching. This was followed by the deposition of  $\sim 40$  nm thick SWNT film, prepared by vacuum-filtration as explained in detail previously [40, 172, 181] [Figure 7-2B]. The deposited SWNT film had a resistivity of about  $10^{-4} \Omega\text{cm}$ . The SWNT film was then patterned into interdigitated finger electrodes by photolithography and inductively coupled plasma etching (ICP), using a method

we have described previously [181, 182] [Figure 7-2C]. Finally, for ease of electrical probing, a Chromium/Palladium (7 nm/43 nm) metal stack was patterned on the nanotube film contact pads using photolithography, e-beam evaporation, and subsequent lift-off [Figure 7-2D]. The SWNT film contact pads end up on top of the SiN isolation, which eliminates parasitic leakage paths, and therefore reduces the dark current [183]. Figure 7-2E shows the optical microscope image of a finished MSM device and Figure 7-2F shows the Atomic Force Microscope (AFM) image of the area between two SWNT film electrode fingers. In order to study the effect of device geometry on the dark current, MSM devices with different active area width  $FW$ , finger length  $FL$ , finger width  $W$  and finger spacing  $S$  were fabricated. These dimensions are labeled in Figure 7-2E. Finger widths smaller than 5  $\mu\text{m}$  were not used, since it has been shown by 4-point-probe measurements and Monte Carlo simulations that the SWNT film resistivity increases strongly at smaller widths, because the film approaches the percolation threshold [181, 184].

### **Result and Discussion**

The Figure 7-3 shows the dark  $I$ - $V$  characteristics of this device at room temperature (294 °K) in linear scale. The data clearly exhibit the characteristic  $I$ - $V$  curves of two back-to-back Schottky diodes making up the MSM photodetector [185-187], demonstrating that the SWNT film indeed makes a *Schottky* contact to GaAs. Furthermore, the symmetry of the  $I$ - $V$  curve in the inset demonstrates that the two metal-semiconductor (M-S) contacts are identical, implying that the SWNT film acts as a uniform material. In an MSM structure, at high applied voltage, one of the M-S contacts is reverse biased and the other one forward biased; and as a result, the reverse biased contact limits the current and results in current saturation [185, 188]. However, Figure 7-3 shows that after the first steep rise, the current does not completely saturate at high voltages, but slowly increases with increasing voltage. This slow increase in the current

at higher voltages can be explained by Schottky barrier lowering due to charge accumulation at surface states, and image force lowering at the edges of the electrodes where there is a strong electric field, as previously reported for MSM photodetectors [189, 190].

Next, we study the effect of the device geometry on the dark  $I$ - $V$  characteristics at room temperature (294 °K). Figure 7-4A shows the dark  $I$ - $V$  curves for devices with identical  $W$ ,  $FL$ , and  $FW$ , but with  $S$  ranging from 10 to 20  $\mu\text{m}$ . Increasing the spacing in these devices (with the same area) decreases the number of finger pairs  $n$ , which is given by  $n = FW / 2(W + S)$ . This decrease in turn reduces the amount of dark current in the device, in agreement with the trend observed in Figure 7-4A. Figure 7-4B shows the dark  $I$ - $V$  curves for devices with identical  $FL$  and  $FW$ , but with  $W = S$  ranging from 15 to 30  $\mu\text{m}$ . The dark current is found to monotonically decrease with an increase in  $W$ . It has been observed that in MSM detectors, beyond a certain finger width, the dark current becomes roughly independent of the width  $W$ , and is proportional to the product of  $FL$  and  $n$  [191]. This is due to current crowding at the edges of the electrodes as illustrated explicitly in Figure 7-4C, which shows a MEDICI [192] simulation of the cross-sectional current density distribution in the GaAs substrate between two electrode fingers ( $W = S = 20 \mu\text{m}$ ) at  $V = 3 \text{ V}$  bias. It is evident from this simulation that current crowding occurs at the electrode edges, which results in the effective device area to be weakly dependent on the width of the electrode. Therefore, since  $FL$  and  $FW$  are constant and  $W = S$  for all the devices shown in Figure 7-4B,  $n$ , thus the dark current should be inversely proportional to  $W$ , in agreement with the observed trend in the figure. Finally, Figure 7-4D shows the dark  $I$ - $V$  curves for devices with identical  $W$  and  $S$ , but with  $FL = FW$  ranging from 200 to 400  $\mu\text{m}$ . In this case, both  $FL$  and  $n$  (which depends linearly on  $FW$ ) vary, resulting in a strong change in the amount of dark current, in agreement with the trend observed in Figure 7-4D. These results show that the dark

current in SWNT film-GaAs MSM devices scales rationally with device geometry. Ongoing work by other students in our group include extracting the barrier height of SWNT film-GaAs Schottky contacts using temperature-dependent  $I$ - $V$  measurements and characterizing the photocurrent of these MSM devices.

### **Conclusions**

In summary, we have fabricated and characterized the effect of device geometry on the dark current of MSM photodetectors based on SWNT film-GaAs Schottky contacts. We have observed that dark currents of the MSM devices scale rationally with device geometry, such as the device active area, finger width, and finger spacing. The results open up the possibility of integrating SWNT films as transparent and conductive Schottky electrodes in conventional semiconductor electronic and optoelectronic devices.

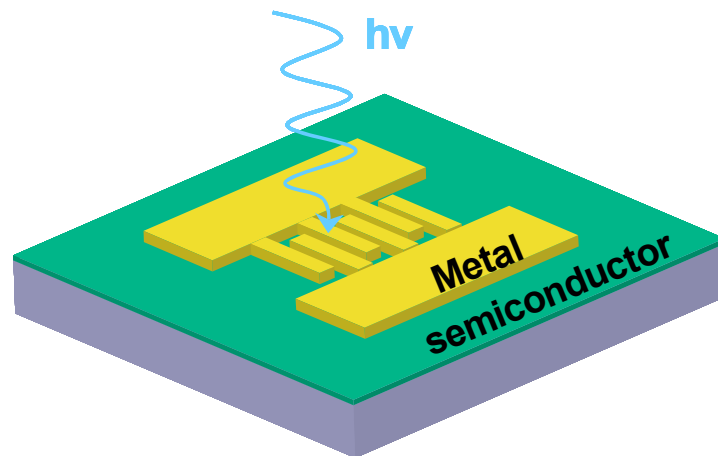


Figure 7-1. Schematic of MSM photodetector with interdigitated metal finger electrodes on top of semiconducting layer. When the photodetector is illuminated with light, electron/hole pairs are created in the semiconductor, which are swept out of the absorbing semiconducting layer by the electric field between the metal finger electrodes, creating a photocurrent.

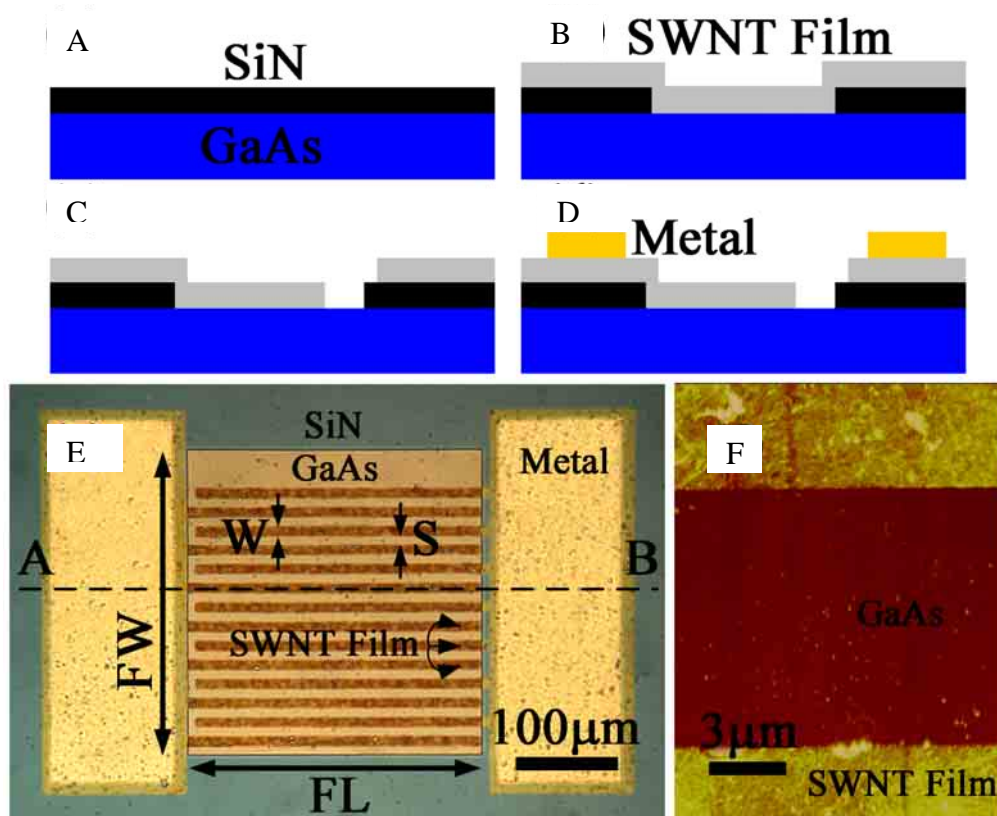


Figure 7-2. Schematic of process flow for MSM photodetectors with SWNT film electrodes along the dashed line *AB* shown in part E: A) SiN isolation layer deposited on a GaAs substrate, B) SWNT film prepared by vacuum-filtration deposited on the substrate after opening the active windows in the SiN layer, C) SWNT film patterned into interdigitated electrode fingers by photolithography and inductively coupled plasma (ICP) etching, and D) Cr/Pd metal contacts patterned on the nanotube film contact pads using photolithography, e-beam evaporation, and subsequent lift-off. E) Optical microscope image of the finished MSM photodetector, showing the various device dimensions. F) Atomic Force Microscope (AFM) image showing the area between two SWNT film electrode fingers of the MSM device of part E.

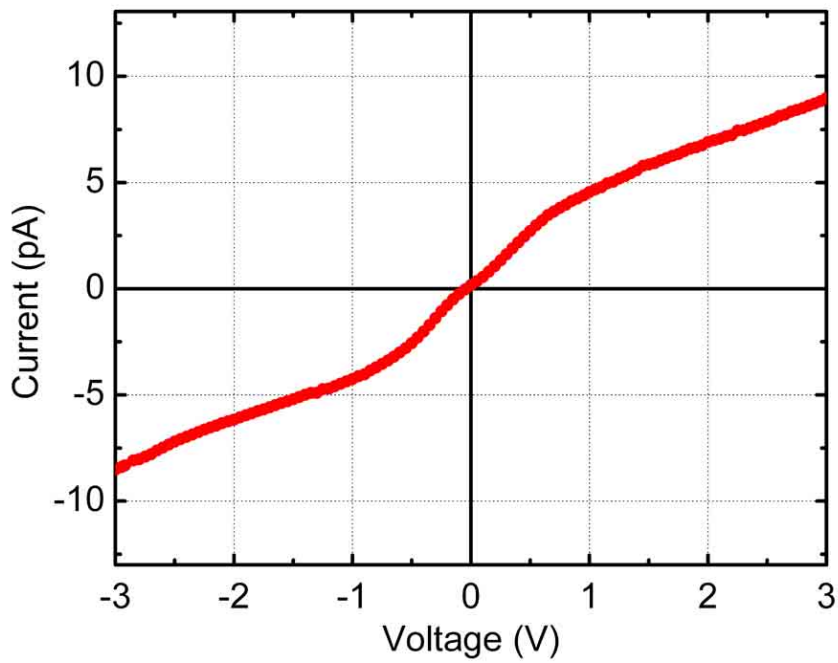


Figure 7-3. Dark current versus applied voltage measured at room temperature (294 °K) for a SWNT film-GaAs MSM device with  $W = S = 15 \mu\text{m}$  and  $FL = FW = 300 \mu\text{m}$ . The data clearly exhibit the characteristic  $I$ - $V$  curves of two back-to-back Schottky diodes making up the MSM photodetector, demonstrating that the SWNT film indeed makes a Schottky contact to GaAs.

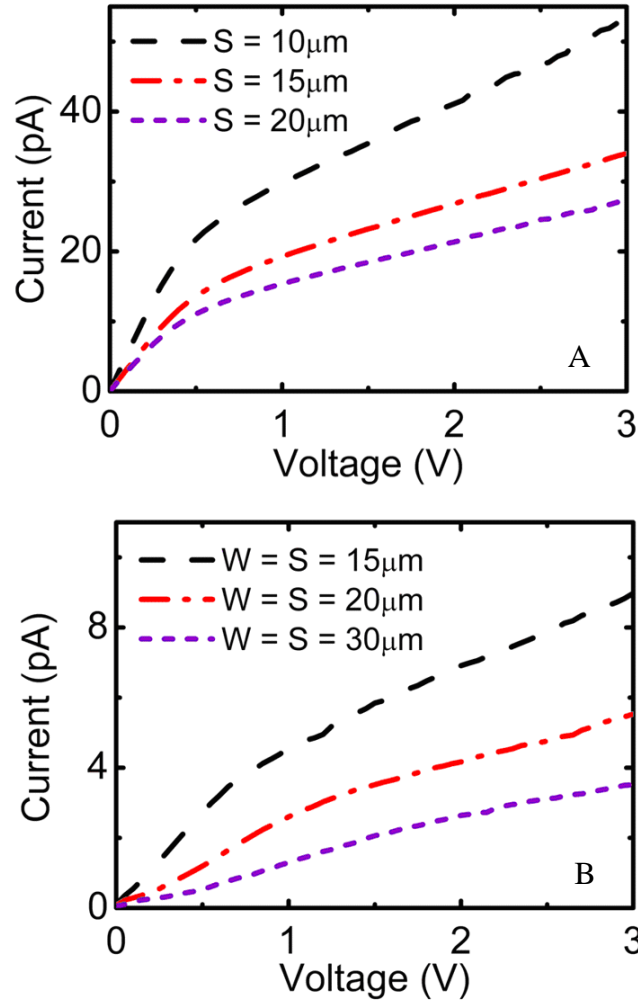


Figure 7-4. Dark current of fabricated MSM device. A) Dark current versus applied voltage at room temperature (294 °K) for SWNT film-GaAs MSM devices with  $W = 5 \mu\text{m}$  and  $FL = FW = 400 \mu\text{m}$ , but with spacing  $S$  ranging from 10 to 20  $\mu\text{m}$ , as labeled in the figure. B) Dark current versus applied voltage for SWNT film-GaAs MSM devices with  $FL = FW = 300 \mu\text{m}$ , but with  $W = S$  ranging from 15 to 30  $\mu\text{m}$ , as labeled in the figure. C) MEDICI simulation of the cross-sectional current density distribution in the GaAs substrate between two SWNT film electrode fingers ( $W = S = 20 \mu\text{m}$ ) at  $V = 3 \text{ V}$  bias. Darker colors correspond to higher current density (courtesy of Ashkan Behnam). D) Dark current versus applied voltage for SWNT film-GaAs MSM devices with  $W = 5 \mu\text{m}$  and  $S = 15 \mu\text{m}$ , but with  $FL = FW$  ranging from 200 to 400  $\mu\text{m}$ , as labeled.

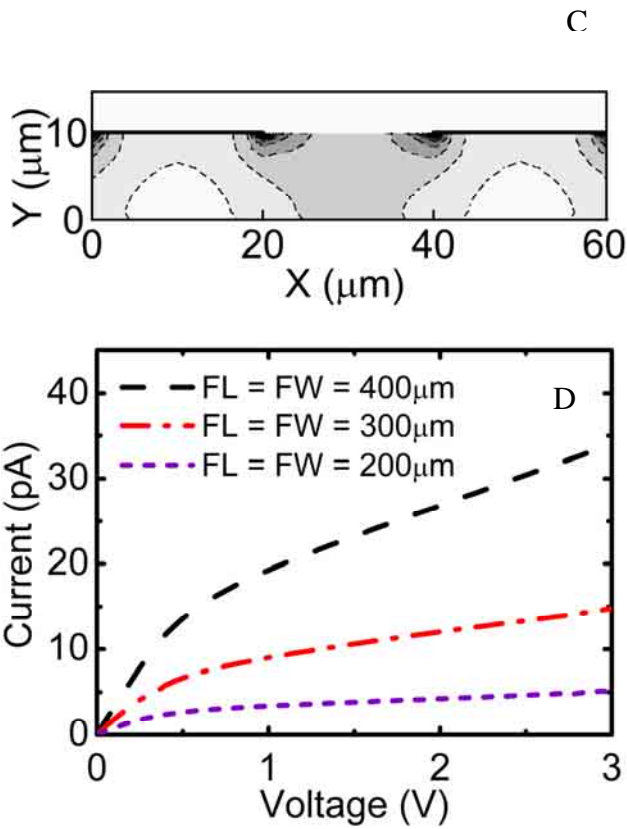


Figure 7-4. Continued

## CHAPTER 8 CONCLUSIONS AND FUTURE WORK

### Conclusions

This dissertation is mainly divided into two subjects. The first subject is nucleating the growth of nanomaterials by the ion implantation technique. We have shown experimental evidence that single-walled carbon nanotubes (SWNT) and  $\text{SiO}_x$  and GaN nanowires can be grown by Fe ion implantation into  $\text{SiO}_2/\text{Si}$  substrates, subsequent annealing, and CVD growth. Moreover, we have shown that there is a dose and energy window of ion implantation in which SWNT and nanowire growth are observed for a given growth condition. For nanomaterials growth, catalyst is usually spun on or drop-dried from a liquid solution containing iron nanoparticles or deposited as solid thin film layers by evaporation or sputtering. However, it is not possible to pattern the liquid solution-based catalyst into very small dimensions or the thin film catalyst into nonplanar three-dimensional (3D) device structures, such as the sidewalls of high aspect ratio trenches. By adopting ion implantation technique for nanomaterials growth, this thesis opens up the possibility of controlling the origin of nanomaterials at the nanometer scale and of integrating nanomaterials into nonplanar 3D device structures with precise dose control. We also have fabricated micromachined Si TEM grids for direct TEM, as well as AFM, SEM, and Raman characterization of as-grown nanomaterials. As a result, these micromachined TEM grids offer fast, easy, and reliable structural characterization. Furthermore these grids provide a low cost, mass producible, efficient, reliable, and versatile platform for direct TEM, AFM, SEM, and Raman analysis of as-grown nanomaterials, eliminating the need for any post-processing growth.

The second subject is the fabrication and characterization of single-walled carbon nanotube films which are three-dimensional films of tens of nanometers thickness, consisting of an

interwoven mesh of single-walled carbon nanotubes. We have demonstrated, for the first time, patterning of SWNT films down to submicron lateral dimensions as small as 50 nm using e-beam lithography and inductively coupled plasma (ICP) etching. This simple and efficient “top-down” patterning capability developed could open up tremendous opportunities for integrating single-walled nanotube films into a wide range of electronic and optoelectronic devices. Furthermore, we have fabricated and characterized the effect of device geometry on the dark current of MSM photodetectors based on SWNT film-GaAs Schottky contacts. We have observed that dark currents of the MSM devices scale rationally with device geometry, such as the device active area, finger width, and finger spacing. These results open up the possibility of integrating SWNT films as transparent and conductive Schottky electrodes in conventional semiconductor electronic and optoelectronic devices.

### **Suggestions for Future Work**

Future work could include fabricating nanotube and nanowire devices such as field effect transistors (FETs), sensors, and light-emitting diodes (LEDs) by using ion implanted catalyst. As mentioned in the previous chapters, ion implanted catalyst could make it possible to grow nanomaterials at desired locations and integrate them into 3D structures. Moreover, it is possible to control density of nanomaterials during growth by adjusting the dose and energy. With these capabilities, more efficient and advanced nanotube and nanowire devices can be designed and fabricated in a controllable way.

SWNT films can be integrated with conventional semiconductors for the microfabrication of electronic and optoelectronic devices such as transistors, lasers, solar cells, and photodiodes. Future work is needed to measure the photocurrent of SWNT film-GaAs MSM photodetectors to extract and compare the responsivity with conventional MSM devices. Moreover, future work is needed to measure the  $I$ - $V$  characteristics of SWNT film-GaAs Schottky contacts as a function

of temperature and their  $C$ - $V$  characteristics in order to experimentally extract the Schottky barrier height. Furthermore, MSM devices with various geometries using SWNT film electrodes on other substrates such as silicon and germanium could be fabricated.

APPENDIX A  
MASK LAYOUT

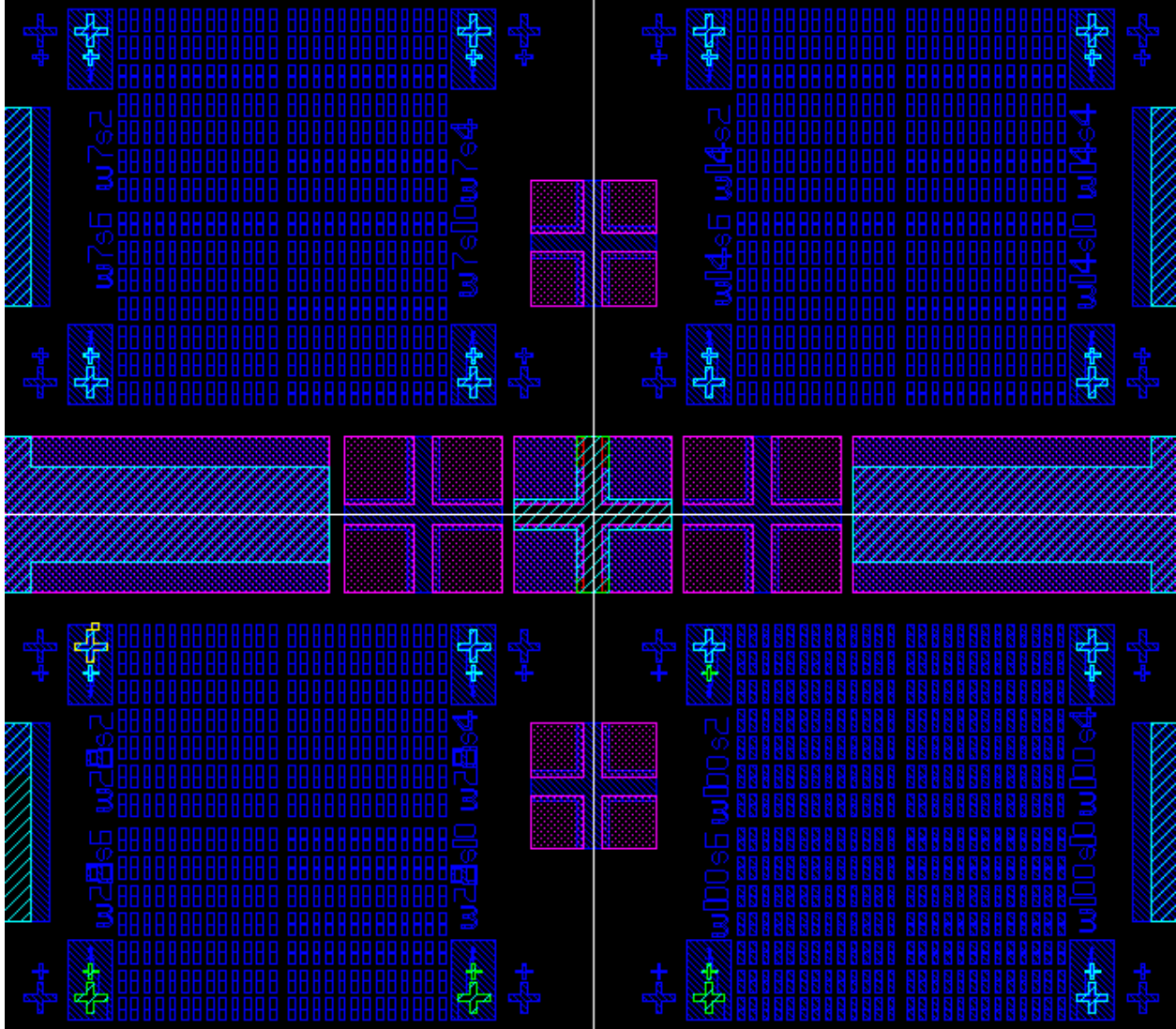


Figure A-1. Mask layout for nanotube device fabrication. Mask has four different electrode widths (7, 14, 28, and 100  $\mu\text{m}$ ) and each width has four different electrode spacings (2, 4, 6, and 10  $\mu\text{m}$ ).

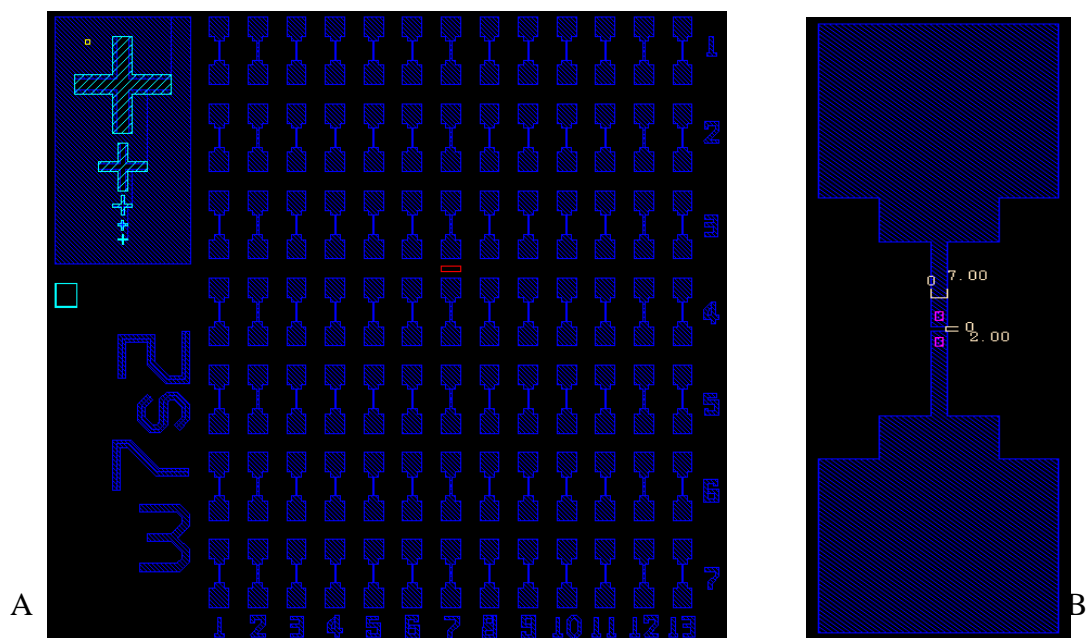


Figure A-2. Mask layout. A) area where electrodes have 7  $\mu\text{m}$  width and 2  $\mu\text{m}$  spacing. B) device which has 7  $\mu\text{m}$  width and 2  $\mu\text{m}$  spacing. Blue color areas are places for metals and red boxes are designed for patterning catalysts on top of electrodes.

## LIST OF REFERENCES

- [1] Extending the road beyond CMOS in IEEE Circuits and Devices Magazine (2002), Vol. 18, p. 28.
- [2] Semiconductor Industry Association (SIA) International Roadmap for Semiconductors 2003 Edition, <http://public.itrs.net>
- [3] SIA girds for life after CMOS in EE Times (2004), p. 1.
- [4] R. Compano, *Technology Roadmap for Nanoelectronics* (2000).
- [5] S. Iijima, Nature **354**, 56 (1991).
- [6] S. Iijima, and T. Ichihashi, Nature **363**, 603 (1993).
- [7] R. Saito *et al.*, Phys. Rev. B **46**, 1804 (1992).
- [8] J. W. Mintmire, D. H. Robertson, and C. T. White, J. Phys. Chem. Solid. **54**, 1835 (1993).
- [9] D. S. Bethune *et al.*, Nature **363**, 605 (1993).
- [10] A. Thess *et al.*, Science **273**, 483 (1996).
- [11] J. Kong *et al.*, Nature **395**, 878 (1998).
- [12] J. Kong, A. M. Cassell, and H. J. Dai, Chem. Phys. Lett. **292**, 567 (1998).
- [13] M. S. Dresselhaus, G. Dresselhaus, and P. C. Eklund, *Science of fullerenes and carbon nanotubes* (Academic Press, San Diego, 1996).
- [14] R. Saito, G. Dresselhaus, and M. S. Dresselhaus, *Physical properties of carbon nanotubes* (Imperial College Press, London, 1998).
- [15] M. S. Dresselhaus, G. Dresselhaus, and P. Avouris, *Carbon nanotubes : synthesis, structure, properties, and applications* (Springer, New York, 2000).
- [16] A. Jorio *et al.*, Phys. Rev. Lett. **86**, 1118 (2001).
- [17] S. J. Tans, R. M. Verschueren, and C. Dekker, Nature **393**, 49 (1998).
- [18] C. Dekker, Phys. Today **52**, 22 (1999).
- [19] H. W. C. Postma *et al.*, Science **293**, 76 (2001).
- [20] P. L. McEuen, Phys. World **13**, 31 (2000).

- [21] P. L. McEuen, M. S. Fuhrer, and P. Hongkun, *Ieee Trans. Nanotechnol.* **1**, 78 (2002).
- [22] P. Kim, and C. M. Lieber, *Science* **286**, 2148 (1999).
- [23] T. Rueckes *et al.*, *Science* **289**, 94 (2000).
- [24] J. H. Hafner *et al.*, *J. Phys. Chem. B* **105**, 743 (2001).
- [25] J. Appenzeller *et al.*, *Ieee Trans. Nanotechnol.* **1**, 184 (2002).
- [26] A. Javey *et al.*, *Nat. Mater.* **1**, 241 (2002).
- [27] C. M. Lieber, *Mrs Bull.* **28**, 486 (2003).
- [28] M. Dresselhaus, G. Dresselhaus, and P. Avouris, *Carbon Nanotubes: Synthesis, Structure, Properties and Applications* (Springer, 2001).
- [29] P. L. McEuen, and J. Y. Park, *Mrs Bull.* **29**, 272 (2004).
- [30] S. J. Pearton, *GaN and Related Materials* (Gordon and Breach, New York, 1997).
- [31] T. Ozel *et al.*, *Nano Lett.* **5**, 905 (2005).
- [32] R. Seidel *et al.*, *Nano Lett.* **4**, 831 (2004).
- [33] K. Bradley, J. C. P. Gabriel, and G. Gruner, *Nano Lett.* **3**, 1353 (2003).
- [34] E. S. Snow *et al.*, *Appl. Phys. Lett.* **86**, 033105 (2005).
- [35] G. B. Blanchet *et al.*, *Appl. Phys. Lett.* **85**, 828 (2004).
- [36] L. Valentini *et al.*, *Appl. Phys. Lett.* **82**, 961 (2003).
- [37] J. Oakley *et al.*, *Nanotechnology* **16**, 2218 (2005).
- [38] J. P. Novak *et al.*, *Appl. Phys. Lett.* **83**, 4026 (2003).
- [39] E. S. Snow *et al.*, *Science* **307**, 1942 (2005).
- [40] K. Lee *et al.*, *Nano Lett.* **4**, 911 (2004).
- [41] A. D. Pasquier *et al.*, *Appl. Phys. Lett.* **87**, 203511 (2005).
- [42] C. M. Aguirre *et al.*, *Appl. Phys. Lett.* **88**, 183104 (2006).
- [43] M. W. Rowell *et al.*, *Appl. Phys. Lett.* **88**, 233506 (2006).

- [44] J. W. Mintmire, B. I. Dunlap, and C. T. White, *Phys. Rev. Lett.* **68**, 631 (1992).
- [45] T. Guo *et al.*, *Chem. Phys. Lett.* **243**, 49 (1995).
- [46] S. Nakamura, S. J. Pearton, and G. Fasol, *The Blue Laser Diode: The Complete Story* (Springer-Verlag, Berlin, 2000).
- [47] H. Morkoc, *Nitride Semiconductors and Devices* (Springer-Verlag, Berlin, 1999).
- [48] J. K. Sheu *et al.*, *Ieee Photonic Tech. L.* **15**, 18 (2003).
- [49] J. H. Jang *et al.*, *Inst. Phys. Conf. Ser.* **184**, 295 (2005).
- [50] C. B. Xiong *et al.*, *J. Lumin.* **122**, 185 (2007).
- [51] W. Q. Fang *et al.*, *J. Lumin.* **126**, 636 (2007).
- [52] S. C. Hsu, and C. Y. Liu, *Electrochem. Solid St.* **9**, G171 (2006).
- [53] P. Waltereit *et al.*, *Nature* **406**, 865 (2000).
- [54] S. Nakamura, and S. F. Chichibu, *Introduction to Nitride Semiconductor Blue Lasers and Light-Emitting Diodes* (Taylor and Francis, London, 2000).
- [55] F. A. Ponce, and D. P. Bour, *Nature* **386**, 351 (1997).
- [56] H. Morkoc, and S. N. Mohammad, *Science* **267**, 51 (1995).
- [57] E. J. Kang *et al.*, *Electrochem. Solid St.* **8**, G327 (2005).
- [58] Y. Taniyasu, M. Kasu, and T. Makimoto, *Nature* **441**, 325 (2006).
- [59] J. Han *et al.*, *Appl. Phys. Lett.* **73**, 1688 (1998).
- [60] H. Hirayama *et al.*, *Appl. Phys. Lett.* **80**, 37 (2002).
- [61] T. Wang *et al.*, *J. Cryst. Growth* **235**, 177 (2002).
- [62] S. Ito *et al.*, *Phys. Status. Solidi. A* **204**, 2073 (2007).
- [63] Y. Ohba, T. Gotoda, and K. Kaneko, *J. Cryst. Growth* **298**, 682 (2007).
- [64] J. T. Chu *et al.*, *Jpn. J. Appl. Phys. 1* **45**, 2556 (2006).
- [65] S. N. Lee *et al.*, *Appl. Phys. Lett.* **88**, 111101 (2006).

- [66] C. Skierbiszewski, Acta. Phys. Pol. A **108**, 635 (2005).
- [67] Y. Ohba, and S. Iida, Physica Status Solidi a-Applied Research **200**, 126 (2003).
- [68] T. Miyajima *et al.*, J. Phys-Condens. Mat. **13**, 7099 (2001).
- [69] S. Nakamura, Ieee J. Sel. Top. Quant. **3**, 435 (1997).
- [70] C. K. Wang *et al.*, Ieee T. Electron Dev. **53**, 38 (2006).
- [71] D. W. Kim *et al.*, Physica Status Solidi a-Applied Research **201**, 2686 (2004).
- [72] C. Pernot *et al.*, Jpn. J. Appl. Phys. 2 **39**, L387 (2000).
- [73] H. Jiang *et al.*, Jpn. J. Appl. Phys. 2 **41**, L34 (2002).
- [74] H. Jiang *et al.*, Jpn. J. Appl. Phys. 2 **40**, L505 (2001).
- [75] K. P. Korona *et al.*, Acta. Phys. Pol. A **110**, 211 (2006).
- [76] J. B. Limb *et al.*, Appl. Phys. Lett. **89**, 011112 (2006).
- [77] S. Nakamura, IEICE Transactions on Electronics **E83C**, 529 (2000).
- [78] S. J. Pearton *et al.*, Mat. Sci. Eng. B-Solid. **82**, 227 (2001).
- [79] A. P. Zhang *et al.*, Appl. Phys. Lett. **78**, 823 (2001).
- [80] J. W. Johnson *et al.*, Ieee T. Electron Dev. **49**, 32 (2002).
- [81] J. W. Johnson *et al.*, Solid. State. Electron. **46**, 911 (2002).
- [82] P. Kung *et al.*, J. Eur. Ceram. Soc. **17**, 1781 (1997).
- [83] S. Keller *et al.*, Mater. Sci. Forum **264-2**, 1157 (1998).
- [84] M. Losurdo, P. Capezzuto, and G. Bruno, Mrs Internet. J. N. S. R. **4** (1999).
- [85] D. W. Kum, and D. J. Byun, J. Electron. Mater. **26**, 1098 (1997).
- [86] K. T. Liu *et al.*, J. Cryst. Growth **263**, 400 (2004).
- [87] V. V. Mamutin *et al.*, J. Cryst. Growth **202**, 346 (1999).
- [88] M. A. Sanchez-Garcia *et al.*, J. Cryst. Growth **202**, 415 (1999).

- [89] R. F. Davis *et al.*, Solid. State. Electron. **41**, 129 (1997).
- [90] T. Weimann *et al.*, Microelectron. Eng. **57-8**, 903 (2001).
- [91] R. S. Q. Fareed *et al.*, Mater. Chem. Phys. **64**, 260 (2000).
- [92] H. Amano, and I. Akasaki, Opt. Mater. **19**, 219 (2002).
- [93] S. J. Pearton *et al.*, J. Appl. Phys. **86**, 1 (1999).
- [94] H. J. Choi *et al.*, Adv. Mater. **17**, 1351 (2005).
- [95] F. Qian *et al.*, Nano Lett. **4**, 1975 (2004).
- [96] S. Gradecak *et al.*, Appl. Phys. Lett. **87** (2005).
- [97] G. S. Cheng *et al.*, Appl. Phys. Lett. **83**, 1578 (2003).
- [98] Y. Huang *et al.*, Nano Lett. **2**, 101 (2002).
- [99] Z. H. Zhong *et al.*, Nano Lett. **3**, 343 (2003).
- [100] S. Han *et al.*, Chem. Phys. Lett. **389**, 176 (2004).
- [101] V. Dobrokhotov *et al.*, J. Appl. Phys. **99**, 104302 (2006).
- [102] X. F. Duan, and C. M. Lieber, J. Am. Chem. Soc. **122**, 188 (2000).
- [103] Y. Huang *et al.*, Science **291**, 630 (2001).
- [104] A. Javey *et al.*, Nano Lett. **7**, 773 (2007).
- [105] F. Qian *et al.*, Nano Lett. **5**, 2287 (2005).
- [106] Y. Li *et al.*, Nano Lett. **6**, 1468 (2006).
- [107] Y. Li *et al.*, Materials Today **9**, 18 (2006).
- [108] H. J. Choi *et al.*, J. Phys. Chem. B **107**, 8721 (2003).
- [109] J. C. Johnson *et al.*, Nat. Mater. **1**, 106 (2002).
- [110] T. Y. Kim *et al.*, J. Cryst. Growth **257**, 97 (2003).
- [111] T. Kuykendall *et al.*, Nano Lett. **3**, 1063 (2003).

- [112] S. K. Lee *et al.*, Phys. Status. Solidi. B **241**, 2775 (2004).
- [113] S. K. Lee *et al.*, Phil. Mag. **87**, 2105 (2007).
- [114] P. J. Pauzauskie *et al.*, J. Am. Chem. Soc. **127**, 17146 (2005).
- [115] P. J. Pauzauskie, and P. Yang, Materials Today **9**, 36 (2006).
- [116] E. A. Stach *et al.*, Nano Lett. **3**, 867 (2003).
- [117] Y. Y. Wu, and P. D. Yang, J. Am. Chem. Soc. **123**, 3165 (2001).
- [118] P. Deb *et al.*, Nano Lett. **5**, 1847 (2005).
- [119] L. Delzeit *et al.*, Chem. Phys. Lett. **348**, 368 (2001).
- [120] computer code SRIM ([www.srim.org](http://www.srim.org))
- [121] C. L. Cheung *et al.*, J. Phys. Chem. B **106**, 2429 (2002).
- [122] Y. Li *et al.*, J. Phys. Chem. B **105**, 11424 (2001).
- [123] Y. Li *et al.*, Chem. Mater. **13**, 1008 (2001).
- [124] Y. Choi *et al.*, Nanotechnology **17**, 4635 (2006).
- [125] Y. Choi *et al.*, in Materials Research Society (MRS) Fall Meeting (Boston, MA, 2006).
- [126] Y. Choi, and A. Ural, in Photonics West (San Jose, CA, 2007).
- [127] H. Kanzow, and A. Ding, Phys. Rev. B **60**, 11180 (1999).
- [128] A. Jorio *et al.*, New J. Phys. **5**, 139 (2003).
- [129] A. Jorio *et al.*, Philos. T. R. Soc. A **362**, 2311 (2004).
- [130] H. Kataura *et al.*, Synthetic Met. **103**, 2555 (1999).
- [131] J. D. Plummer, M. D. Deal, and P. B. Griffin, *Silicon VLSI Technology: Fundamentals, Practice, and Modeling* (Prentice Hall, Upper Saddle River, NJ, 2000).
- [132] S. B. Chikkannanavar *et al.*, Nano Lett. **5**, 151 (2005).
- [133] B. W. Smith, M. Monthieux, and D. E. Luzzi, Nature **396**, 323 (1998).
- [134] J. S. Oakley, in *Physics* (University of Florida, Gainesville (FL), 2005), p. 97.

- [135] J. C. Meyer *et al.*, Appl. Phys. Lett. **85**, 2911 (2004).
- [136] H. B. Peng *et al.*, Appl. Phys. Lett. **83**, 4238 (2003).
- [137] H. B. Peng, and J. A. Golovchenko, Appl. Phys. Lett. **84**, 5428 (2004).
- [138] T. Kim *et al.*, Appl. Phys. Lett. **87**, 173108 (2005).
- [139] Y. H. Choi, J. Sippel-Oakley, and A. Ural, Appl. Phys. Lett. **89**, 153130 (2006).
- [140] Y. Choi *et al.*, in Optics East (Boston, MA, 2005).
- [141] Y. Choi *et al.*, in Materials Research Society (MRS) Fall Meeting (Boston, MA, 2005).
- [142] C. Y. Wang *et al.*, J. Vac. Sci. Technol. B **24**, 613 (2006).
- [143] D. P. Yu *et al.*, Appl. Phys. Lett. **73**, 3076 (1998).
- [144] D. K. Sood, P. K. Sekhar, and S. Bhansali, Appl. Phys. Lett. **88**, 143110 (2006).
- [145] C. H. Liang *et al.*, J. Non-Cryst. Solids **277**, 63 (2000).
- [146] Z. W. Pan *et al.*, Nano Lett. **3**, 1279 (2003).
- [147] R. S. Wagner, and W. C. Ellis, Appl. Phys. Lett. **4**, 89 (1964).
- [148] P. K. Sekhar *et al.*, Nanotechnology **17**, 4606 (2006).
- [149] H. K. Park *et al.*, Physica. E **37**, 158 (2007).
- [150] J. H. Hsu *et al.*, Nanotechnology **17**, 170 (2006).
- [151] B. Zheng *et al.*, Adv. Mater. **14**, 122 (2002).
- [152] Z. W. Pan *et al.*, J. Am. Chem. Soc. **124**, 1817 (2002).
- [153] L. Dai *et al.*, Phys. Lett. A **335**, 304 (2005).
- [154] S. H. Sun *et al.*, Solid. State. Commun. **128**, 287 (2003).
- [155] P. Wu *et al.*, Nanotechnology **18**, 125601 (2007).
- [156] Lacey Carbon TEM grids were used. For more information, see [http://www.tedpella.com/supflm\\_html/suptfilm.htm](http://www.tedpella.com/supflm_html/suptfilm.htm)
- [157] Y. Cui *et al.*, Appl. Phys. Lett. **78**, 2214 (2001).

- [158] K. Shimakura, T. Suzuki, and Y. Yadoiwa, *Solid. State. Electron.* **18**, 991 (1975).
- [159] A. S. Grove, C. T. Sah, and O. Leistiko, *J. Appl. Phys.* **35**, 2695 (1964).
- [160] J. Q. Hu *et al.*, *J. Phys. Chem. B* **106**, 9536 (2002).
- [161] W. Q. Han *et al.*, *Appl. Phys. Lett.* **76**, 652 (2000).
- [162] G. S. Cheng *et al.*, *Appl. Phys. Lett.* **75**, 2455 (1999).
- [163] K. W. Chang, and J. J. Wu, *Adv. Mater.* **16**, 545 (2004).
- [164] R. Calarco *et al.*, *Nano Lett.* **7**, 2248 (2007).
- [165] M. He *et al.*, *Appl. Phys. Lett.* **77**, 3731 (2000).
- [166] Y. P. Song *et al.*, *Phys. Rev. B* **69**, 075304 (2004).
- [167] C. C. Chen *et al.*, *J. Am. Chem. Soc.* **123**, 2791 (2001).
- [168] J. Li *et al.*, *Nano Lett.* **6**, 148 (2006).
- [169] J.-R. Kim *et al.*, *Appl. Phys. Lett.* **80**, 3548 (2002).
- [170] S. Han *et al.*, *Materials Research Society* **18**, 245 (2003).
- [171] W.-Q. Han, and A. Zettl, *Appl. Phys. Lett.* **80**, 303 (2002).
- [172] Z. C. Wu *et al.*, *Science* **305**, 1273 (2004).
- [173] E. S. Snow *et al.*, *Appl. Phys. Lett.* **82**, 2145 (2003).
- [174] Y. X. Zhou, L. B. Hu, and G. Gruner, *Appl. Phys. Lett.* **88**, 123109 (2006).
- [175] E. Bekyarova *et al.*, *J. Am. Chem. Soc.* **127**, 5990 (2005).
- [176] J. W. Seo *et al.*, *Ieee Photonic Tech. L.* **4**, 888 (1992).
- [177] H. K. Kim *et al.*, *J. Vac. Sci. Technol. B* **21**, 1273 (2003).
- [178] S. X. Lu, and B. Panchapakesan, *Appl. Phys. Lett.* **88**, 253107 (2006).
- [179] A. K. Okyay, C. O. Chui, and K. C. Saraswat, *Appl. Phys. Lett.* **88**, 063506 (2006).
- [180] P. Kapur, and K. C. Saraswat, in *International Interconnect Technology Conference* (2002).

- [181] A. Behnam *et al.*, Appl. Phys. Lett. **89**, 093107 (2006).
- [182] A. Behnam *et al.*, J. Vac. Sci. Technol. B **25**, 348 (2007).
- [183] W. A. Wohlmuth, P. Fay, and I. Adesida, Ieee Photonic Tech. L. **8**, 1061 (1996).
- [184] A. Behnam, and A. Ural, Phys. Rev. B **75** (2007).
- [185] S. M. Sze, D. J. Coleman, and A. Loya, Solid. State. Electron. **14**, 1209 (1971).
- [186] A. Behnam *et al.*, J. Appl. Phys. **103** (2008).
- [187] A. Behnam *et al.*, Appl. Phys. Lett. **92** (2008).
- [188] M. Ito, and O. Wada, Ieee J. Quantum Elect. **22**, 1073 (1986).
- [189] M. Klingenstein *et al.*, Solid. State. Electron. **37**, 333 (1994).
- [190] J. Burm, and L. F. Eastman, Ieee Photonic Tech. L. **8**, 113 (1996).
- [191] M. Seto *et al.*, Appl. Phys. Lett. **75**, 1976 (1999).
- [192] MEDICI computer code version W-2004.09-0 from Synopsys Incorporation.

## BIOGRAPHICAL SKETCH

Yongho Choi was born in 1974, in Daegu, South Korea. He received his bachelor's degree in electronic engineering from Kumoh National Institute of Technology, South Korea, in 2000. He started his graduate program in electrical and computer engineering at the University of Florida in fall 2003. He began working for Professor Ant Ural, studying nanotechnology. His research interests include nano-device fabrication and characterization.